VELOCITY AND TEMPERATURE MEASUREMENTS IN A HIGH MACH NUMBER SHOCK-TURBULENCE INTERACTION

A Dissertation

by

BRIANNE TAYLOR MCMANAMEN

Submitted to the Office of Graduate and Professional Studies of
Texas A&M University
in partial fulfillment of the requirements for the degree of

DOCTOR OF PHILOSOPHY

Chair of Committee,	Rodney D. W. Bowersox
Committee Members,	Simon W. North
	Diego A. Donzis
	Edward B. White
Head of Department,	Rodney D. W. Bowersox

December 2019

Major Subject: Aerospace Engineering

ABSTRACT

Shock wave turbulence interactions are important problems with ubiquitous applications in high-speed flight and propulsion. The complex physical processes during the interaction are not fully understood, where contemporary high-fidelity numerical simulations have brought into question classical linear interaction analyses (LIA). The differences are most pronounced at high Mach number (>2). The objective of this study was to experimentally examine the role of a normal shock wave on the modification of velocity and temperature fluctuations to provide an empirical basis to help close the emerging knowledge gap between classical and contemporary theories. The experiments were performed in a pulsed wind tunnel facility at Mach 4.4. The freestream disturbances provided the test-bed for the study, where the Taylor Reynolds numbers (Re_λ) were varied over a range of 80 to 170. The pulsed operation enabled sufficiently large statistical samples. A Mach stem normal shock was generated through the interaction of two mirrored oblique shock waves. Molecular tagging velocimetry and two-line planar laser induced fluorescence thermometry were conducted upstream and downstream of the normal shock wave and the fluctuating intensities were compared. The measured axial velocity fluctuation amplification factor $\left(\left\langle {U_{DS}}'^2 \right\rangle / \left\langle {U_{FS}}'^2 \right\rangle\right)$ was nominally 1.1-1.2 over the Reynolds number range tested. The measured values were consistent with LIA. The temperature fluctuation amplification factor $\left[\left(\left\langle {T_{DS}}'^2 \right\rangle / \langle T_{DS} \rangle^2\right) / \left(\left\langle {T_{FS}}'^2 \right\rangle / \langle T_{FS} \rangle^2\right)\right]^{1/2}$ was found to vary between 3.0-4.5, where the lowest Reynolds number condition saw the highest freestream disturbances and largest amplification. The freestream fluctuations were primarily in the entropic mode, which is believed to lead to the significantly higher amplification of the entropic mode reported in these measurements.

DEDICATION

To my mother and father, who developed my curious nature and have provided continuous encouragement and opportunity.

And to my husband, who is my light in the darkness.

CONTRIBUTORS AND FUNDING SOURCES

Contributors

This work was supervised by a dissertation committee consisting of Dr. Rodney Bowersox (advisor), and Drs. Diego Donzis and Edward White, of the Department of Aerospace Engineering, and Dr. Simon North of the Department of Chemistry.

All work conducted for the dissertation was completed by the student independently.

Funding Sources

This work was supported in part by a fellowship from Texas A&M University, a grant from the Air Force Office of Scientific Research (Grant # FA9550-12-1-0443), and a grant from the Department of Defense Office of the Under Secretary of Defense (Vannevar Bush Faculty Fellowship Grant # N00014-18-1-3020).

Its contents are solely the responsibility of the authors and do not necessarily represent the official views of Texas A&M University, the Air Force Office of Scientific Research, or the Department of Defense Office of the Under Secretary of Defense.

NOMENCLATURE

Acronyms & Abbreviations

ACE	Actively Controlled Expansion Nozzle
CARS	Coherent Anti-Stokes Raman Spectroscopy
CCNY	City College of New York
DAQ	Data Acquisition System
DNS	Direct Numerical Simulation
DS	Downstream
LDV	Laser Doppler Velocimetry
LES	Large Eddy Simulation
LIA	Linear Interaction Analysis
LIF	Laser Induced Fluorescence
MTV	Molecular Tagging Velocimetry
N2	Nitrogen
NACA	National Advisory Committee for Aeronautics
NAL	National Aerothermochemistry and Hypersonics Laboratory
NO	Nitric Oxide
N-S	Navier-Stokes (equations)
PHACENATE	Pulsed Hypersonic Adjustable Contoured Expansion Nozzle for Aerothermochemical Testing Environments
PIV	Particle Imaging Velocimetry
PLIF	Planar Laser Induced Fluorescence
PMT	Photo-Multiplier Tube
PVC	Polyvinyl Chloride

RDT	Rapid Distortion Theory
SFM	Sum Frequency Mixing
SGS	Subgrid-Scale Model
SNR	Signal to Noise Ratio
STI	Shock Turbulence Interaction
TKE	Turbulent Kinetic Energy
US	Upstream
UV	Ultra-Violet
YAG	Yttrium Aluminum Garnet

Subscripts & Superscripts

0	Initial state/population, total condition
1	Upstream of normal/oblique shock, state 1
2	Downstream of normal/oblique shock, state 2
12	(or 21) Rate direction in two-energy level model
∞	Freestream condition
DI	Demarcation between dissipation and inertial ranges
DS	Downstream of normal shock
EI	Demarcation between inertial and energy containing ranges
FS	Freestream
i	Index notation
j	Index notation
rot	Rotational
SAT	Saturation
t	Total (stagnation)
vib	Vibrational

Parameters & Variables

a	Speed of sound
A_{21}	Rate constant for spontaneous emission
b_{12}	Rate constant for absorption
b_{21}	Rate constant for stimulated emission
c	Speed of light
C_{12}	Experimental calibration constant
c_p	Specific heat capacity
E	Energy
f_B	Boltzmann population fraction
G	Amplifcation factor
h	Specific enthalpy
$h\nu$	Energy of emitted photon
I_ν	Laser irradiance
J''	Rotational state
k	Boltzmann constant
K	Ratio of laminar shock thickness to Kolmogorov scale
l	Eddy size, length scale
L	Integral length scale
M	Mach number
M_s	Shock Mach number
M_t	Turbulent Mach number
N	Population density
N_1^0	Initial population
p	Pressure

P	Rate constant for predissociation
Q_{21}	Rate constant for collisional quenching
r	Auto-correlation function
r^2	Goodness of fit parameter
R	Gas constant
R_{12}	Ratio of LIF signal for states 1 & 2
Re/m	Unit Reynolds number (1/m)
Re_λ	Taylor based Reynolds number
s	Specific entropy
S	Mach stem height
S_f	LIF signal intensity (Boltzmann)
S_{LIF}	LIF signal intensity
t	Time
T	Temperature, averaging time scale, integral time scale
t_λ	Taylor time scale
U	Velocity (axial direction)
V	Volume
v''	Vibrational state
W_{2i}	Rate constant for photo-ionization
x	Direction vector
β	Shock angle
γ	Specific heat ratio
η	Kolmogorov scale
θ	Deflection angle
λ	Taylor micro-length scale

Λ	Integral length scale
ρ	Density
τ	Stress tensor, auto-correlation window
Φ	Generic dependent variable
Ω	Overlap function
$\frac{\Omega}{4\pi}$	Collection solid angle

TABLE OF CONTENTS

Page

LIST OF FIGURES

FIGURE Page

LIST OF TABLES

TABLE Page

1. INTRODUCTION

The work described in this dissertation are the results of a non-intrusive investigation of the interaction of freestream turbulence with a stationary normal shock wave. The motivation for this work is described below, followed by the scope of this study and an overview of the organization of the document.

1.1 Motivation

The interaction of turbulence with shock waves is of significant importance to the engineering community, particularly with respect to aerospace applications. Shock-turbulence interactions (STI) are prevalent in high speed aerodynamics. Specifically, STI is a leading contributor to the challenges in hypersonic vehicle design because of its ability to significantly alter the fluid dynamics downstream through amplification of turbulent modes and modification of energy transport. Even in typical wind tunnel testing, the interaction of freestream noise with inherent shock structures adds uncertainty and complexity to high speed diagnostics. Due to the non-linearity and coupling of modal interactions in the process, STI, even in its most basic form, is a complex problem.

Though it has been studied for several decades, the behavior of STI is still largely uncertain. Modern direct numerical simulation (DNS) studies ([1],[2]) have brought into question classical STI theories based on the linear interaction analyses (LIA) of Ribner ([3],[4]). These differences become increasing noticeable as the Mach number is increased beyond 2. At present, experimental data is not available to guide theory and reconcile these differences. This is especially true for non-intrusive measurements at high Mach number.

1.2 Problem Statement

1.2.1 Research Objective and Questions

The overarching objective of this study was to provide experimental insight into the role of a normal shock wave on the modification of turbulence by answering the following basic question:

'To what degree are vortical and entropic fluctuations amplified across a normal shock wave at high Mach number?' Answering this question will provide an empirical basis to help close the emerging knowledge gap between classical and contemporary theories.

1.2.2 Experimental Approach

An experimental campaign took place within the Texas A& M University National Aerothermochemistry and Hypersonics Laboratory. The experimental design was as follows:

- The target Mach number was selected to be sufficiently high to resolve the differences between classical ([3],[4]) and contemporary ([1],[5],[2]) theories, while not introducing undue experimental difficulty (e.g., the excessive heating to avoid liquefaction at hypersonic conditions). Hence, Mach 4.5 was targeted.
- Generating controlled turbulence at high Mach number represents a significant technical challenge. However, vortical (velocity), entropy (temperature), and acoustic (pressure) disturbances are commonly observed in high-speed wind tunnel freestreams. These small-scale freestream disturbances are typically assumed to be uncorrelated in a linearized approach [6]. Hence, a high Mach number wind tunnel freestream was selected as the test-bed.
- A Mach-stem generator was selected to produce a normal shock within the wind tunnel freestream. An innovative open-wedge design was developed to enable optical access. An image of the Mach stem at Mach 4.5 is shown in fig. 1.1 with a diagram outlining the interests of the study.
- The instruments were selected to be non-intrusive and responsive to the rapid jump in properties across a shock wave, which occur over a spatial range corresponding to about 3-5 molecular mean free paths. High energy, pulsed (10 Hz), laser-based systems to monitor the velocity and temperature of seeded nitric oxide were available. Hence, molecular tagging velocimetry (MTV) and 2-line planar laser induced fluorescence (PLIF) instrumentation was selected to quantify the vortical and entropic fluctuations. The expected uncertainties in the velocity and temperature were less than 0.5 %, which was sufficient to characterize the expected changes across the normal shock.

- The freestream gas was selected to be nitrogen to significantly improve the PLIF signal-to-noise ratio over that of air, where the presence of oxygen leads to significant quenching of nitric oxide fluorescence.
- A new pulsed wind tunnel was developed to achieve large data sets (>10,000 samples). The pulsed facility was synchronized to the laser systems with a duty cycle of nominally 20 seconds. However, the overall test duration was unbounded within the available infrastructure. The facility repeat-ability was within 3 % and 4 % for velocity and temperature, respectively, which was sufficient to quantify the expected changes across the normal shock.
- Finally, optical measurement of the acoustic (sound) fluctuations was not attempted in this study due to the unavailability of instrumentation. This is not considered a strong drawback as [7] has shown good agreement between LIA and DNS for the acoustic field.

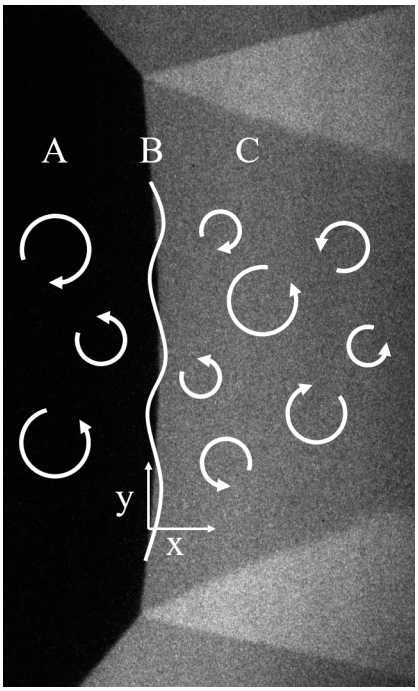

Figure 1.1: Schematic of canonical shock-turbulence interaction. A) freestream turbulent flow; B) example wrinkling of normal shock due to STI [2]; C) downstream amplified turbulent flow.

1.2.3 Contributions to the Field

The primary contribution of this study is a new experimental database quantifying the amplification of freestream fluctuations as they traverse a normal shock. The attributes of the database include:

- Sufficiently high Mach number to distinguish between competing theories.
- Non-intrusive optical techniques that rely on molecular tagging and emission, providing direct measurement of thermodynamic properties.

The secondary contributions include the development of an innovative apparatus that allowed for statistical convergence of experimental results, and further refinement of the data processing for reduced experimental uncertainty.

1.3 Organization of Document

The remainder of this document is broken into several sections that walk through the background, methodology, and results and conclusions of the study. The next section covers the fundamental elements of this work, highlighting the important physics, mathametics, and experimental methods. This is followed by a literature review of shock turbulence interaction which explores the previous theoretical, numerical, and experimental studies in canonical STI. Next, a section on facility development covers the design and operation of the PHACENATE facility and gives a description of the model design to fully establish the problem setup and inflow conditions. This is followed by a detailed description of the experiments performed and subsequent data processing techniques. Then a discussion of results is presented, exploring the findings of the study. Finally, the conclusions and recommendations section summarizes the work and presents the major findings and remarks on improvements and suggestions for future works.

2. FUNDAMENTALS

This section explores the basic flow elements and measurement techniques of this study. A general description of the individual aspects contributing to shock-turbulence interaction follows, with a brief overview of the conventional mathematics and procedures used in studying these features. Next is an exploration of available measurement techniques providing background for the methods chosen in this work. Some theory and mathematical description is provided.

2.1 Basic Flow Elements

The experimental domain of this work constitutes freestream turbulent flow interacting with a normal shock wave. The ideal case of turbulent flow is statistically invariant under translation, rotation, and reflection, classically defined as homogeneous and isotropic turbulence. Numerical techniques will often simplify this further to study a single fluctuating quantity. In practice, however, turbulence generated in wind tunnels can only be 'approximately' isotropic and will consist of acoustic, vortical, and entropic fluctuations. Here, the problem is broken into its constitutive elements to give a basic overview of the features in question: shock waves and turbulence. Conventional methods for studying these features is explored for the ideal case as well as some of the limitations and complexities that arise in real application.

2.1.1 Shock Waves

Shock waves are inherent to supersonic flow. While the overall phenomena is generally well defined, the processes within are still not fully characterized. This section covers the general definition and common treatment of shock waves in practice. The focus of this study is normal shock waves, a special case where the shock wave is formed perpendicular to the flow direction. To gain some physical insight into the creation of a normal shock, two cases are presented for a probe mounted in a wind tunnel subjected to a fluid flow (adapted from [8] and [9]).

Consider first, the flow is subsonic, gas molecules are traveling at less than the local speed of sound. As molecules of the gas collide with the probe this creates a disturbance in the flow, and

molecules are deflected around the probe. The disturbance is propagated through the flow by weak pressure waves, generally treated as sound waves, that travel at the local speed of sound of the gas. Because the gas is traveling at a subsonic speed, the pressure waves will propagate upstream. The flow will be 'aware' of the probe in every region and flow is deflected to compensate for the presence of the probe as shown in fig. 2.1a.

Consider the same probe, now subjected to supersonic flow. The gas is traveling at some speed greater than the local speed of sound and the pressure waves can no longer work their way upstream. The disturbances coalesce at some distance from the probe and form the phenomenon known as a shock wave. As shown in fig. 2.1b, the flow upstream of the shock is still unaware of the presence of the probe, while the flow downstream of the shock is necessarily disturbed to compensate for the presence of the probe. Thus, the shock wave is a thin region (typically a few molecular mean free paths) which acts as a boundary between the undisturbed and disturbed regions of flow and across which the flow properties change drastically.

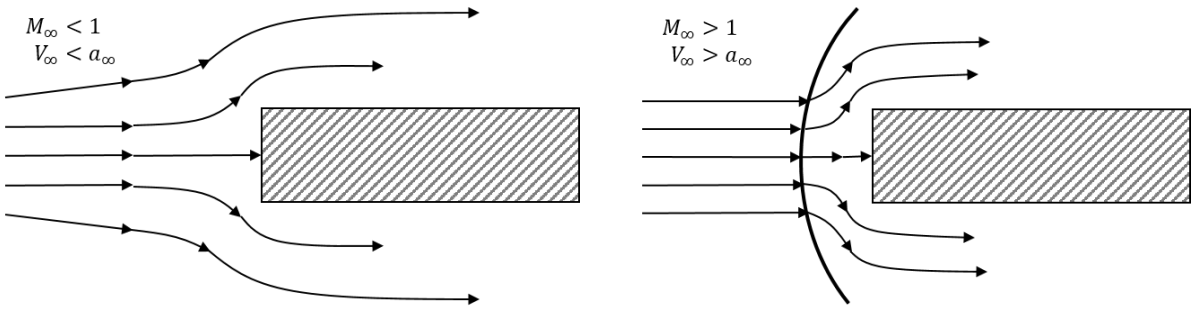

(a) Subsonic Flow (b) Supersonic Flow

Figure 2.1: Streamlines showing flow past a flat-faced object or probe in subsonic and supersonic conditions (adapted from Anderson [8]).

Although the shock wave does have a finite thickness, it is often treated as a discontinuity, where the flow properties instantaneously change from upstream to downstream conditions. This treatment is fairly robust in describing mean flow properties, however, it can become problematic in STI investigations where fluctuating quantities are of interest. It has even been shown that the

shock thickness can reach the same order of magnitude as turbulent length scales in some cases [10], thus, the shock can no longer be treated as a discontinuity. Many analytic and numerical models have been developed to describe the physics that are lost in the conventional shock-jump treatment, and these will be explored further in chapter 3, while the discontinuity approach will be continued here to establish the conventional method for normal shock treatment.

When analyzing a normal shock wave, it is advantageous to consider a control volume of constant area such as in fig. 2.2. The conditions in region 1 must be supersonic, and energy is neither added or removed so the flow is adiabatic. From this, the normal shock relations are simply the one-dimensional conservation equations of mass (2.1), momentum (2.2), and energy (2.3) for compressible flow. These are the general forms of the normal shock jump relations, and they must be solved numerically.

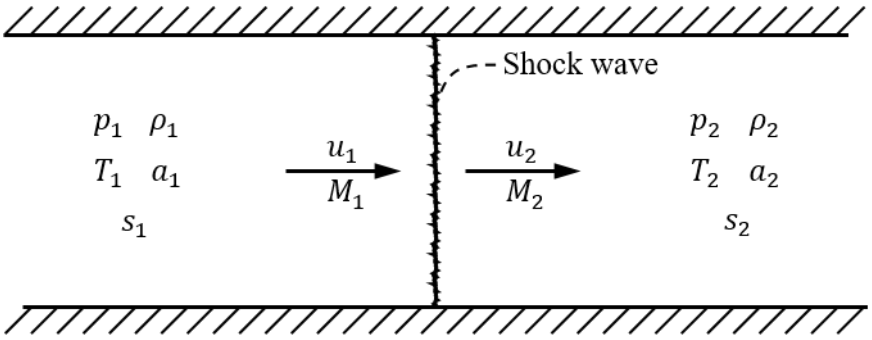

Figure 2.2: One dimensional normal shock schematic (adapted from NACA report 1135 [11]).

$$\rho_1 u_1 = \rho_2 u_2 \tag{2.1}$$

$$p_1 + \rho_1 u_1^2 = p_2 + \rho_2 u_2^2 \tag{2.2}$$

$$h_1 + \frac{u_1^2}{2} = h_2 + \frac{u_2^2}{2} \tag{2.3}$$

For a stationary normal shock wave, equation (2.3) implies that total enthalpy is constant across a shock. In the case of a calorically perfect gas, the enthalpy relation (2.4) adapts this to show that total temperature is constant across a shock. Additionally, by imposing the second law of thermodynmaics (holding that entropy must increase) it can be found that the total pressure of a calorically perfect gas must decrease across a shock wave. Another convenient result of the perfect gas assumption is that with the addition of the thermodynamic relations (2.4) and (2.5) derivation of algebraic solutions to the shock jump relations can be achieved.

$$h = c_p T \tag{2.4}$$

$$p = \rho R T \tag{2.5}$$

Algebraic shock jump relations are listed in the NACA 1135 report [11]. Some of the convenient forms are given below:

$$M_2^2 = \frac{(\gamma-1)M_1^2 + 2}{2\gamma M_1^2 - (\gamma-1)} \tag{2.6}$$

$$\frac{\rho_2}{\rho_1} = \frac{u_1}{u_2} = \frac{(\gamma+1)M_1^2}{(\gamma-1)M_1^2 + 2} \tag{2.7}$$

$$\frac{p_2}{p_1} = \frac{2\gamma M_1^2 - (\gamma-1)}{\gamma+1} \tag{2.8}$$

$$\frac{T_2}{T_1} = \frac{a_2^2}{a_1^2} = \frac{\left[2\gamma M_1^2 - (\gamma-1)\right]\left[(\gamma-1)M_1^2 + 2\right]}{(\gamma+1)^2 M_1^2} \tag{2.9}$$

$$\frac{p_{t2}}{p_{t1}} = \frac{\rho_{t2}}{\rho_{t1}} = \left[\frac{(\gamma+1)M_1^2}{(\gamma-1)M_1^2+2}\right]^{\gamma/(\gamma-1)} \left[\frac{\gamma+1}{2\gamma M_1^2 - (\gamma-1)}\right]^{1/(\gamma-1)} \tag{2.10}$$

Given that the upstream Mach number M_1 is defined to be greater than one, equation (2.6) easily shows that the downstream Mach number M_2 must be less than one. While this holds for

the calorically perfect case, this relation actually holds true in the non-perfect case as well from the application of the second law of thermodynamics to the general equations. Thus, M_1 is *always* supersonic, and M_2 is *always* subsonic in a normal shock relationship. It can be seen from the remaining equations that the static conditions of density, pressure, and temperature, must necessarily increase across a normal shock. As the Mach number in front of the shock increases above one, the 'strength' of the shock increases, and the relations across the shock become more dramatic. Continuing to increase M_1, the calorically perfect assumption begins to break down when the temperature downstream of the shock reaches the limit where γ is no longer constant. Thus, while the shock jump relations are found to be reasonably accurate for most cases in estimating mean values across a normal shock, numerical solutions of the general equations are often needed in real hypersonic environments.

2.1.2 Turbulence

Turbulent flow is prevalent in engineering applications of all kinds, appearing in both liquid and gaseous flows of various natures. Despite its common occurrence, there lacks a strict definition of turbulence, rather it is described through a set of characteristic features. Turbulent flow is described by Pope [12] as "unsteady, irregular, seemingly random and chaotic." It can be characterized as having a broad range of scales of motion with high sensitivity to boundary and initial conditions. Additionally, turbulent flows are known to have enhanced mixing rates of mass, momentum, and heat compared with laminar flows. Despite its "seemingly random" nature, turbulent flow is governed by the Navier-Stokes equations. While the equations fully describe the flow, the large number of length and time scales make directly solving such equations intractable. One answer to this is direct numerical simulation (DNS), which will be explored further in section 3.2 and is mainly limited to moderate Reynolds number flows. An alternative solution is the statistical approach, which involves statistically averaging the equations before solving them.

One averaging technique, first introduced by Reynolds [13], follows a time based averaging procedure. Given a dependent variable Φ, a Reynolds decomposition breaks the variable into its time-based mean and fluctuating components as seen in (2.11). The mean, $\bar{\Phi}$, is defined by (2.12),

where T is the averaging time scale.

$$\Phi = \underbrace{\overline{\Phi}}_{\text{mean}} + \underbrace{\Phi'}_{\text{fluctuation}} \tag{2.11}$$

$$\overline{\Phi} = \frac{1}{T}\int_0^T \Phi(t)dt \tag{2.12}$$

Following these definitions, it can be seen that applying a Reynolds average to a Reynolds-averaged value returns the same value, while the Reynolds average of the fluctuating part must be zero. Applying the Reynolds average to the continuity equation for compressible flow (2.13) results in the new form shown in (2.14).

$$\frac{\partial \rho}{\partial t} + \frac{\partial \rho u_i}{\partial x_i} = 0 \tag{2.13}$$

$$\frac{\partial \overline{\rho}}{\partial t} + \frac{\partial \overline{\rho u_i}}{\partial x_i} + \frac{\partial \overline{\rho' u_i'}}{\partial x_i} = 0 \tag{2.14}$$

It can be seen in this form, that for compressible flow, Reynolds averaging introduces a new term to the continuity equation. It follows, that additional terms appear in the momentum and energy conservation equations as well. This is the source of the closure problem of turbulence. The number of unknown quantities exceeds the number of equations, and additional relations are needed. A density weighted approach, introduced by Favre [14], helps to simplify this issue. Following Favre, the variable decomposition in (2.15) breaks the general dependent variable Φ into its density-weighted time-based mean and fluctuation components. The mean, $\widetilde{\Phi}$, in this case is defined by (2.16), where it is related to a typical Reynolds decomposition by the Reynolds-

averaged density.

$$\Phi = \underbrace{\widetilde{\Phi}}_{\text{mean}} + \underbrace{\Phi''}_{\text{fluctuation}} \tag{2.15}$$

$$\widetilde{\Phi} = \frac{\int_0^T \rho(t)\Phi(t)dt}{\int_0^T \rho(t)dt} = \frac{\overline{\rho\Phi}}{\overline{\rho}} \tag{2.16}$$

Again, looking at (2.13) and applying Favre averaging (with some simplifications from the relation to Reynolds averaging), the form of the Favre-averaged mass conservation equation for compressible flow is revealed as (2.17).

$$\frac{\partial\overline{\rho}}{\partial t} + \frac{\partial}{\partial x_i}(\overline{\rho}\widetilde{u_i}) = 0 \tag{2.17}$$

For compressible flow, the Favre averaged continuity equation matches the form of the laminar continuity equation where the Reynolds averaged form could not. Thus, though Reynolds is generally preferred for its simplicity in application, Favre averaging is advantageous in compressible flows. Additionally, when dealing with highly compressible or hypersonic flows where turbulent fluctuations can lead to significant density fluctuations, Reynolds averaging is generally not sufficient. Looking at the momentum (2.18) and energy (2.19) equations in Favre averaged form, the closure problem is again encountered with the introduction of several new terms including $\overline{\rho u_i'' u_j''}$ and $\overline{\rho u_i'' h}$. These are typically referred to as the Reynolds stress and turbulent heat flux. Turbulence modeling seeks to provide transport equations for these terms to effectively close the N-S equations. Experiments, such as in this study, are needed to provide basis for, and validate, these

models.

$$\frac{\partial}{\partial t}(\overline{\rho}\widetilde{u_i}) + \frac{\partial}{\partial x_j}(\overline{\rho}\widetilde{u_i}\widetilde{u_j}) = -\frac{\partial \overline{p}}{\partial x_i} + \frac{\partial}{\partial x_j}(\overline{\tau_{ij}} - \overline{\rho u_i'' u_j''}) \tag{2.18}$$

$$\begin{aligned}\frac{\partial}{\partial t}\left[\overline{\rho}\left(\widetilde{h} + \frac{\widetilde{u_i}\widetilde{u_i}}{2}\right) + \frac{\overline{\rho u_i'' u_i''}}{2} - \overline{p}\right] + \frac{\partial}{\partial x_j}\left[\overline{\rho}\widetilde{u_j}\left(\widetilde{h} + \frac{\widetilde{u_i}\widetilde{u_i}}{2}\right) + \widetilde{u_j}\frac{\overline{\rho u_i'' u_i''}}{2}\right] = \\ \frac{\partial}{\partial x_j}\left[\widetilde{u_i}\left(\overline{\tau_{ij}} - \overline{\rho u_i'' u_j''}\right) - \overline{q} - \overline{\rho u_j'' h''} + \overline{\tau_{ji} u_i''} - \overline{\rho u_j'' \frac{u_i'' u_i''}{2}}\right]\end{aligned} \tag{2.19}$$

As previously mentioned, turbulence is characterized by a range of scales of motion. Vortical structures, or eddies, form within the bulk flow that have somewhat coherent nature. Each of these structures has an associated length and velocity that describe its overall size and motion and can define its Reynolds number. The integral scale is the largest of these scales. It is related to the dimensions of the bulk flow and therefore has a Reynolds number similar to the mean Reynolds number of the flow. Most of the turbulent energy is found in this range, and viscosity effects are small. Richardson [15] introduces the "energy cascade". Larger scales become unstable and break up into smaller scales transferring their energy. The energy cascades to successively smaller scales until the smallest scale is reached, the Kolomogorov scale. At this scale, the eddy motion is stable and viscosity is effective in dissipating the turbulent kinetic energy.

The energy cascade below the largest scales is typically broken into two sub-ranges, the inertial subrange and the dissipation range. From Kolomogorov's similarity hypotheses, the inertial subrange is dominated by inertial effects, viscosity being negligible, while the dissipation range experiences significant viscous effects and is responsible for essentially all of the dissipation. The division of these sub-ranges across the length scales is shown in fig. 2.3, where the "universal equilibrium range" is defined by the two Kolomogorov hypotheses, and the "energy containing range" is the larger scales which contain the bulk of the turbulent energy (namely the integral scale). The suffixes DI and EI represent the demarcation between the disspation and inertial, and inertial and energy containing ranges respectively.

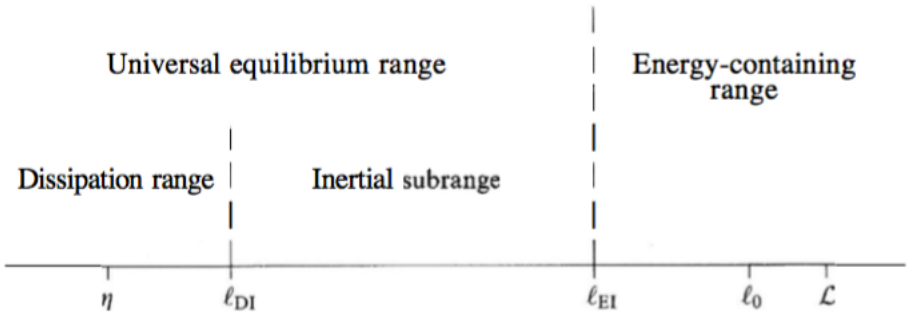

Figure 2.3: Eddy sizes, l, (on a logarithmic scale) at very high Reynolds number, showing the various lengthscales and ranges (reprinted from Pope [12]).

Another convenient scale to define is the Taylor microscale. This is an intermediate scale, loosely considered to be the largest of the dissipation range scales, or the dividing scale between the inertial and dissipation sub-ranges. While its physical interpretation is less intuitive, the Taylor microscale, λ, is easily defined by the rms of the fluctuating velocity field in (2.20).

$$\left(\frac{\partial u'}{\partial x}\right)^2 = \frac{(u')^2}{\lambda^2} \tag{2.20}$$

Due to this relation, the Taylor microscale is often used to characterize turbulent flow. In fact, the Taylor scale is directly related to the energy dissipation rate of the flow, and the Taylor Reynolds number is a convenient comparative quantity between turbulent flows, often referenced in DNS studies.

2.2 Measurement Techniques

This study was conducted with the use of molecular techniques, utilizing seeded nitric oxide as a tracer in a nitrogen flow. These techniques were chosen for their non-intrusive and instantaneous nature, ideal for a high speed turbulent flow. Some background and theory of various methods is described.

2.2.1 Physical Probing Methods

Conventional measurement techniques in wind tunnel testing employ the use of physical probes such as hot-wires and films, pitot probes, and thermocouples. These measurement devices can be very robust and offer good repeatability, but they suffer additional complications in high speed compressible flows that can make their use cumbersome. One limitation is the disturbance introduced as a result of the physical presence of the probe. In supersonic conditions, this generally means the formation of a shock wave in front of the probe which inherently changes the measured property. Much work has been done in the treatment of such measurements, such as Kovasznay's [16] breakdown of supersonic flow over a hot-wire. With limitation, the response of a physical probe can be within a reasonable uncertainty if carefully applied. In some cases, however, the presence of the probe has been found to fundamentally alter the flow behavior [17]. Thus, even following proper treatment of the preceding shock, the measurements will not represent the true process.

An additional limitation to these techniques is in the resolution of measurements. The physical probe can have adequate temporal resolution given appropriate response and data acquisition equipment, but can only offer point measurements in the spatial regime. In contrast, optical techniques can have high spatial and temporal resolution simultaneously. Some probes are mounted to traversing systems to allow measurement in several spatial locations, but this is no contender to the resolution provided in optical methods and is still limited by the physical size, mechanical resolution, and timing capabilities of the traversing system.

In the case of temperature measurements, physical probes are distinctly lacking in high speed flows. There is often a need to shield the thermocouple, adding to the complexity of their application and reducing their resolution. By nature, thermocouples do not directly measure the temperature of the fluid, rather the temperature of the thermocouple itself is measured and corrected based on assumptions for radiation, convection, and conduction.While there has been success with thermocouple probes in high speed environments, the advantage of optical methods can easily be seen for their ability to directly measure flow temperature with substantial resolution.

2.2.2 Optical: Particle-Tracking Methods

Particle tracking methods, such as particle imaging velocimetry (PIV) and laser Doppler velocimetry (LDV), are popular optical techniques for flow speed measurement. These methods utilize discrete particles that are seeded into the flow in the region of interest, either from local or upstream distribution methods. As the particles move with the flow, laser scatter signal is collected on a camera or detector. In the case of PIV, a planar laser sheet generates scatter signal in a two dimensional plane. Groups of particles are tracked between images to determine two component motion of the flow, including velocity and vorticity. In LDV, multiple lasers are focused and crossed at a point, generating an interference fringe pattern. Particles passing through this region scatter light, the frequency of which is related to velocity through the Doppler effect. Depending on the experimental setup, single or multi-component flow velocity can be determined. Both of these techniques have proven useful for velocity determination in a wide range of flow environments.

The limitation of these techniques is the use of discrete particles, namely, seeding capabilities and particle response. Much care must be taken to sufficiently distribute the particles in the area of interest without over-saturating the signal. Physical limitations of seeding in high speed gaseous flows can often over-encumber the ability. Additionally, these particles often cannot fully capture the fluid motion, particularly in low density environments. Tracking particles must be both neutrally buoyant, and of appropriate size for the technique to be applicable. When the particles are too small, they are unable to produce measurable scatter signal above noise limits. On the other hand, when particle size is increased, drag effects start to cause a phase shift or 'particle lag' [18]. In high speed turbulent environments, small scale turbulent motions can be lost due to particle lag. In the case of the shock problem, as in this work, particle methods have been shown to be insufficient in capturing the physical phenomena of interest [19].

2.2.3 Optical: Molecular-Tagging Methods

Molecular methods effectively address the shortcomings of PIV and LDV. Choosing an appropriate flow tagging molecule allows for essentially perfect flow tracking regardless of flow density.

Seeding concerns must still be addressed, and chemical compatibility can play a factor in application. Laser induced fluorescence (LIF) and its planar counterpart (PLIF) are useful for flow visualization, species concentration, and temperature measurements. These techniques are ideal for their non-intrusive nature. If care is taken in seeding and excitation, the flow is negligibly perturbed in the process, in contrast to conventional techniques that can create or modify significant flow structures. The methods chosen for this study were a combination of PLIF thermometry and molecular tagging velocimetry (MTV), using nitric oxide as a flow tracer. These techniques are advantageous for their relatively high sensitvity and simple experimental setup in comparison with other non-linear techniques such as coherent anti-stokes raman scattering (CARS) [20].

Detailed descriptions of the underlying physics, theory, and application of LIF techniques can be found in [21] and [17], among others. In essence, the LIF process begins with a laser excitation and ends with an emission process. The laser targets a specific rotational-vibrational transition and the molecule enters an excited state. The molecule relaxes to its ground state through spontaneous emission and the emitted photons, or fluorescence, can be captured by a detector. A simplistic two energy level model of this process is shown in fig. 2.4.

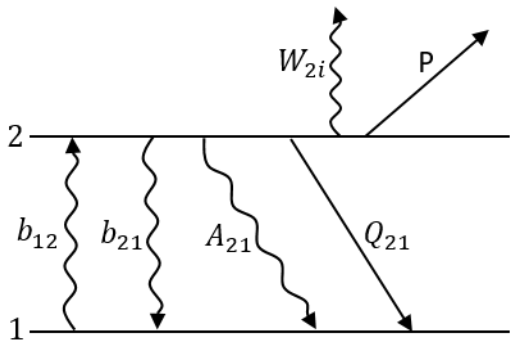

Figure 2.4: Simple two energy-level diagram for basic LIF process (adapted from Eckbreth [17]).

In this model, the various processes connecting the two energy levels are labeled by their respective rate constants which will be described briefly. The rate constants for absorption and

stimulated emission are shown as b_{12} and b_{21} respectively. A_{21} is the spontaneous emission rate constant given by the Einstein A coefficient and Q_{21} is the rate constant for collisional quenching. W_{2i} and P are rate constants for photo-ionization and predissociation, which will be considered negligible in this example. The absorption and stimulated emission rate constants can be related to their respective Einstein B coefficients by (2.21), where I_ν is the incident laser irradiance, Γ is the overlap function between the laser line shape and the absorption line, and c is the speed of light.

$$b = \frac{BI_\nu\Gamma}{c^2} \tag{2.21}$$

The population densities for the lower and upper energy levels can be written as rate equations taken from the rate constants in fig. 2.4, where W_{2i} and P have been neglected.

$$\frac{dN_1}{dt} = -b_{12}N_1 + (b_{21} + A_{21} + Q_{21})\,N_2 \tag{2.22}$$

$$\frac{dN_2}{dt} = b_{12}N_1 - (b_{21} + A_{21} + Q_{21})\,N_2 \tag{2.23}$$

It can be seen that adding the population density rate equations results in cancellation of the right-hand terms, thus, the total population of both states at any time is equal to the initial population, N_1^0, which is assumed to be entirely in the lower state (2.24).

$$\frac{d}{dt}\,(N_1 + N_2) = 0 \Rightarrow N_1 + N_2 = constant = N_1^0 \tag{2.24}$$

The total fluorescence signal is directly proportional to the population density of the excited state N_2, and the spontaneous emission rate constant A_{21}. Additional factors for the total LIF signal come from the experimental conditions. These are the energy of the emitted photon $h\nu$, collection volume of the detector V, and the collection solid angle $\frac{\Omega}{4\pi}$, as seen in the total LIF signal equation (2.25).

$$S_{LIF} = A_{21}N_2\frac{\Omega}{4\pi}h\nu cV \tag{2.25}$$

Using the population density relations above, the LIF signal equation can be written in the form of (2.27), where the saturation spectral irradiance, I_ν^{SAT}, is defined in (2.26) as the power needed for the rates of stimulated processes (stimulated absorption and emission) to equal the rates of spontaneous processes (spontaneous emission and collisional quenching).

$$I_\nu^{SAT} = \frac{c^2\left(A_{21} + Q_{21}\right)}{\Gamma\left(B_{21} + B_{12}\right)} \tag{2.26}$$

$$S_{LIF} = A_{21} N_1^0 \frac{B_{12}}{\left(B_{21} + B_{12}\right)} \frac{1}{\left(1 + I_\nu^{SAT}/I_\nu\right)} \frac{\Omega}{4\pi} h\nu c V \tag{2.27}$$

An important factor in the form of (2.27) is the ratio of saturation intensity to the actual laser intensity used in the experiment. There are generally two regimes of operation: the saturation regime where $I_\nu \gg I_\nu^{SAT}$, and the linear regime where $I_\nu \ll I_\nu^{SAT}$. In the case of this work (targetting NO with low power UV wavelengths), typical operation is in the linear regime and the LIF signal equation takes the form of (2.28), where the LIF signal is a linear function of laser intensity.

$$S_{LIF} = N_1^0 B_{12} \frac{A_{21}}{(A_{21} + Q_{21})c} \Gamma I_\nu \frac{\Omega}{4\pi} h\nu \tag{2.28}$$

In thermometry applications, the excitation laser wavelength is set to target a specific rotational state of the tracer molecule. The population density, N_1^0, can be modified by the Boltzmann population fraction, f_B, of the target state and the experimental volume, V, to determine the population density of the specific rotational-vibrational state. The LIF signal equation takes the form (2.29), where f_B is defined by the energy (E) and temperature (T) of the target state, as well as the Boltzmann constant (k) and the rotational level (J'').

$$S_{LIF} = f_B N_1^0 B_{12} \frac{A_{21}}{(A_{21} + Q_{21})c} \Gamma I_\nu \frac{\Omega}{4\pi} h\nu V \tag{2.29}$$

$$f_B = e^{E_{vib}/kT_{vib}} (2J'' + 1) e^{-E_{rot}/kT_{rot}} \tag{2.30}$$

A common application of PLIF thermometry is the two-line technique, where two excitation lasers are used to target individual rotational states of the tracer molecule. When the same vibrational state is targeted in excitation, the ratio of the signal intensity from each rotational state gives a direct indication of the rotational temperature of the flow. The vibrational temperature component from the Boltzmann population fraction conveniently cancels out of the equation in this case. As seen in (2.31) and (2.32), the intensity ratio can be simplified by gathering experimental influences into a constant "C_{12}" that can be determined through experimental calibration. The equation is often further reduced by including the rotational J sates and denoting C_{12} as ${C_{12}}'$.

$$R_{12} = \frac{S_{f1}}{S_{f2}} = C_{12}\frac{(2J_1'' + 1)}{(2J_2'' + 1)}e^{-\Delta E_{rot}/kT_{rot}} \tag{2.31}$$

$$R_{12} = {C_{12}}'e^{-\Delta E_{rot}/kT_{rot}} \tag{2.32}$$

In MTV applications, the motion of the LIF signal is studied, rather than the intensity. A discrete pattern of excited molecules is generated and then tracked with a LIF technique. The initial excitation laser is typically formed into a series of lines through use of a lens apparatus or screen, and "writes" a pattern of vibrationally excited molecules. In two component application, the "write" laser can be split in order to create a grid of crossing lines. The evolution of the excited molecules can be tracked through their lifetime with secondary "read" lasers, typically formed into sheets. The exact LIF intensity is no longer important, needing only to have a sufficient SNR to distinguish the excitation pattern from the background noise. Flow velocity is then simply deduced from the movement of the pattern and the time delay between captured fluorescence images.

3. LITERATURE REVIEW OF SHOCK-TURBULENCE INTERACTION

Shock-turbulence interactions are found in a wide range of applications and have been studied extensively in theoretical, computational, and experimental works. Basic understanding of the interactions has been improved through the years, but the fundamental physics have yet to be fully described. Extensive literature reviews covering the realm of STI can be found in [22], [7], and [23] among others; a brief synopsis is given here concerning the more relevant works to the current study.

3.1 Theoretical Work

Initial work in STI came from a theoretical linear analysis approach, attributed to Ribner ([3],[4],[24]) and Moore [25]. The first works investigated individual shear waves passing through a shock wave. These works were expanded to treat the incoming flow as a spectrum of sinusoidal shear waves of varying strength and orientation. In the linear treatment, later called linear interaction analysis (LIA), it was predicted that the shock wave would modify the incident shear wave and activate the acoustic mode downstream of the shock in the form of pressure waves. The acoustic noise generation in LIA was the first evidence of turbulence enhancement through a shock wave. In similar agreement, Kovasznay indicated that the incoming turbulence could be broken into three fluctuating modes (acoustic, entropic, and vortical), and analysis of a single incident mode would produce all three modes downstream of a shock wave interaction [6],[26]. The predictions of Ribner were qualitatively verified by Sekundov [27] and Dosanjh and Weeks [28], and continued theoretical and numerical works ([29], [30],[31],[32]) see similar agreement to LIA. Zang et al [33] found linear theory to be reliable to "extraordinarily large amplitudes" in the cases of weak shocks and strong disturbances.

In a more recent study, Mahesh et al [34] applied an extension of Moore's linear analysis to a field of acoustic waves interacting with a shock wave. Where most previous studies have applied LIA to purely solenoidal fields, the study of acoustic disturbances hoped to simulate a more

real environment. Real world and experimental configurations often include acoustic disturbances in addition to the typical solenoidal disturbances. The interaction for acoustic waves was found to be notably different from that of vortical waves. The authors use the analysis to describe a vortical-acoustic interaction with a shock wave and suggest that some of the discrepancy between experimental results and LIA may be due to the acoustic component often left out of LIA.

Lele took another approach to STI, determining the shock jump relations in a turbulent mean flow by applying homogeneous rapid distortion theory (RDT) as a correction to the exact jump relations [35]. The classical jump conditions have been shown to suffer the closure problem of turbulence, they hold for the instantaneous flow but are unable to appropriately describe the mean flow due to the influence of fluctuating turbulent modes. The application of homogeneous RDT in this study treated fluctuations as incompressible, and incoming turbulence as isotropic. Although turbulent shock jump relations are presented, the simplifications showed the approach to be unrealistic in practical application. Jacquin et al [36] performed a similar study on the application of homogeneous RDT to predicting amplification of turbulent kinetic energy in axial compression using a Helmholtz decomposition. The study shows that amplification of total kinetic energy is limited to two analytic solutions in the purely solenoid-acoustic regime and the 'pressure released' regime. The results were found to predict much higher amplification than comparable DNS and LIA studies, and again, homogeneous RDT was found to be insufficient for the STI problem.

More recently, Zank et al [37] considered the shock problem with a self-consistent model to account for the mutual interaction of the shock wave and incident turbulence. The model was based on the inviscid form of the Burgers' equation, the most basic model for hypersonic flow, and jump conditions were formed for a basic hypersonic state. It was determined that energy in the turbulent fluctuations upstream of the shock was not only being amplified at the shock but also converted to mean flow energy downstream. A characteristic 'shock thickness' was also introduced, and the possibility of a turbulent viscosity model to describe the shock structure was proposed.

Wouchuk et al [38] later constructed an exact analytic model for STI by decomposing an isotropic vorticity field into Fourier modes, where each mode was assumed to interact with the

shock independently. Closed form exact analytic expressions were obtained for the characteristic quantities of STI and were presented as functions of γ and shock Mach number (M_s) only. The simplifications at the limits of weak and strong shock waves were explored, and the possibility of exact scaling laws was presented.

The theoretical works have shown that LIA can be applied, with limitations, to a range of STI conditions. Of particular note is the role of acoustic disturbances in STI. The acoustic response predicted by Ribner and Moore was the first evidence of turbulence enhancement in STI. Figure 3.1 shows one of the first shadowgraph images that provided proof of these predictions, motivating further analytic works by Ribner and others [39]. Additionally, the affect of *incoming* acoustic disturbances has been shown to be of critical importance to understanding STI as a whole. The notably different response of the acoustic mode is an important consideration when comparing idealized theoretical and numerical works with real-world experimental works, where acoustic noise is almost always present.

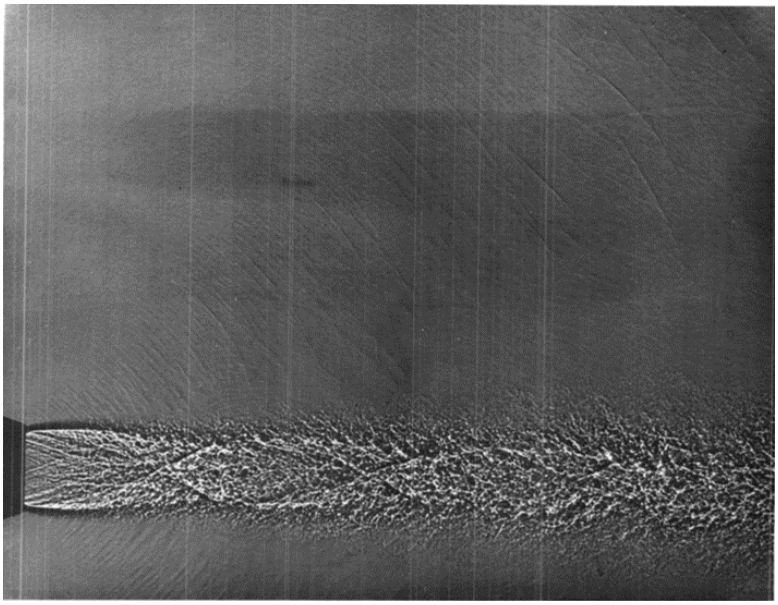

Figure 3.1: Shadowgraph of acoustic wave generation in a supersonic jet (reprinted from Ollerhead [40]).

3.2 Numerical and Computational Work

With the improvement of computing abilities, computational work has begun to play an integral role in the study of STI. Numerical works have relied on two methods for solving the shock problem, direct numerical simulation (DNS) and large eddy simulation (LES). DNS directly solves the Navier-Stokes equations for all of the turbulent scales, while LES only resolves the large scales of turbulent motion, approximating the dynamics of the smaller scales with a subgrid-scale (SGS) model. In comparison to DNS, LES can operate on a coarser mesh and thus reduce computational cost and increase the Reynolds number capability of simulation. This comes at the cost of approximating the smaller scales, inherently losing information of the complete turbulence behavior.

In an early work for the computational study of canonical STI, Rotman [30] solved Euler's equations for a traveling shock through a weak turbulent flow field. The problem treatment was "more a large eddy simulation without the SGS model than a direct numerical simulation". Good agreement was found with LIA predictions for the increase in turbulent kinetic energy (TKE) and decrease of turbulent length scales. This work was followed by a set of computations by Lee et al [31], [41] and Lee [42] in both DNS and LES for purely solenoid turbulent fields. In the first DNS study, the shock was fully resolved and the enhancement of TKE was observed across weak shock waves. The authors found partial agreement with linear analysis, observing that as the turbulent Mach number (M_t) increased, the shock would become distorted and discrepancy on TKE enhancement would arise. In the later DNS study, it was determined that comparable results could be found using a shock-capturing scheme, reducing the resolution cost of the study. In this case, the shock is computed, or numerically "captured", as part of the solution. This work also extended the Mach number range of the initial study and found that entropy fluctuations became more significant than acoustic fluctuations for Mach numbers greater than 1.65. The LES study by Lee explored the effectiveness of the SGS modeling for a comparable turbulent field to the DNS cases. Good agreement was found with filtered DNS, though the author determined that the shock-capturing scheme in LES produced excessive dissipation in the turbulence. It was suggested that shock capturing schemes in LES applications should be applied only in the direct vicinity of the

shock wave and in the direction normal to the shock plane.

Further LES works performed by Ducros et al [43], Dubois et al [44], and Garnier et al [45] explored purely solenoidal turbulent fields with Mach numbers in the range of 1.2 to 2 and turbulent Mach numbers ranging from 0.075 to 0.152. The first of these works developed a shock wave sensor which allowed local shock-capturing without the need for prior knowledge of the shock location. It was found that the sensor effectively limited dissipation away from the shock, but further treatment was needed to minimize the affects of dissipation within the shock. In the following works LES was compared with filtered DNS and found to have good agreement in the range of study. Ducros et al compared several SGS models and concluded that LES would only be sufficient for STI modeling when the mesh refinement around the shock could be small enough to capture the corrugation of the shock wave.

In a similar time frame Hannappel and Friedrich [32] performed a DNS study of a Mach 2 shock wave interacting with both in-compressible and compressible isotropic turbulence. For the compressible case, the authors note a new behavior of the shock turbulence interaction, having lower turbulence enhancement than expected. They suggested a relation between amplification ratios of turbulent quantities and the ratio of compressible to in-compressible kinetic energy to be used in turbulence modeling of the compressible regime. In a later work, Grube et al [46] conducted a DNS study of highly compressible isotropic turbulence ($M_t = 0.5 - 0.9$) for the Mach numbers in the range of 3.3 to 4.7. They found agreement with other, less compressible, studies for TKE enhancement and turbulent micro-length scale reductions through the shock wave. Further, they found that these effects would intensify with weaker turbulence upstream and stronger shock waves.

Mahesh et al [47] introduced the effect of entropy fluctuations on STI in a study using DNS and inviscid linear analysis on a weak turbulent field with vortical and entropic disturbances. The study focused on Mach numbers ranging from 1 to 3, with turbulent Mach and Reynolds numbers ranging 0.14-0.18 and 19.1-19.5 respectively. They found that the correlation between the upstream vorticy and entropy fluctuations had a large effect on the turbulence behavior across the shock. Specifically

they suggested that negative correlation between upstream velocity and temperature fluctuations would increase amplification of TKE as well as vortical and thermodynamic fluctuations across the shock wave; positive correlation having the opposing effect. Jamme et al [48] studied the effect of different types of isotropic turbulence interacting with a shock by combining vortical, acoustic, and entropic fluctuations. The conditions of the analysis ($M = 1.2, 1.5, M_t = 0.173, Re_\lambda = 5 = 6.7$) were similar to the earlier work of Mahesh et al, in this case using a shock resolving method. The authors explore the effects of purely solenoidal, solenoidal-entropic, and solenoidal-acoustic fields and find confirming results for the suggestions of earlier works by [47] and [32].

A comprehensive DNS study by Larsson and Lele [49] expanded previous works, (noting especially those of Lee et al [31], [41]), to a large range of mean and turbulent Mach numbers ($M = 1.3 - 6, M_t = 0.16 - 0.38$). The authors found that the Kolmogorov scale decreases in the shock interaction, and argued that grid refinement was necessary in both shock normal and transverse directions. This implied that previous studies may not have fully resolved viscous dissipation. Additionally, the authors investigated the changes in the shock-turbulence interaction for increasing strength of incoming turbulence relative to the local shock strength and identified two regimes for the interaction: wrinkled shock and broken shock. In the former, the relative weak turbulence experiences a clear shock-jump at every point and the shock retains a simple topology, while in the latter there exist smooth profiles through local regions where the shock is said to be broken or have 'holes'. Larsson would later confirm that the 'broken shock' regime is physical, and not a result of numerical treatment [2]. Bermejo-Moreno et al [50] followed the work of Larsson and Lele with an LES study targeting mean and turbulent Mach numbers of 1.5-3.5 and 0.16 respectively. The aim of the work was to evaluate different SGS models, focusing on the region just downstream of the shock wave in a canonical STI study. The authors explored several improvements to typical SGS models and found some agreement with the filtered DNS results as well as the error predictions of [51], suggesting future improvements to LES application in STI flows.

Wang and Zhong [52] further expanded DNS works up to Mach 30 using a new shock fitting routine. The authors observed that streamwise vorticity fluctuations would reach a peak at Mach

2.8 and then decrease as the shock strength continued to increase. Additionally, it was found that amplification of the streamwise Reynolds stress would initially decrease with increasing shock strength up to Mach 8.8 (consistent with LIA), but that the trend would then reverse for further increasing shock strength. The work included a perfect gas assumption. It was noted that the increasingly high temperature downstream of the strong shocks would be outside the limit of this assumption, and effects of thermochemical non-equilibrium should be considered in future work.

In several more recent works by Donzis ([10] & [1]) the role of the shock structure in STI was thoroughly investigated. A similarity parameter, K, was introduced as the ratio of laminar shock thickness to Kolmogorov length scale. Under this definition, the "wrinkled" and "broken" shock regimes could easily be categorized into small and large values of K. It was also suggested that the similarity parameter should be used to characterize amplification factors of turbulent quantities, and it was specifically shown to successfully collapse streamwise velocity amplification factors from several studies onto a universal scale. In fact, this analysis was expanded in a later work of Chen and Donzis [53] with continuing scaling agreement at high K. A mechanism for "shock holes" was proposed based on locally subsonic regions in the flow with general agreement to previous works, though it was suggested that expanded works would be needed to determine the precise mechanism. A following study by Donzis and Jagannathan [5] investigated the high Reynolds number limit for the relation of turbulence and shock gradients. It was found that small-scale intermittency in the turbulence could produce gradients on the same order as shock waves. This suggested that intermittency could, at least in part, be responsible for the formation of shock holes. The ratio of strongest turbulent gradient to shock gradient was introduced as a parameter to characterize this phenomenon.

A recent DNS study by Ryu and Livescu [54] focused on the linear limit of STI, investigating the effects of decreasing turbulent Mach number. The authors fully resolved the shock wave for Mach numbers ranging 1.1 to 2.2 and Taylor Reynolds numbers ranging from 10 to 45. It was found that, even at high Taylor Reynolds numbers, the DNS results converged to LIA solutions as the turbulent Mach number became sufficiently small. In this limit, Reynolds stresses and

vorticity components were found to be in agreement with LIA, where previous studies could only find agreement in TKE enhancement. The authors suggest that LIA is a reliable tool given a large separation of turbulent scales and shock width.

The most recent work by Braun et al [55] used LES to investigate STI for turbulent flows in the inertial range. The Taylor Reynolds number was expanded well beyond previous studies up to $Re_\lambda = 2500$ for mean and turbulent Mach numbers of 1.2-3 and 0.03-0.18 respectively. The results compared favorably with DNS in the applicable range of Re_λ, and it was noted that no significant Reynolds number effects were observed beyond $Re_\lambda = 100$. Also in agreement with DNS, the Reynolds stress amplification was found to have a weak dependence on Taylor Reynolds number in the range less than $Re_\lambda = 100$.

This work, along with the other numerical studies of canonical shock turbulence interaction, are listed in table 3.1. The respective simulation parameters, shock treatment, and upstream turbulent modes are tabulated for comparison. A significant trend, noted in [1] and [53], is the disparity between works at increasing Mach number. These works indicate that predictions of velocity amplification in STI through various techniques diverge beyond Mach 2, though it was suggested that the similarity parameter K brings works onto a universal scale. While general agreement is often reported in these works, and use of similarity scaling can provide some insight, it is clear that the high Mach number regime is an area of discrepancy which needs further investigation.

3.3 Experimental Work

Theoretical and Numerical works have come far in understanding the physics of STI, but as always, experimental results are necessary to fully validate the findings. Experimental work in canonical STI is sparse, as the requirements for flow field establishment and appropriate measurements are limiting. In practice, the shock wave can be treated experimentally in one of two ways: moving or stationary. The former case typically utilizes shock tubes and reflects the shock onto a grid-generated turbulent field. The latter case is usually performed in wind tunnel experiments where intentional geometries establish shock formation.

One of the earlier experimental works in STI was performed by Trolier and Duffy [56] in a

Author (Year) [REF]	Method	M_1	M_t	Re_λ	Shock Treatment	Upstream Turbulence
Bermejo-Moreno et al (2010) [50]	LES	1.5, 3.5	0.16	75	capture	
Braun et al (2019) [55]	LES	1.2-3.0	0.03-0.18	20-2500	capture	
Chen & Donzis (2019) [53]	DNS	1.1-1.4	0.05-0.54	10-65	resolve	sol
Dubois et al (2002) [44]	LES	1.29	0.127-0.152	17.29-33.2	capture	sol
Ducros et al (1999) [43]	LES	1.2	0.075		capture	sol
Garnier et al (2002) [45]	LES	1.2, 2	0.136, 0.108	11.9, 19	capture	sol
Grube et al (2011) [46]	DNS	3.31-4.66	0.52-0.86	22-26		sol
Hannappel & Friedrich (1995) [32]	DNS	2	0.1	5-6.7	capture	sol/ac
Jamme et al (2002) [48]	DNS	1.2, 1.5	0.173	5-6.7	resolve	sol/ent/ac
Larsson & Lele (2009) [49]	DNS	1.3-6	0.16-0.38	40	capture	
Larsson et al (2013) [2]	DNS	1.05-3.5	0.05-0.38	38-74	capture	
Lee (1993) [42]	LES	1.2-2	0.07-0.51	12-25	capture	
Lee et al (1993) [31]	DNS	1.05-1.2	0.0567-0.110	11.9-21.6	resolve	sol
Lee et al (1997) [41]	DNS	1.5-3	0.0897-0.110	15.7-19.7	capture	sol
Mahesh et al (1997) [47]	DNS	1.29, 1.8	0.14, 0.18	19.1-19.5	capture	sol/ent
Rotman (1991) [30]	DNS	1.1, 1.34			capture	sol
Ryu & Livescu (2014) [54]	DNS	1.1-2.2		10-45	resolve	
Wang & Zhong (2012) [52]	DNS	2-30	0.083-0.143	18.9-52.4	fit	sol

Table 3.1: Computational works in canonical STI

shock tube study. A pneumatically driven cutter was used to rupture the diaphraghm separating the high pressure driving gas and test gas in the driven section. The diaphragm opening process would lead to shock formation as well as establish initial turbulent conditions of the flow. Measurements were taken with a double-wire hotwire anemometer for a series of Reynolds numbers. Amplification of mass flux and total temperature fluctuations were reported to decrease with increasing

Reynolds number. Other early shock tube studies performed by Haas and Sturtevant [57] and Hesselink and Sturtevant [58] investigated the propogation of a weak shock wave through a discrete gaseous in-homogeneity and a statistically uniform medium respectively. Flow visualization techniques were employed in the form of spark shadography, schlieren photography, and shadowgraph photography. The main findings of the studies were that the Rayleigh-Taylor instability induced by the shock wave would enhance flow mixing, and that the turbulent scales appeared to decrease downstream of the shock passage.

Extensive studies have been performed in a shock tube facility developed at the City College of New York (CCNY) by Honkan and Andreopoulos ([59] & [60]), Honkan et al ([61]), Briassulis and Andreopoulos ([62]), Xanthos et al ([63]) and most recently Agui et al ([23]). The large scale facility passes shock-induced flow through a turbulence generating grid towards a removable porous end-wall. The strength of the reflected shock is controlled by the type of endwall in place at the time of operation and various hotwire and pressure ports are available in the test section for simultaneous measurement of multiple thermodynamic properties. Initial works investigated reflected moderate shock waves interacting with weak decaying turbulent fields. A combination of measurements were taken with hotwires and pressure transducers and the authors report significant amplification of turbulent intensities as well as length and time scales. It was noted that calculations of the initial turbulent field were not adequate due to the complexities associated with flow through the grid. The continued works in the shock tube facility studied the influence of grid size on the amplification of turbulent intensities and a new multi-hotwire probe was developed to observe vorticity evolution. In the most recent work, the authors reported direct measurement of the dissipation, and showed that dissipation increased through the shock interaction. It was additionally suggested that the dissipation would dominate flow motions more than enstrophy.

Another shock tube study by Keller and Merzkirch [64] applied speckle photography and hotwire measurements to analyze the interaction of a reflected shock and grid generated homogeneous, isotropic turbulence. Speckle photography is sensitive to density fluctuations, though the technique is limited to the assumption that the turbulent flow is homogeneous and isotropic. The

authors reported hotwire confirmation of these conditions. They found good agreement in density fluctuation amplification with the earlier work of Trolier and Duffy, and estimated the error in measurements to be on the order of 10 percent.

Initial work for canonical STI in a supersonic wind tunnel was performed by Jacquin et al [19] using laser Doppler velocimetry to study grid generated turbulence passing through a stationary shock wave. Experiments were performed in a continuous wind tunnel facility with a turbulence generating grid at the tunnel entrance. The grid acted as a sonic throat and Mach 1.65 flow was established downstream. A secondary throat controlled the formation of a stationary normal shock wave in the nozzle test section. The authors report an absence of amplification of TKE, but also noted that the use of LDV may not be appropriate. It has been shown that LDV over-estimates turbulent intensities in compressible flows, which could account for the inability to measure a notable amplification. In another work, Jacquin and Geffroy [65] studied STI in a heated jet. Amplification of turbulence intensity was reported within the jet region, though TKE was found to decrease in the mixing layer region. It was concluded that there were no significant effects from jet temperature on the amplification or TKE reduction.

Barre et al [66] studied the interaction of quasi-homogeneous isotropic turbulence with a stationary shock wave in a supersonic wind tunnel facility. The flow was initiated using a multi-nozzle design that established Mach 3 flow while simultaneously acting as a turbulence generating grid. The shock wave was established through the use of shock generator wedges, where the Mach reflection can be considered a purely normal shock wave. The flow field was probed using LDV and a hotwire anemometer. As noted before, the LDV technique is not ideal for this type of flow field, though the hotwire results for velocity fluctuation amplification were found to be in close agreement to LIA predicitons.

A more recent wind tunnel study by Mai [67] expanded the experimental database of canoncial STI to Mach 6 flow. Experiments were performed in a hypersonic blowdown wind tunnel facility, observing freestream total pressure fluctuation evolution through a stationary normal shock wave. The shock wave was established using shock generator wedges and total pressure fluctuations were

measured with a fast response Pitot pressure probe for several Reynolds number conditions. The author reported that amplification of pressure fluctuations, time scales, and power spectral densities were higher for the lower Reynolds number condition where lower freestream disturbances were measured. It was also noted that the amplification factors increased from a point downstream of the shock wave to a point farther downstream, indicating that the turbulent structures would take time to grow following the interaction.

3.4 Role of Current Study

The current work provides novel and non-intrusive velocity and temperature fluctuation measurements through a stationary normal shock wave. The target Mach number range was chosen due to the discrepancy between numerical and theoretical treatment that is seen as flow speed increases beyond Mach 2. Specifically, Mach 4.5 was targeted to limit tunnel pre-heating needs while maintaining definitive position within this range of discrepancy. Table 3.2 provides a list of experimental works in canonical STI with some of the relevant flow parameters and measurement techniques of each study. It can clearly be seen that there is a lack of non-intrusive investigation of STI, and the Mach number range is severely limited. This study is the highest Mach number investigation of velocity and temperature fluctuations in STI to date. Using non-intrusive methods on an isolated and stationary normal shock wave, this work will begin to fill this gap in knowledge of canonical STI behavior.

Author (Year) [REF]	Facility Type	M_1	M_t	Re_λ	Measurement Techniques (Intrusive)	Measurement Techniques (Non-Intrusive)	Measured Quantities
Agui et al (2005) [23]	Shock tube	1.04-1.392	0.01-0.05	260-1300	Hot-wire		$P, T_t, \rho U$
Barre et al (1996) [66]	Blowdown	3	0.011	15.5	Hot-wire	LDV	U
Briassulis & Andreopoulos (1996) [62]	Shock tube	1.551-2.183	0.02-0.06	162-735	Hot-wire		$P, T_t, \rho U$
Haas & Sturtevant (1987) [57]	Shock tube	1.007-1.1			PES	Spark Shadography	
Hesselink & Sturtevant (1988) [58]	Shock tube	1.007-1.1				Schlieren & Shadography	
Honkan & Andreopoulos (1990) [59]	Shock tube	1.62	0.050	$\sim$1000	Hot-wire		$P, T_t, \rho U$
Honkan & Andreopoulos (1992) [60]	Shock tube	1.62	0.033	$\sim$1000	Hot-wire		$P, T_t, \rho U$
Honkan et al (1994) [61]	Shock tube	1.24	0.040	$\sim$1000	Hot-wire		$P, T_t, \rho U$
Jacquin & Geffroy (1997) [65]	Continuous	1.6	0.07-0.123				
Jacquin et al (1993) [19]	Continuous	1.4	0.050	122.8		LDV	U
Keller & Merzkirch (1994) [64]	Shock tube	1.115-1.22				Speckle Photography	ρ
Mai (2014) [67]	Blowdown	6			Pitot		P_t
Trolier & Duffy (1985) [56]	Shock tube				Hot-wire		$P, T_t, \rho U$
Xanthos et al (2002) [63]	Shock tube	1.1-1.3		160-1300	Hot-wire	Raleigh Scattering	$P, T_t, \rho U$
Current Work	*Pulsed*	*4.4*	*0.052-0.083*	*80-170*		*MTV, PLIF*	*U, T*

Table 3.2: Experimental works in canonical STI

4. FACILITY DEVELOPMENT

4.1 The PHACENATE Facility

All experiments in this work were conducted in the pulsed hypersonic adjustable contour expansion nozzle for aero-thermochemical test environments (PHACENATE) facility located at the National Aerothermochemistry and Hypersonics Laboratory (NAL). The PHACENATE facility operates with a 60 ms total runtime with 10-15 ms of stable flow and a duty cycle of 10-20 s. The pulsed operation is ideal for laser diagnostic based experiments, and allows for large-sample data collection in order to analyze fluctuating quantities. This section will cover the major features and typical operation procedures of the facility.

4.1.1 Infrastructure and Design

PHACENATE is a tabletop-scale facility with a converging-diverging planar nozzle that free-jets into a rectangular test section. The nozzle was designed using a method of characteristics approach. The initial contour was taken from a previously designed large scale blow-down facility located at the NAL, the actively controlled expansion (ACE) wind tunnel [68]. The ACE facility supports a variable Mach number range of 4-7 by adjusting the nozzle throat height with a series of shims that can be installed or removed. The two nozzle planes are allowed to rotate to compensate for the throat adjustment while keeping a constant exit area. The PHACENATE facility replicates this ability in its nozzle design, details of which are shown in fig. 4.1. The initial nozzle contour from ACE was scaled down to a 10.2 cm x 10.2 cm (4 in x 4 in) exit area. This was then iteratively modified until uniform flow was predicted for the target Mach number range.

The nozzle exit opens to a rectangular test section with dimensions 25.4 cm H x 25.4 cm D x 58.4 cm L (10 in x 10 in x 23 in), shown in fig. 4.2. The test section has a series of mounting holes on the upper and lower walls of the cell. These are spaced 10.2 cm (4 in) apart in the transverse flow direction in the center of the cell, and spaced every 5.1 cm (2 in) in the axial flow direction. A series of rails was mounted to these holes, which were used to support a set of aerodynamic wedges. The

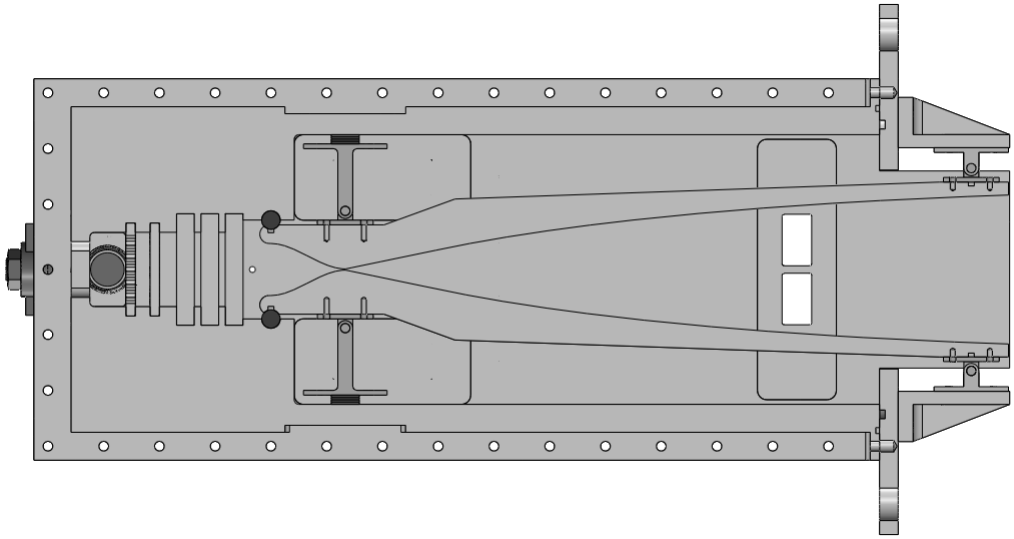

Figure 4.1: Schematic of PHACENATE nozzle.

test section provides optical access from all sides with 15.2 cm (6 in) diameter Schlieren quality windows in both sidewalls and 17.8 cm L x 2.5 cm W (7 in x 1 in) fused silica windows in the upper and lower walls. The Schlieren windows allow flow field imaging while the fused silica windows are needed for laser diagnostic measurement techniques. There are multiple window ports on the top and bottom walls of the tunnel allowing adjustment of diagnostic location. Several window blanks were outfitted as well, to allow additional pressure ports or sting assemblies to be used in the facility. Additional fused silica windows are located in the nozzle for future experiments in thermal non-equilibrium effects on turbulence generation but were not utilized in the experiments of this study.

Beyond the test cell, the flow is sent through a dump tank and then to a set of vacuum pumps through a 15.2 cm (6 in) diameter PVC pipe, pictured in fig. 4.3. To achieve hypersonic conditions, the vacuum pumps pull the test cell and nozzle down to 133 Pa (0.5 Torr) and the settling chamber is pressurized between 170-650 kPa (10-80 psig).

The facility is operated on a high pressure liquid nitrogen tank running through a regulator to the supply line. A set of mass flow controllers are located in-line to allow controlled mixing of nitric oxide into the supply. The gas mixture enters a pebble bed heater which acts to pre-heat the

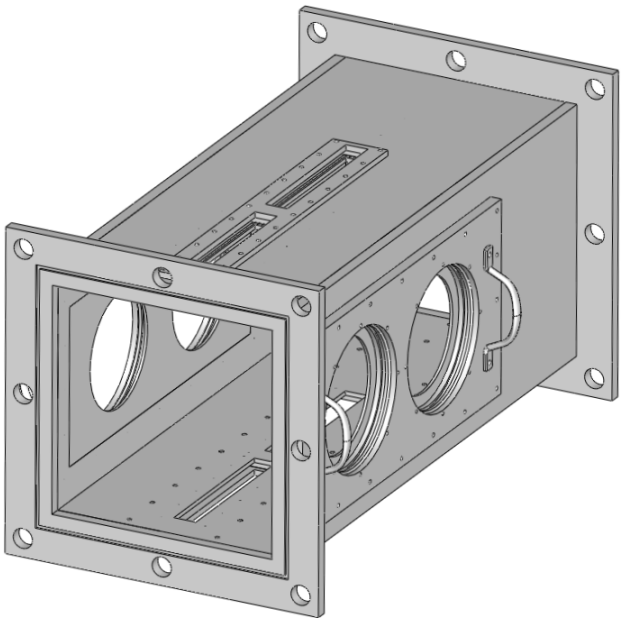

Figure 4.2: Schematic of PHACENATE test cell. Circular ports shown in the sidewalls and rectangular ports in the upper and lower walls. Mounting hole arrangement seen on the inside lower wall, and mirrored on the upper wall.

Figure 4.3: Picture of dump tank and vacuum pump infrastructure.

supply and force mixing for even composition. The temperature of the heater is set such that the expansion process of the gas entering the tunnel and flowing through the nozzle will not result in

liquefaction. The heated gas exits the pebble bed and fills a 0.1 m^3 (20 gal) reservoir which enters the settling chamber through a set of 2.5 cm (1 in) poppet valves, pictured in fig. 4.4. The poppet valves operate with energize times of 12 ms and are actuated by a series of MHJ Festo valves.

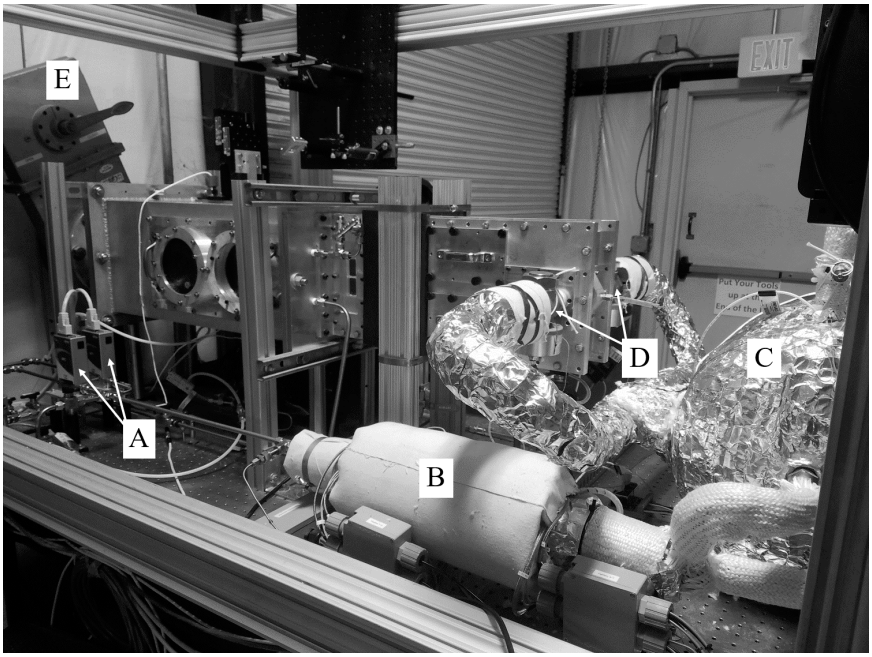

Figure 4.4: Image of the PHACENATE facility. Included labels are the mass flow controllers (A), pebble bed heater (B), inlet tank (C), poppet valves (D), and knife gate (E) leading to the dump tank and vacuum pumps through the wall.

Inside the settling chamber the nitrogen and NO mixture is sent through a set of aerogrids to force pressure equalization in the transverse directions. This is followed by a series of three meshes of decreasing coarseness to reduce flow disturbances before the gas mixture enters the nozzle contraction. A detailed image of this is shown in fig. 4.5. Ports are located on both sides of the settling chamber for installation of static pressure probes. An additional port at the back of the settling chamber allows access for a thermocouple probe.

A Quantum Composer 9520 series pulse delay generator is used to control tunnel operation. The Festo valves are triggered to open and close the poppet valves and then the lasers, cameras, and data acquisition are triggered at optimal time delays. The pulse delay generator has picosecond

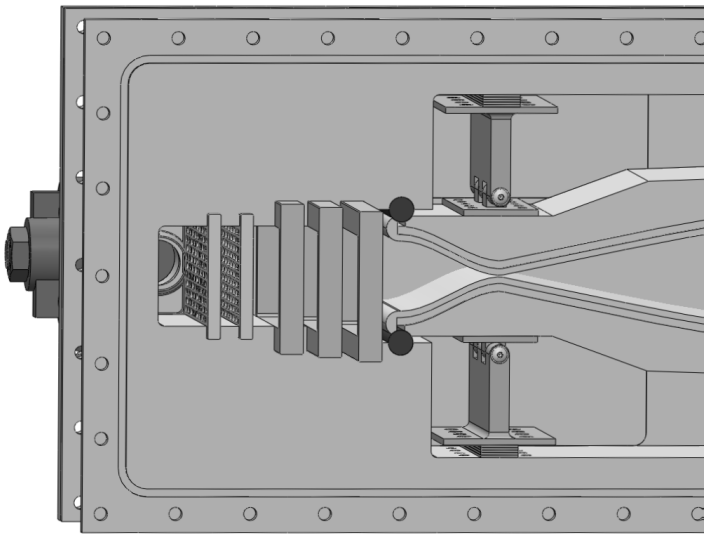

Figure 4.5: Close-up exploded view schematic of the settling chamber. Flow enters through poppet valves on both sides and then travels through two aero-grids followed by three mesh screens of successively decreasing coarseness.

resolution on 8 channels with <50ps jitter, and thus, is capable of controlling both tunnel operation and laser timing simultaneously.

4.1.2 Typical Operation

Typical operation of the PHACENATE facility follows a routine checklist. The tunnel operator must first allow sufficient time to warm up the vacuum pumps and pebble bed heater, as well as any experimental equipment needed during the run. The test section is opened to check or modify the experimental setup. Figure 4.6 shows a picture of the facility in a typical experimental configuration.

Once equipment is in place, the test section is cleared and closed up. The sidewalls are tightened and all valves are checked to be in the closed position, including vacuum lines to other facilities. To begin pulling vacuum on the test cell and nozzle, a small diameter tubing line is opened between the test cell and dump tank. When vacuum has been reached, the knife gate for the facility can be opened. Simultaneously, the supply tank can be pressurized with a heated N2-NO mixture, the composition of which is set through the mass flow controllers. Once the target pressure is

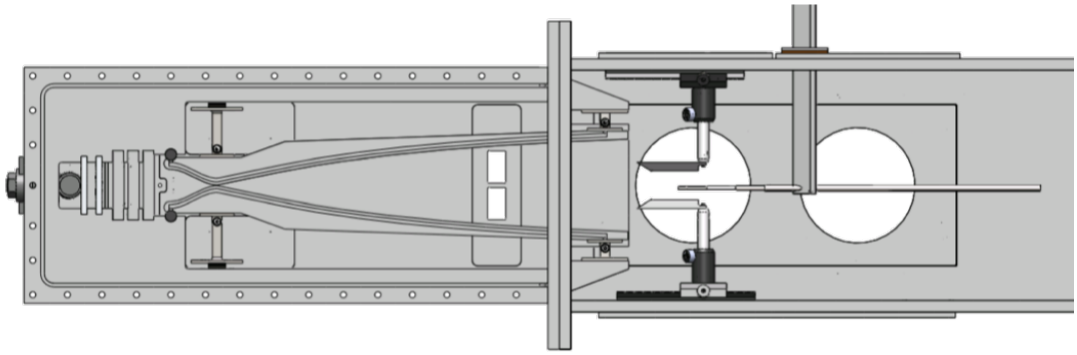

Figure 4.6: Schematic of the PHACENATE facility in a typical experimental configuration.

reached, ball valves leading to the poppet valves can be opened and operation can proceed.

To run the facility, a custom program, written in LabView, is used in conjunction with the pulse delay generator. The Labview program waits for a trigger from the pulse delay generator and begins data aquisition on the connected pressure and temperature probes. To start the tunnel, the operator runs the LabView program and runs through the checklist until the program states "Ready to Run". The operator can make sure all equipment is ready, and trigger any external data aquisition systems. Once satisfied, the operator presses 'run/stop' on the pulse delay generator and the tunnel will operate in pulsed mode until the 'run/stop' button in pressed again. A screenshot of the LabView program during a typical tunnel operation is shown in fig. 4.7.

Shutdown procedure follows the reverse of this process, the delay generator and data acquisition is stopped. The knife gate is closed, and then the test section is vented to reach atmospheric pressure. The supply tanks are closed and remaining pressurized supply is vented through a bypass valve. Heaters and vacuum pumps can be turned off, as well as any additional experimental equipment. In an emergency, a similar procedure is followed depending on the specific circumstances. The pulse delay generator is stopped, and tunnel supply valves can be closed. Lasers can be shut down with an emergency stop button and the operator can vent the supply through the bypass and evacuate the area if needed.

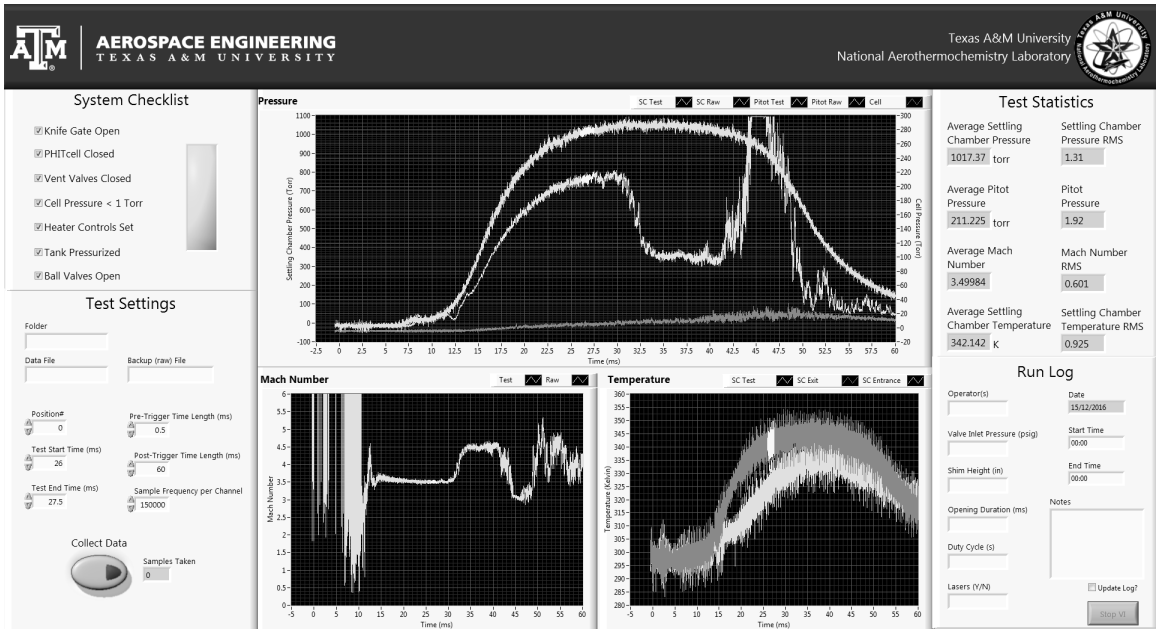

Figure 4.7: Screenshot of a typical run in the PHACENATE facility.

4.2 Model Development

A major part of this work was developing the 'canonical STI' flowfield to be investigated, namely, forming a freestanding normal shock wave in an optically accessible location. This was achieved by creating a Mach stem at the nozzle exit, through a set of aerodynamic wedges. This section will cover some of the basic theory of Mach stem formation and growth, as well as the design process that led to the experimental wedges used in this work.

4.2.1 Mach Stem Theory

Mach stem formation is simply the result of an irregular reflection of an oblique shock wave. In the most basic example, one can observe an oblique shock wave impinging on a surface, such as a wall. Figure 4.8 shows a diagram of a typical regular reflection. Incoming flow in region 1 is turned by the oblique shock so that the flow in region two downstream is parallel with the deflected wall surface, starting at point 'A'. At the upper wall surface, the flow must be turned again to accommodate the presence of the wall. The incident shock reflects at point 'B' at an angle defined by the original deflection angle, 'θ', and the Mach number in region 2.

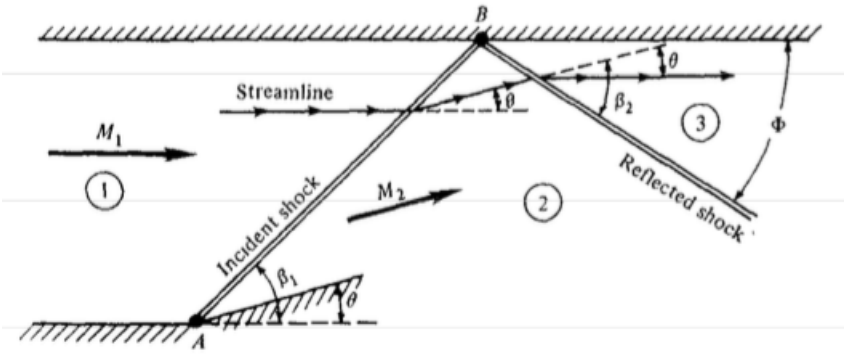

Figure 4.8: Regular reflection of an oblique shock wave incident on a wall (reprinted from Anderson [8]).

At sufficiently high Mach number, the reflected shock is not enough to compensate for the mass flow through the region, and an irregular reflection occurs. A normal shock, or Mach stem, extends from the wall to the incident shock at some distance away from the wall. This process is depicted in fig. 4.9. The oblique shock reflects at the intersection point with the Mach stem, which is commonly referred to as the triple point.

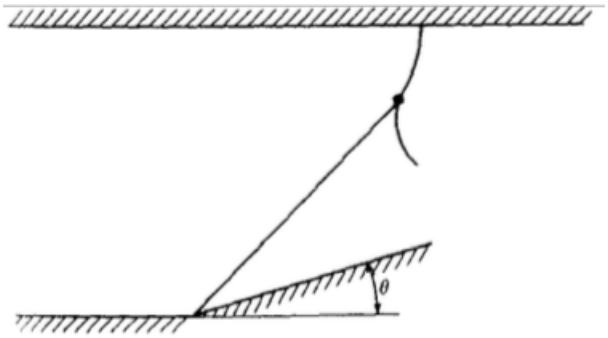

Figure 4.9: Irregular, or Mach, reflection of oblique shock incident on a wall (reprinted from Anderson [8]).

In the case of this work, it is advantageous to avoid wall or boundary layer effects in the region of the normal shock wave. To achieve this, the reflecting wall is replaced with a plane of symmetry. Two deflection surfaces mirror each other, and the interaction of the resultant oblique

shocks causes the formation of a Mach stem in the center of the flow. A schematic of this process is seen in fig. 4.10. In this figure, region 1 is the incoming supersonic flow. The flow in region 2, downstream of the incident shock, is parallel with the deflection surface. The flow is turned again by the reflecting shock as it enters region 3, still at a supersonic condition. Region 4 is downstream of the Mach stem, with initial conditions from region 1. From normal shock relations, the angle is unchanged but the flow becomes subsonic. The different conditions in regions 3 and 4 result in a shear layer between the regions that acts as a nozzle. The flow in region 4 accelerates and actually returns to a supersonic condition at the sonic throat, labeled at some distance downstream of the Mach stem.

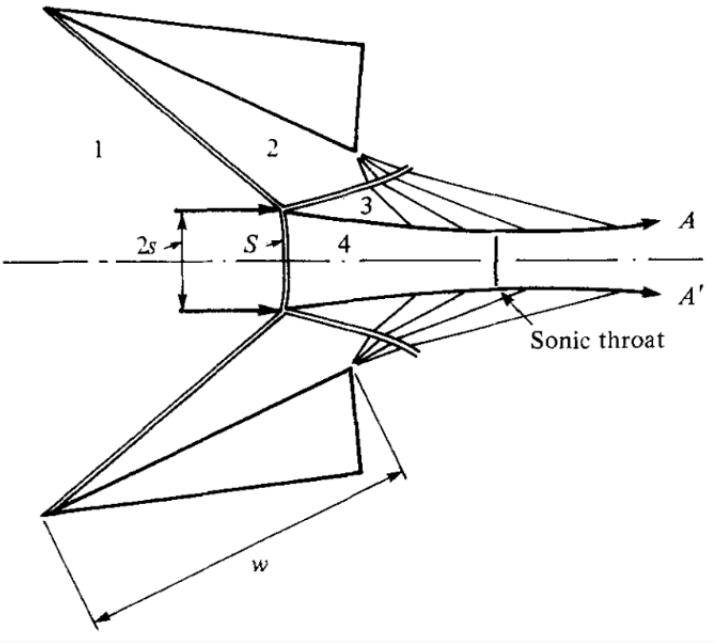

Figure 4.10: Mach stem flow from mirrored oblique shocks (reprinted from Hornung and Robinson [69]).

Predictions of the Mach stem height, 'S', and growth rate are detailed in [70]. The flow geometry is a function of incoming Mach number, specific heat ratio, and deflection surface geometry. From the work of Mouton and Hornung, only the angle and length of the leading edge of the de-

flection model is needed to satisfy the geometry unknowns. In an experimental work by Chpoun and Leclerc [71], is is shown that Mach stem formation and height is consistent between different model geometries, so long as the leading edge angle and length are kept constant. From this, Mach stem generator models can be developed for specific incoming flow conditions. The design process of the wedges used in this work is detailed in the next section.

4.2.2 Wedge Design and Implementation

The initial model design in this work was chosen by optimizing the leading edge angle and overall wedge height (easily related to leading edge length) using a Matlab procedure developed by [67] following the routine of [70]. For an expected Mach number range of 4 to 6, the ideal leading edge angle was found to be 32 degrees. This was determined by looking at the critical deflection angles for both the incident and reflected shocks. From fig. 4.11, the wedge deflection angle must lie below the top curve in order for the leading edge shock to remain attached, and above the bottom curve for a Mach reflection to occur. The 'design space' of Mach 4 to 6 is shown with diamond symbols for the selected 32 degree deflection angle, lying well within the two curves for the entire range. An overall height of 0.953 cm (0.375 in) was chosen to optimize the Mach stem height within the bounds of tunnel blockage allowance and the expected core flow diameter of 5.1 cm (2 in).

An additional consideration for the wedge design was optical access to the near region of the Mach stem from multiple directions. Camera access from the side of the tunnel was needed for imaging, as well as access for multiple laser sheets from the top or bottom of the tunnel. The initial wedge design incorporated flush mounted windows in the wedge body to accommodate laser access. A schematic of the original wedge design is shown in fig. 4.12, the wedge model shown is mounted to its supporting rail system and would be mirrored in the tunnel to create the Mach stem flow. The window is mounted just downstream of the leading edge, where the model transitions to a flat profile. While this did provide the necessary optical access, the fitting and mounting of the window was challenging, and the resulting flow was found to be unstable. The presence of the boundary layer on the wedge surface is thought to have lead to a pressure influence that caused the

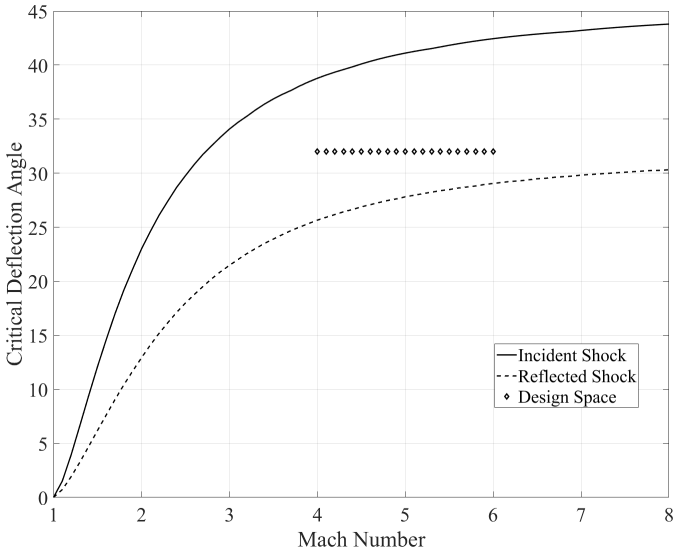

Figure 4.11: Critical deflection angles for Mach stem formation. Model deflection angles must fall between the two curves to generate a Mach stem, the design space of Mach 4 to 6 for the PHACENATE facility is shown with diamond markers.

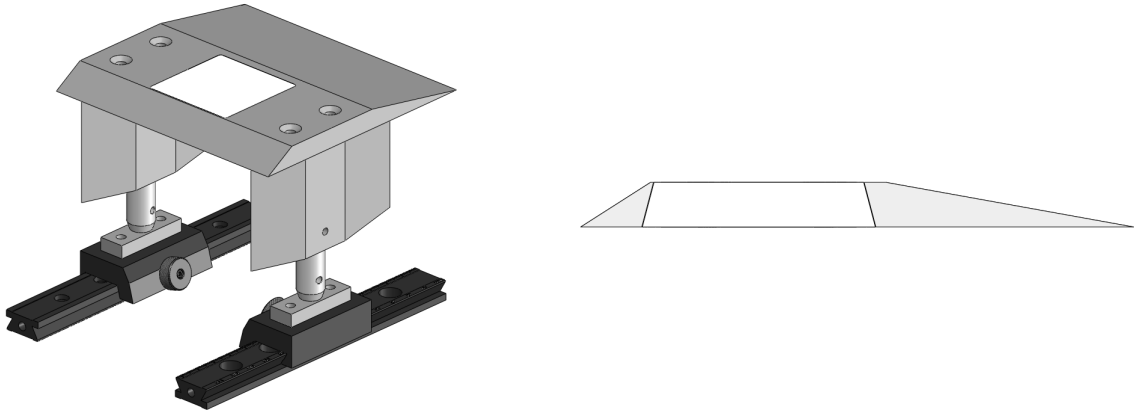

Figure 4.12: Schematic and cut-out view of initial wedge design.

Mach stem to begin growing nearly immediately in the test runs. A Schlieren image of the Mach stem flow for the initial wedge design is shown in fig. 4.13. The red outline is the expected flow structure predicted in the Matlab design code, scaled and overlayed on the image. Good agreement was seen in the initial flow structure, however growth occured rapidly, and the Mach stem quickly moved forward of the optical access point.

To accommodate this issue, a new wedge design was implemented that removed most of the

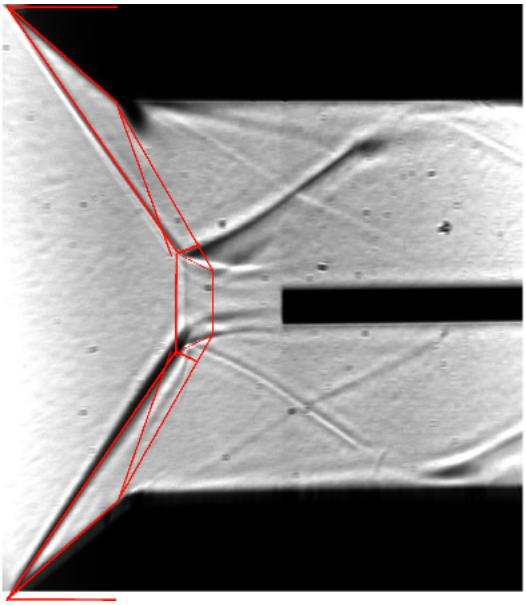

Figure 4.13: Schlieren image of Mach stem flow from initial wedge design. Red lines indicate expected shock geometry from Matlab code.

body of the wedge. While the initial wedge model followed a typical hypersonic body design, it was previously shown in [71] that this is not needed for Mach stem development. It was believed that the absence of a model structure downstream of the triple point may help to stabilize the flow by removing the shock-boundary layer interaction of the reflected shock. An additional advantage of this design was the elimination of the need for windows, as the region of the Mach stem became fully optically accessible. The wedge also implemented a swept back design to delay the influence of the shear layer of the nozzle sidewalls in hopes of minimizing blockage and stabilizing the flow. Figure 4.14 shows a schematic of the new model. The same leading edge angle and overall height of 32 degrees and 0.375in were used for the new triangular cross-section model.

A Schlieren image of the second wedge design, fig. 4.15, shows the clear improvement to the flow structure. The back pressure of the cell became the only influence driving the Mach stem growth, and the flow was stabilized for a period significantly longer than the time-length of the measurement techniques used in this study.

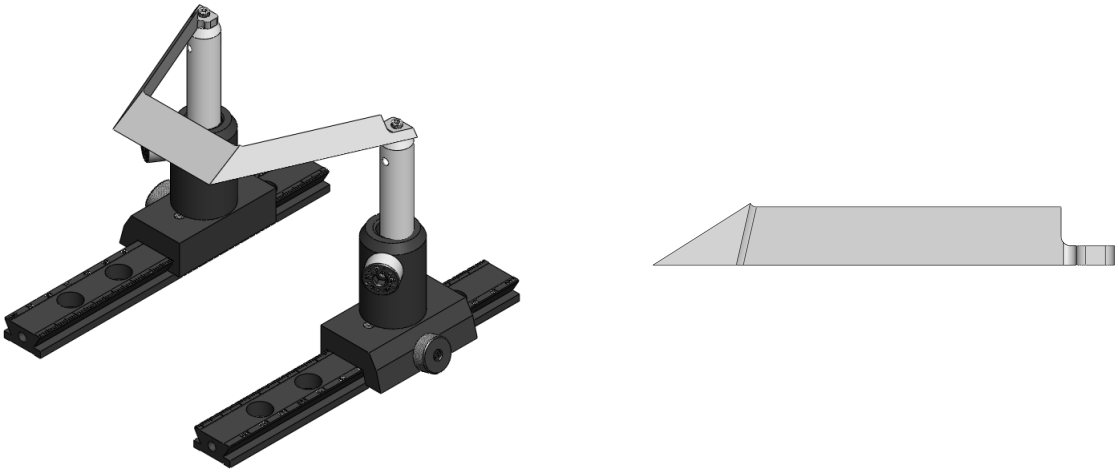

Figure 4.14: Schematic and cut-out view of final wedge design.

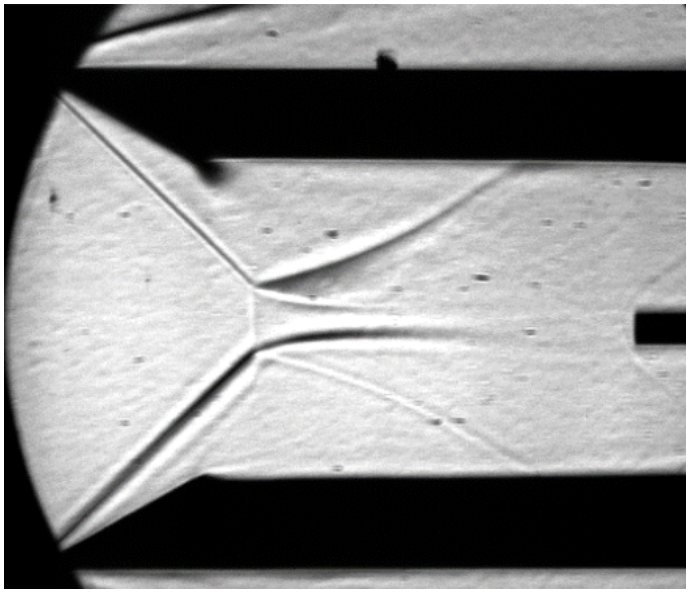

Figure 4.15: Schlieren image of Mach stem flow from final wedge design.

5. EXPERIMENTAL METHODS AND DATA REDUCTION

5.1 Total Pressure Measurements

Total pressure measurements were conducted using a constructed pitot pressure probe. A Kulite pressure sensor was flush mounted in precision stainless steel tubing. Three sections of increasing diameter tubing were connected with epoxy-smoothed transitions to bring the outer diameter to 0.6 cm ($1/4$ in). The pitot probe could then be mounted in a sting assembly to position it in the test section. The kulite sensor was sampled at 300 kHz and the signal was low pass filtered at 50 kHz before being recorded on the computer's data acquisition (DAQ) system.

5.1.1 Nozzle Exit Traverse and Data Reduction

Total pressure measurements were taken along the centerline of the nozzle exit plane in vertical and horizontal directions. The pitot pressure probe was mounted in a sting assembly with a sharp leading edge. The sting was attached to a manual transition stage outside of the tunnel through a sliding seal in order to allow movement of the probe in a single direction during operation of the tunnel. The sting assembly could be mounted to the top of the tunnel for vertical movement or the side-wall of the tunnel for horizontal movement. A schematic of the vertical (standard) orientation is shown in fig. 5.1.

50 runs were recorded at each of 9 locations across the nozzle exit plane while the probe was moved manually using the transition stage. Target locations of the probe were measured with a ruler across the nozzle exit and marked on the transition stage, accuracy of the location of the probe is of the order 0.2 cm ($1/16$ in). For each location a 2 ms section of data was taken from each run in the region of stable pressure. The same 2 ms section of data from the settling chamber pressure was normalized against itself and used to correct the pitot signal to account for shot-to-shot influences over time. This was done for both vertical and horizontal rakes.

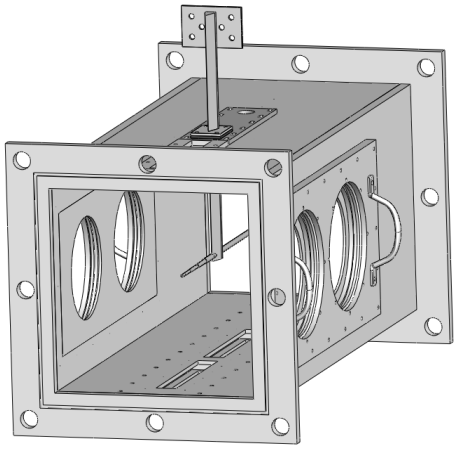

Figure 5.1: Schematic of pitot pressure probe traverse system in vertical orientation.

5.1.2 Freestream Pressure Measurements and Data Reduction

Total pressure measurements were recorded with the pitot pressure probe in conjunction with freestream optical techniques, described below. The pitot probe was statically mounted inside the test section positioned along the center-line in the vertical direction and just offset from center in the horizontal direction. This prevented probe interference with the optical techniques occurring along the horizontal center-line of the tunnel. A schematic of the experimental setup is shown in fig. 5.2.

Roughly 500 tunnel runs were taken at each Reynolds condition and a 4 ms section of data in the region where optical diagnostics typically occurred was extracted from each run. A trend removal routine was performed so that auto-correlation could be performed on zero-average data. The routine fit a second order polynomial to each 4 ms data section using a least squares procedure. The fitted values were subtracted from the original data values and then the data was broken into 150 data point windows. The normalized auto-correlation function (5.1) was determined for each data window and averaged over the number of windows, then over the number of runs, for each lag number.

$$\hat{r}(\tau) = \frac{\frac{1}{t_f-\tau}\sum_{t=t_0}^{t_f-\tau}[P'_{t2}(t)P'_{t2}(t+\tau)]}{\sum[P'^2_{t2}]} \tag{5.1}$$

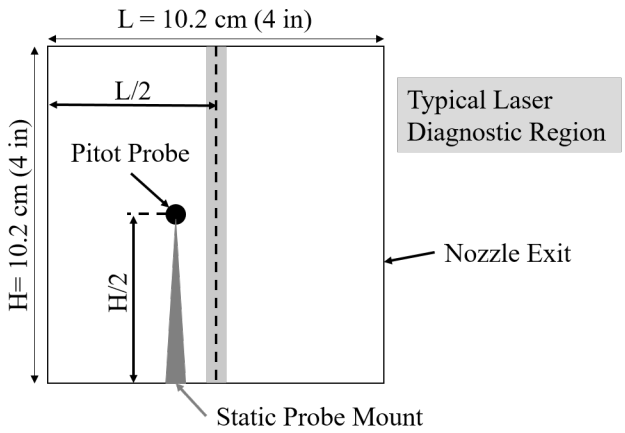

Figure 5.2: Schematic of experimental setup for freestream total pressure measurements. Flow is into the page, and the probe is shown statically mounted offset from the center-line to avoid the optical measurement region.

The normalized auto-correlation for each Reynolds number was plotted (fig. 5.3) and a numerical integration was applied to the initial lag region leading to the first zero-crossing using a trapezoidal method (fig. 5.4). The integral timescale was estimated from the numeric integration, and then the integral length scale was estimated with the mean velocity through Taylor's hypothesis. A parabolic fit was also applied to the first two points of the auto-correlation to estimate the Taylor microscale, an example of which is shown in fig. 5.5. Again, the first zero crossing was used to obtain the time scale, and then the length scale was estimated by multiplying with the mean velocity.

5.2 Laser Diagnostic Measurements

The bulk of experiments in this work were performed using optical techniques. The laser systems are described below, followed by details of the laser diagnostic techniques and data processing routines.

5.2.1 Laser System Description and Wavelength Calibration

Two identical pulsed laser systems were used in this study for excitation of nitric oxide in various LIF techniques. Each system consisted of an injection seeded Spectra Physics PRO-290-

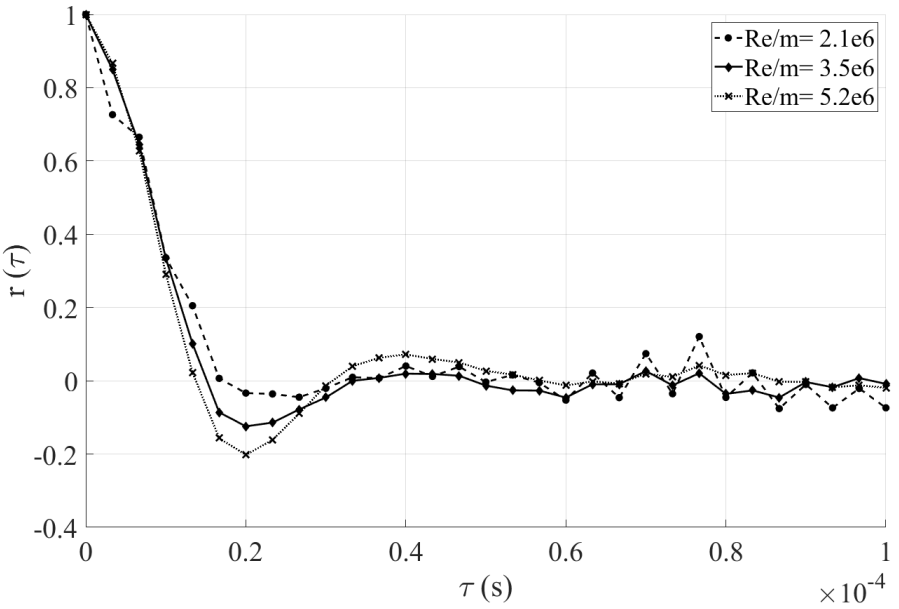

Figure 5.3: Auto-correlation functions for total pressure measurements at three Reynolds conditions.

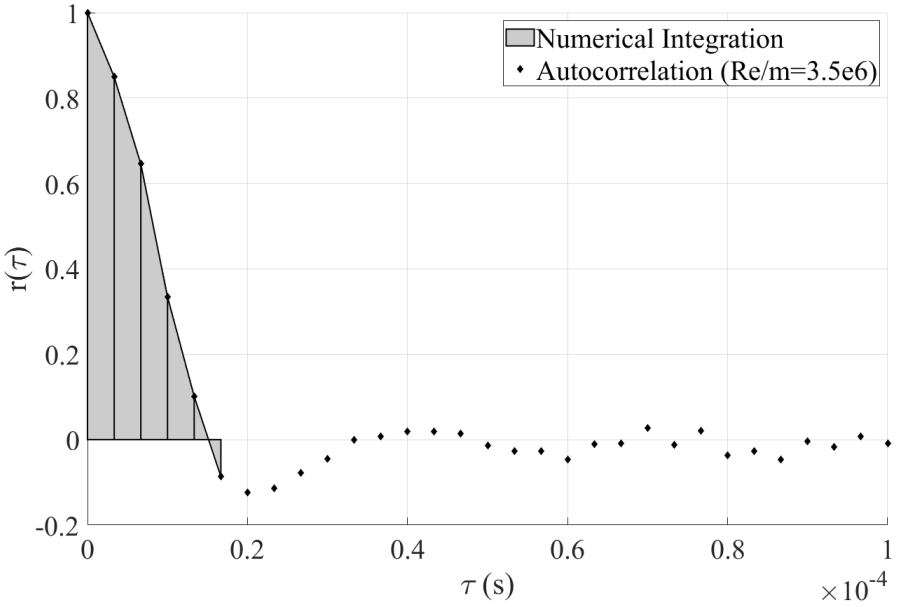

Figure 5.4: Example of numeric integration of the auto-correlation function using a trapezoidal method.

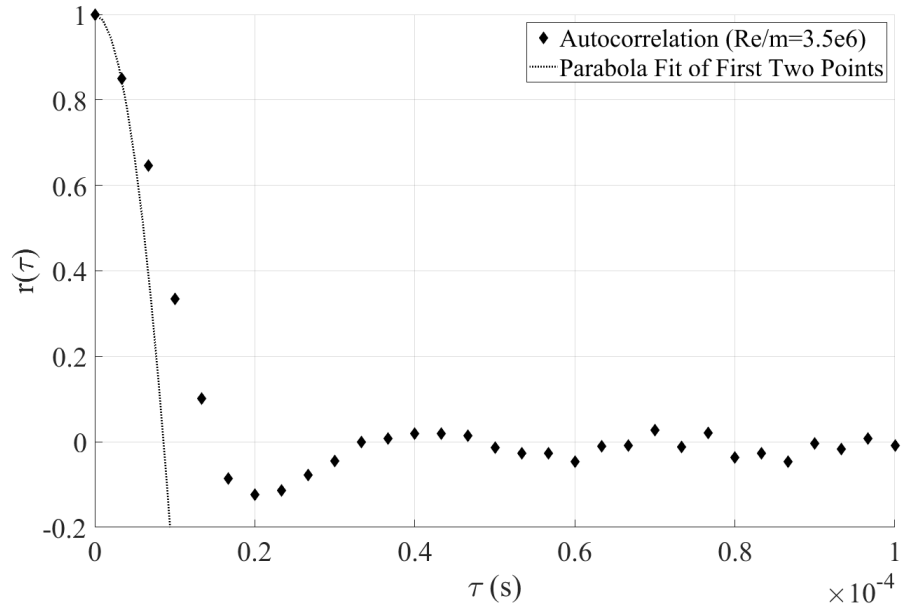

Figure 5.5: Example of parabolic fit of first two points of the auto-correlation function.

10 Nd:YAG laser and a Sirah Cobra Stretch dye laser with a sum frequency mixing unit (fig. 5.6). The YAG laser operated at 10 Hz with a linewidth of 0.003 cm^{-1}, and was tuned for output in both second and third harmonics (532 nm and 355 nm respectively). A fundamental beam was generated in the dye laser by pumping a dye solution consisting of Rhodamine 610 and Rhodamine 640 in methanol with the first harmonic output of the YAG. The resulting fundamental beam was tunable in the range of 600nm to 630nm by adjustment of a grating optic. The dye fundamental beam was them mixed with the third harmonic output from the YAG in a Sirah SFM-355 mixing unit, resulting in an ultraviolet (UV) 223 nm to 227 nm output beam. Typical linewidth and power of the UV beam was 0.08 cm^{-1} and 5-12 mJ/pulse respectively.

The UV wavelength was calibrated in a low pressure test cell. The configuration of the calibration setup is shown in fig. 5.7. The output beam of the dye laser was diverted into a cylindrical test cell. Windows on both ends of the test cell were oriented at 45 degree angles to the incident beam to reduce internal reflections. Pressure ports were located at the center of the cell connecting to a low pressure supply of 1-5 % NO in N2 at the inlet and to a vacuum pump at the outlet. A scien-

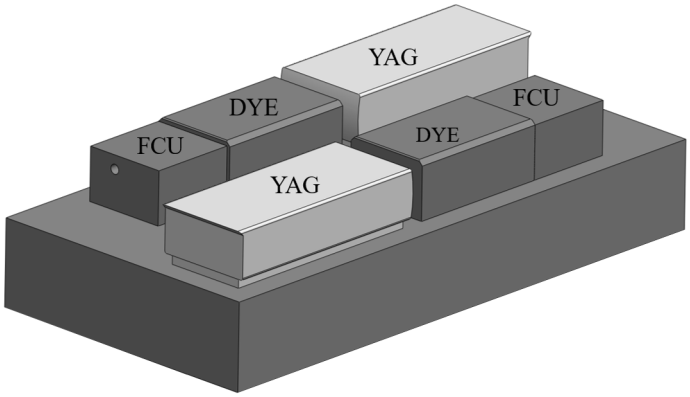

Figure 5.6: Diagram of pulsed laser system setup.

tific valve at the inlet allowed controlled flow of the NO mixture into the cell to achieve a constant pressure. A window was installed at the center of the cell for optical access of a photo-multiplier tube (PMT). Signal from the PMT was recorded on an oscilloscope and sent to a PC computer. A photo-diode mounted near the laser beam exit path was used to trigger the oscilloscope to capture the NO fluorescence signal.

A custom wavelength scanning program, written in Labview, was used to perform the calibration. The program remotely controlled the dye laser output by updating the grating orientation for the fundamental beam. In a typical wavelength calibration, the program would step the laser through a series of wavelengths and record the signal from the oscilloscope at each step. In order to smooth the experimental spectrum and account for shot-to-shot inconsistency, 10 recordings were taken at each wavelength step and averaged. The averaged spectrum was then normalized and compared with the LIFBASE spectral simulation program to determine the overall wavelength shift of the laser. The simulated excitation in LIFBASE was also used to determine wavelengths for the target NO(0,0)and NO(1,1) transitions used in the following experiments.

5.2.2 Molecular Tagging Velocimetry: Experimental Approach

Velocity measurements were made across a normal shock using a single component molecular tagging velocimetry approach. The experimental configuration is depicted in fig. 5.8. The model wedges were installed flush with the exit plane of the nozzle and spaced 5.1 cm (2 in) apart

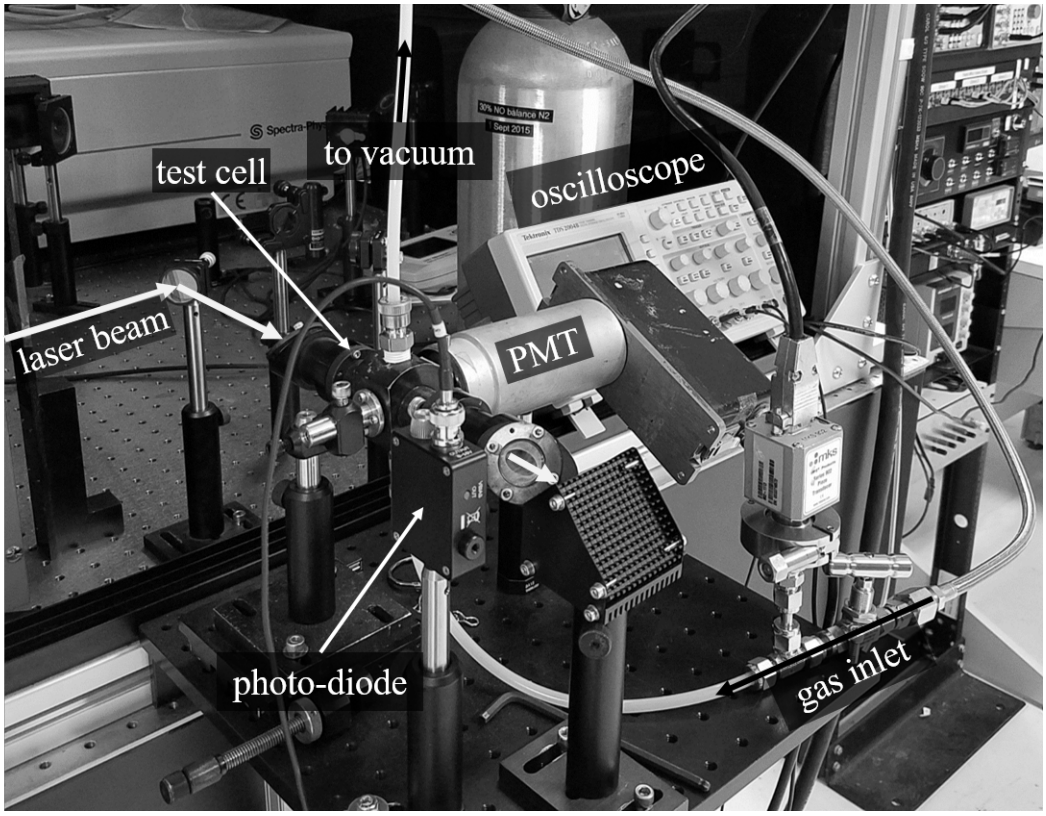

Figure 5.7: Laser wavelength calibration test cell setup.

vertically. The optimal vertical spacing for the wedges was determined via flow visualization techniques (described in section 5.3), where the Mach stem's height was maximized while remaining downstream of the wedge geometry. A Pitot pressure probe was mounted outside of the laser diagnostic area, in the lower corner of the core flow, to monitor tunnel conditions. A Princeton Instruments PI-MAX4 ICCD camera was mounted for viewing from the right hand side of the tunnel.

Two lasers were used in the MTV technique, one "write" laser to initially excite the ground state NO, and one "read" laser that would later target the tagged v"=1 NO. Images for MTV processing were taken of the initial laser grid and a single time delayed 'read' signal. The "write" laser was sent through a cylindrical micro-lens array to separate and focus the beam into multiple discrete lines. These lines were brought into the diagnostic area through the top window of the test section and aligned in the vertical direction, parallel to the normal shock wave. The "read" laser

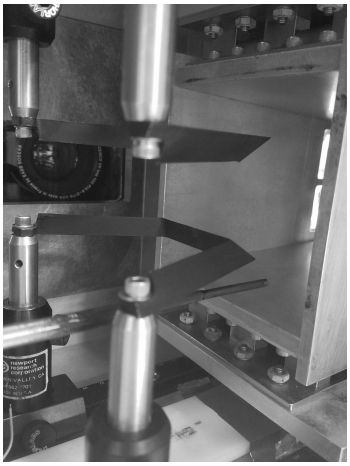

Figure 5.8: Model wedge configuration for MTV and PLIF Thermometry experiments.

was sent through a cylindrical lens to form a sheet parallel with the flow direction and brought in through the top window at a minimal angle to the "write" laser to maximize overlap. The final turning mirrors and sheeting optics for both lasers were mounted to an optical breadboard, which in turn was mounted to a linear transition stage on a rail system. The rail system included statically mounted turning optics to bring both lasers into alignment with the tunnel test section. A diagram of this setup is shown in fig. 5.9. The linear transition stage was used to optimize the location of the "write" laser lines in relation to the normal shock wave during operation of the tunnel. The camera gate would be set to 100 ns exposure so that signal from the scattered laser between the focused lines could be detected, allowing the shock wave location to become evident. The transition stage would be adjusted until the "write" line was just downstream of the shock wave, usually with a separation of roughly 5 pixels. Once the lines were in optimal location, the transition stage was locked to prevent accidental motion.

The tunnel N2 supply was pre-seeded with 0.5-1.0 % NO and pre-heated to achieve 375 K in the tunnel settling chamber. The initial laser was timed at 30-32 ms following initial tunnel valve opening and the second laser followed at a 1.7 μs time delay. In MTV, the velocity uncertainty scales directly with distance uncertainty. Increasing the time delay between images will allow the line to travel farther and uncertainty in distance traveled will decrease. This is generally limited

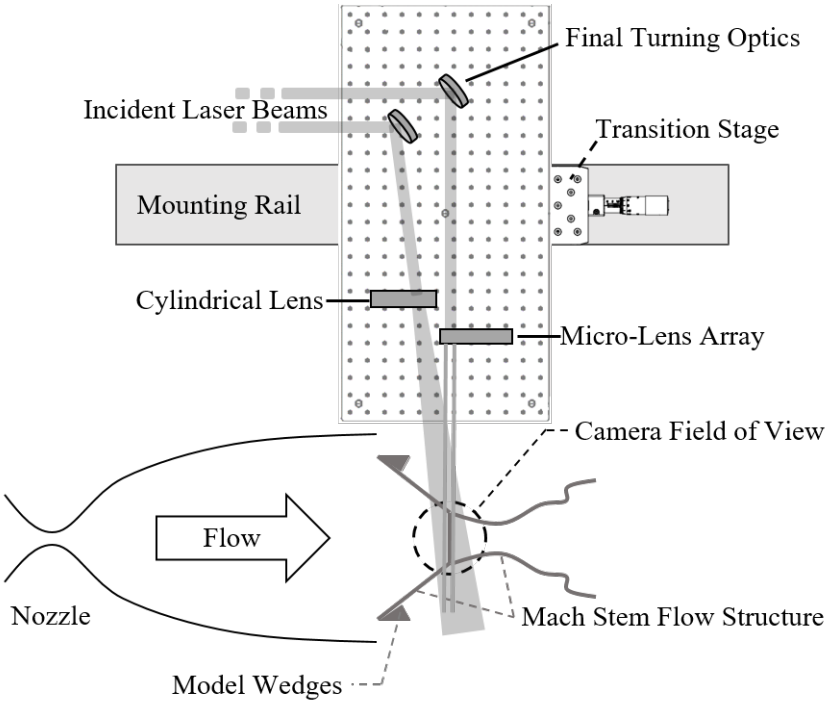

Figure 5.9: Diagram of experiment setup for MTV measurements.

to not allow the lines to cross each other, so that, in image reduction, the interrogation window can remain stationary. In the case of this study, the time delay was set such that the written line in the freestream would almost reach, but not touch, the normal shock wave. The camera was liquid cooled to -35 C with the intensifier enabled. The dual image feature setting was used and camera gates were set for 3 ns exposure of the initial image and 100 ns exposure of the second image. Due to the large difference in signal strength from the "write" and "read" lasers the second exposure had to be much longer than the initial exposure to be comparable in image processing. Typically this can be avoided by introducing a second "read" laser at another time delay and capturing only the two delayed images. The two delayed images will be of roughly equal intensity so the exposure gates can be shortened to limit the line spreading during exposure. A third laser system was not available for these experiments, thus, the camera followed the "write" and single "read" sequence. A timing schematic of this process is shown in fig. 5.10.

For each Reynolds number condition a series of images would be taken. First a dotcard image

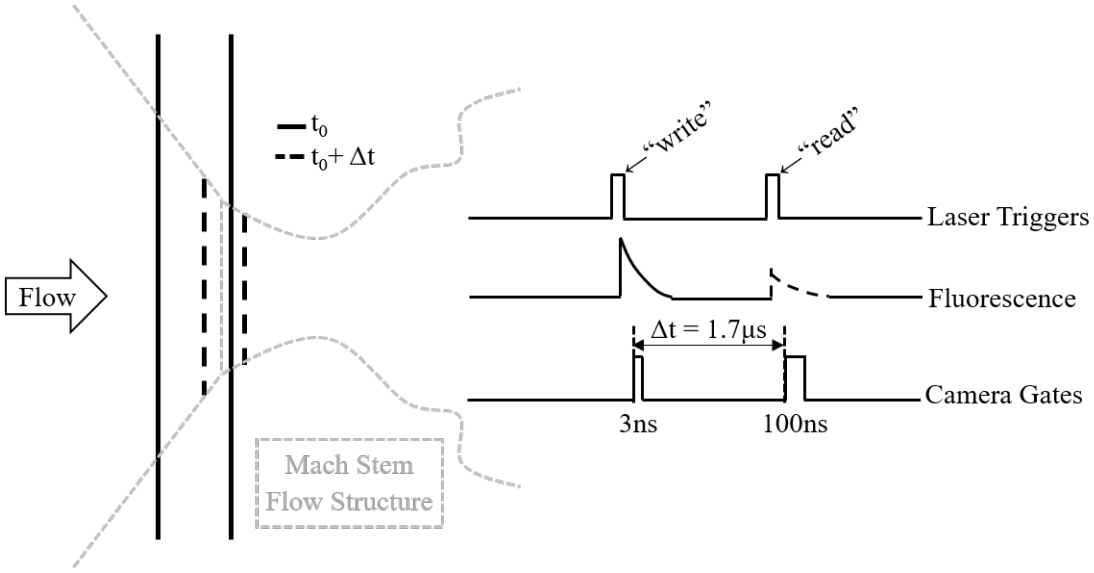

Figure 5.10: Laser and camera gate timing schematic for MTV experiments.

was taken to align and focus the camera on the laser excitation region, as well as provide a distance conversion factor to be used in post processing. The background intensity was corrected by taking a 'dark-charge' image of the covered camera lens and subtracting this from each frame. In order to confirm the location of the shock wave in post-processing, a long term PLIF exposure of NO(0,0) was recorded and averaged over 100 frames. Finally, the MTV images were recorded at several locations. 500 image pairs were taken in the 'optimal' position described previously. The transition stage would then be adjusted to shift the laser lines 5-10 pixels farther downstream, and 500 image pairs were taken at the new location. This was repeated until 4 total locations had been recorded. The images were then processed as described in the following section.

5.2.3 Molecular Tagging Velocimetry: Image Processing

All velocimetry images in this study were processed using a custom program written in Matlab. The image processing program consisted of several sub-routines for processing the dotcard, shock location, and MTV image pairs. Inputs to the program allowed the user to specify the experimental conditions, such as pressure and temperature data from sensors in the tunnel, as well as the time delay between image pairs and folder locations of the various images to be processed. Additionally,

there were controls for thresh-holding images, selecting and sizing the correlation region, and specifying a goodness-of-fit cutoff for the cross-correlation results. A breakdown of the processing routine is listed below, and a more detailed description follows.

- Dotcard subroutine
  - Invert dotcard image
  - Create horizontally and vertically binned images
  - Determine location of peaks
  - Calculate pixel-to-meter conversion factor
- Shock location sub-routine
  - Crop and bin image to experimental settings
  - Adjust contrast to binary 1 downstream of shock
  - Record shock x-location for each row
- Cross-correlation sub-routine
  - Find rough location of lines in average write image
  - For each coordinate pair:
    - Create sub-images around line location coordinate pair
    - Threshold sub-image pair
    - Cross-correlate
    - Fit cross-correlation with polynomial function
    - Return 'lag' and goodness-of-fit
  - Repeat for each image pair
- Post process
  - Calculate velocity from lag and pixel-to-meter conversion
  - Determine mean and fluctuating values with goodness-of-fit exculsions

The first sub-routine of the program used a dotcard image to correlate pixel length to physical length. The dotcard image was processed by first inverting the intensity and adjusting the contrast.

The image was binned in the vertical and horizontal directions and a user specified cutoff was then used to isolate the peaks in intensity. Example line plots for the vertical and horizontal intensity profiles are shown in fig. 5.11a. A search for local maxima was performed for each line plot (shown overlaid on the dotcard image in fig. 5.11b) and the average number of pixels between peaks was calculated. Using the known dotcard line spacing of 2.5 mm, a pixel-to-meter conversion was recorded for the horizontal and vertical directions.

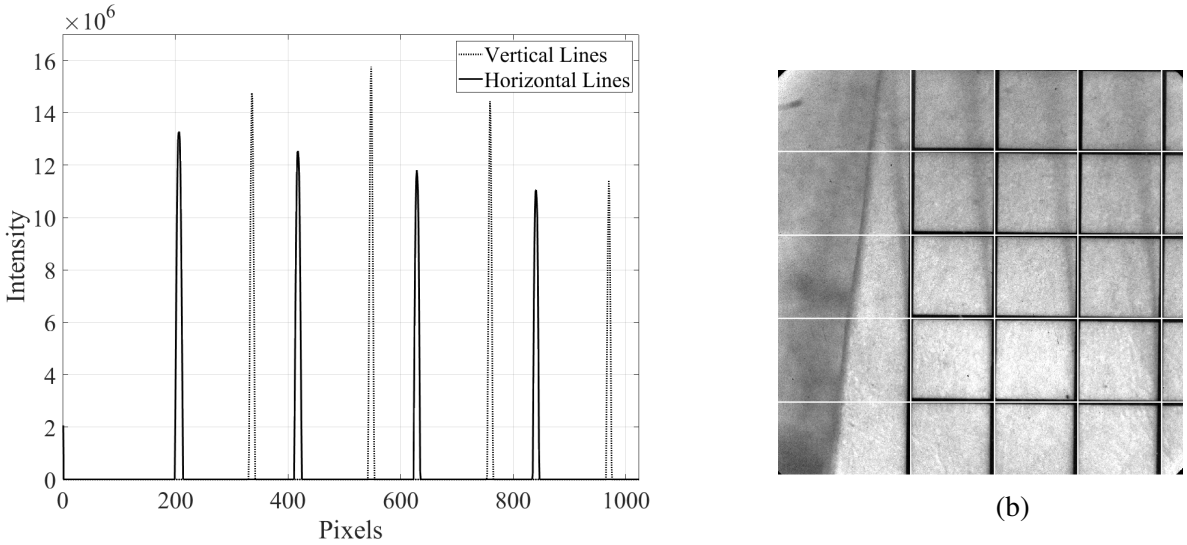

Figure 5.11: Example of dotcard image processing routine. A plot of horizontal and vertical intensity profiles (a), and the resulting peak locations overlaid on the original dotcard image (b).

The next sub-routine determined the exact shock location so that velocity magnitudes and fluctuations could be interpreted in reference to the distance downstream of the shock wave. The PLIF "shock-locator" image was processed by first selecting the close region where the shock was known to be within the overall image. The sub-image was then contrast adjusted so that freestream signal would go to zero-value, and the x-location of the first non-zero value at each y-location was recorded. An example of this procedure is shown in fig. 5.12, where the contrast adjusted image is shown to the left and the resulting shock location is overlayed on the raw image to the right.

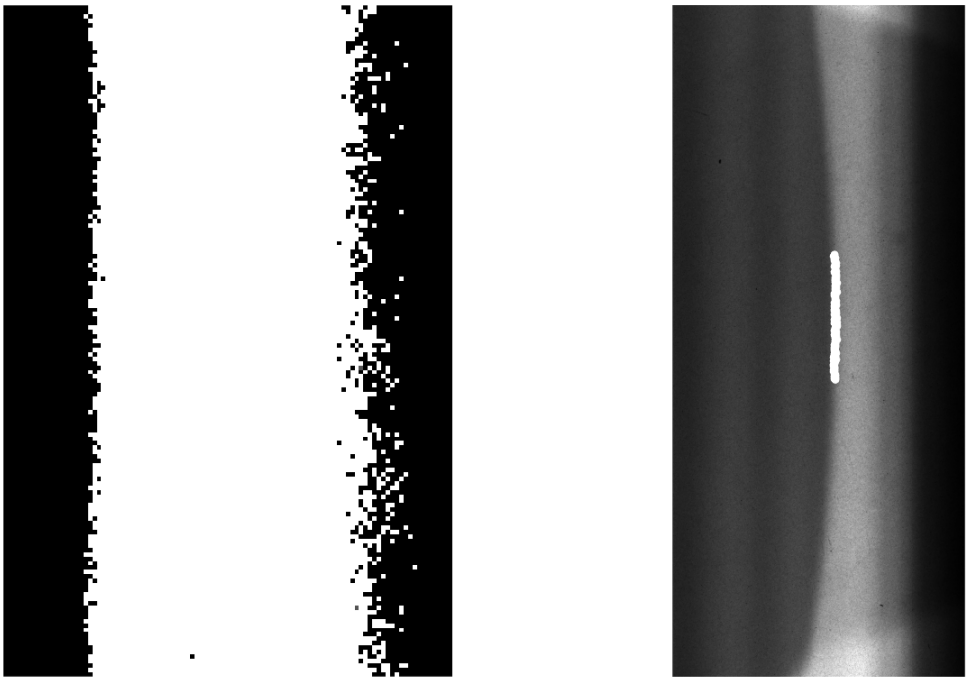

Figure 5.12: Example of shock locating routine. The contrast-adjusted shock region shown to the left, and the resulting shock location shown overlaid on the original image to the right.

The final sub-routine performed the cross-correlation for velocity determination. First, the approximate location of the 'write' lines was found by locating extrema in an average image of the time-zero image set. The average image was generated by calculating the 500 sample mean at each pixel location. A threshold value was then subtracted from the entire image and a gaussian filter was used to smooth the image. For each y-pixel row, the x-locations of the local maximums were recorded. A binary image of the maxima locations could be compared to the original average image, and threshold and filter values could be adjusted as needed to remove spurious points. The line locations were then recorded as coordinate pairs in a matrix.

The sub-routine would then iterate a cross-correlation routine for each coordinate pair in the line location matrix. A sub-image pair wold be generated at the coordinate location by cropping the raw initial and time delayed image pair into a single pixel height region surrounding the coordinate pair. The x-length of the sub-images was defined by a "half grid" variable that the user could input, generally defined as half the pixel distance between two written lines. Individual threshold

values would then be subtracted from each sub-image so that background signal would not affect the cross-correlation results.

The built in "x-corr" Matlab function was then applied to the sub-image pair. The resulting correlation matrix was cropped around the peak value and fitted with a third order polynomial with centering and scaling applied. A goodness of fit (r^2) value was recorded for the correlation function so that the user could remove poor correlation results. An example cross-correlation result is shown in fig. 5.13. It was found that the correlation fit would underestimate the correlation peak value in most cases with the polynomial fit. While the peak value itself is not meaningful, in order to make sure the location of the peak was as accurate as possible a secondary fitting procedure was applied. If the initial polynomial fit returned a goodness of fit value above a user specified threshold (typically 0.95), the application would crop even closer around the peak and perform another polynomial fit. Including more points initially allows for poor correlations, without strong peaks, to be excluded from further processing; and it was found to be within 0.5 pixels of the true peak. The secondary fitting further reduced this uncertainty to 0.1 pixels.

The recorded sub-pixel correlation peak was then converted to a distance value by multiplying the earlier determined pixel-to-meter conversion factor. This value was then divided by the user specified time-delay from the experimental settings to obtain a velocity value. This was repeated for all coordinate pairs in the matrix, across each image pair recorded in the series. The velocity and goodness of fit values were then sent to post-processing where mean and fluctuating values could be determined across the region of interest.

5.2.4 PLIF Thermometry: Experimental Approach

Temperature measurements were made across a normal shock wave by a two-line PLIF thermometry technique. The model wedges were installed in the same configuration as the MTV experiments, leading edges flush with the exit plane of the nozzle and spaced 5.1 cm (2 in) apart vertically (fig. 5.8). A Pitot pressure probe was mounted outside of the laser diagnostic area, in the lower corner of the core flow, to monitor tunnel conditions. The tunnel N2 supply was pre-seeded with 0.5-1.0 % NO and pre-heated to achieve 375 K in the tunnel settling chamber. For the nominal

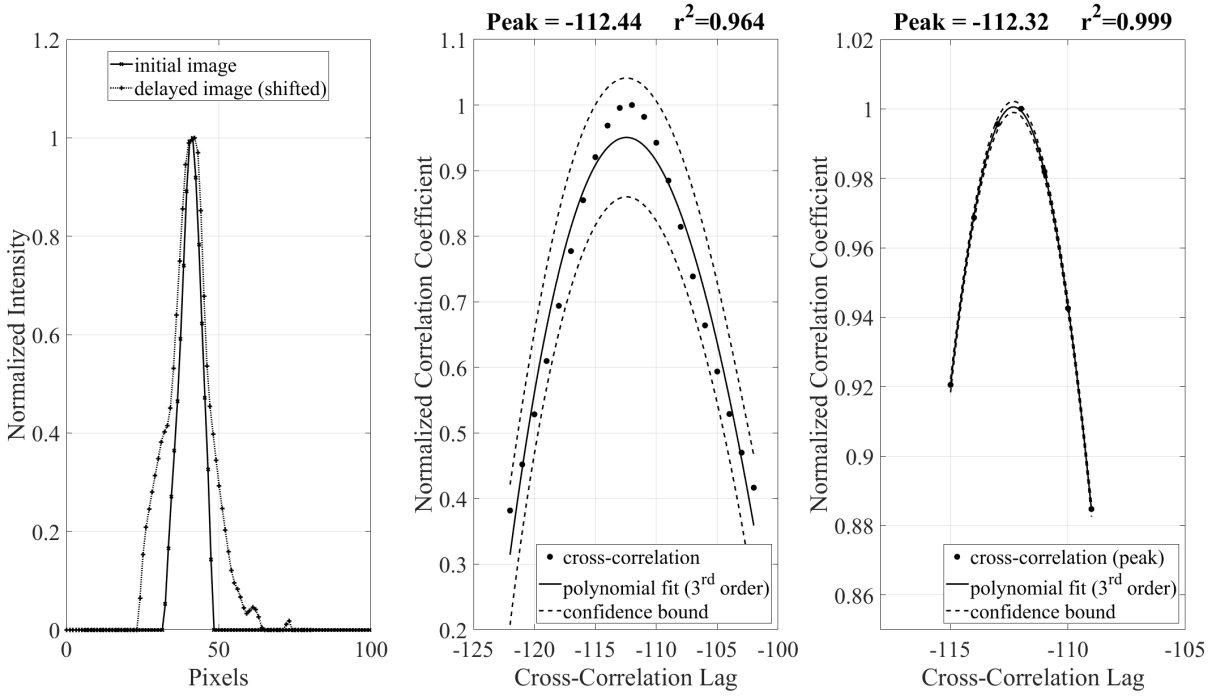

Figure 5.13: Cross correlation example of a random sub-image pair. The far left figure shows the normalized and thresholded sub-images, where the delayed image has been shifted by the correlation peak. In the middle is the primary cross-correlation fit, and to the right is the secondary cross-correlation fit. Each is cropped around the peak value. A third order polynomial fit is applied with 95% confidence bounds, and the resulting peak and goodness-of-fit r^2 value are displayed at the top.

flow Mach number of 4.4, the expected mean temperature conditions were 77 K in the freestream and 361 K downstream of the normal shock wave. The "read" lasers in this study were tuned to probe transitions in the $A^2\Sigma^+(v'=0) - X^2\Pi(v''=0)$ band for ground state NO. Target rotational states were chosen based on the Boltzmann population distributions of ground state NO at the two expected temperatures, shown in fig. 5.14.

Temperature sensitivity in PLIF is achieved by maximizing the spacing between rotational states. Applying uncertainty analysis to the PLIF temperature equation, derived previously in section 2.2.3, it can be seen that temperature uncertainty scales inversely with the energy separation of the states (5.2). Additionally, it is advantageous for ΔE to be of the same order of magnitude

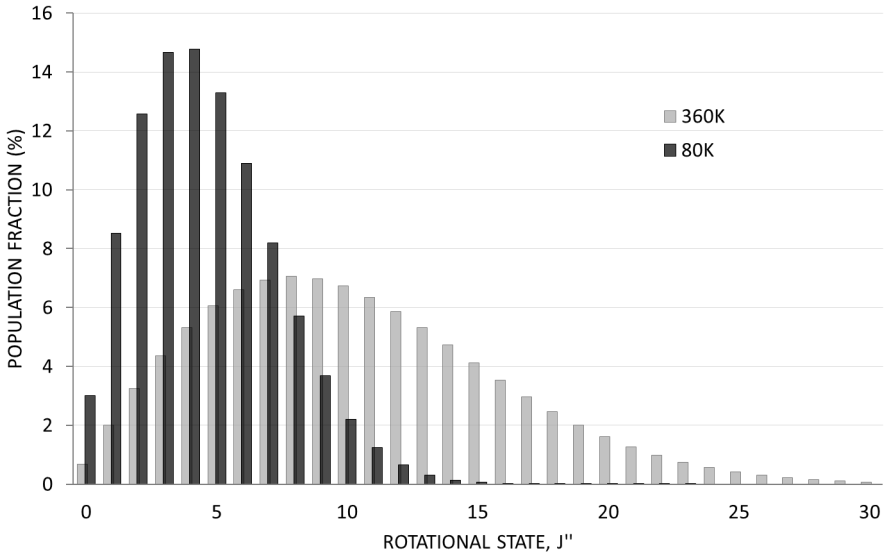

Figure 5.14: Boltzmann population fractions for ground state NO at expected experimental temperatures.

as kT so that temperature uncertainty will scale directly with image-ratio uncertainty.

$$\frac{\delta T}{T} = \frac{kT}{\Delta E}\frac{\delta R}{R} \tag{5.2}$$

Another factor in thermometry, particularly in low temperature conditions, is the signal-to-noise ratio limit. While, in theory, the rotational state extremes will produce the highest temperature sensitivity, there must be a practical balance with the population fractions of the chosen lines such that measurable signal will be produced in all regions of the flow. By scaling the Boltzmann population fraction with the expected number density, the relative fluorescence potential can more clearly be seen. In the case of this study, the nozzle expansion process was expected to produce a low temperature and low density freestream environment. Once the flow passed through the normal shock, both temperature and density were expected to increase dramatically. The scaled population density in fig. 5.15 shows the effective signal potential upstream and downstream of the normal shock. From this figure, it is clear that the freestream flow region would present greater limitations in SNR. The rotational states $J'' = 1$ and $J'' = 8$ were chosen to maximize temperature sensitivity,

particularly in the region downstream of the normal shock, while retaining reasonable signal potential from both regions of flow. Laser wavelengths were set for these rotational states following the calibration procedures described previously and the power was balanced to 1.5 mJ/pulse for both lasers.

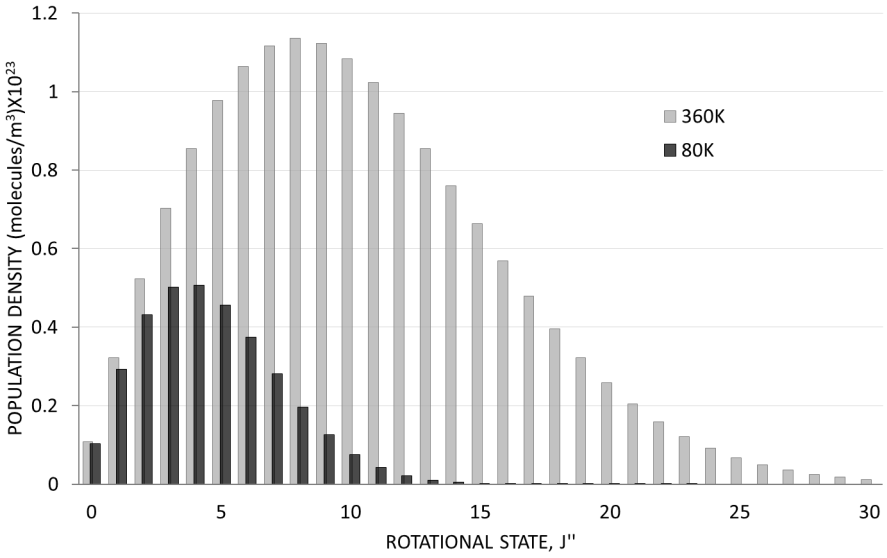

Figure 5.15: Scaled Boltzmann population density for ground state NO at expected experimental conditions.

A schematic of the experimental setup for PLIF thermometry is shown in fig. 5.16 below. Both lasers were introduced through the top window of the tunnel. In order to optimize the overlap of the laser sheets, the angle between the beams was minimized by mounting the final turning mirrors as close to each other as possible without clipping the beams. Both lasers were sent through a cylindrical lens to alter the circular profile into a planar sheet oriented in the direction of flow. A Princeton Instruments PI-MAX4 ICCD camera was mounted on the right hand side of the tunnel for image collection.

The first laser was timed at 30-32 ms after the initial valve opening, followed by the second laser with $1.7\mu s$ time delay between, for consistency with the velocimetry measurements. The

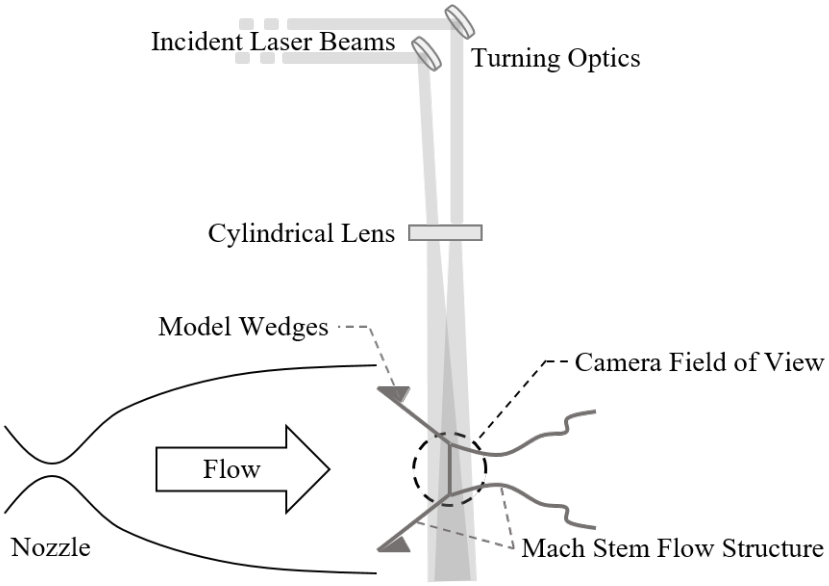

Figure 5.16: Diagram of experimental setup for PLIF thermometry.

camera was liquid cooled to -35 C with the intensifier enabled. Images were taken using the dual image feature setting with 10-15 ns gates. A dotcard image was taken first, to focus the camera on the plane of the laser sheets. The background intensity was corrected in-situ by subtracting a "dark-charge" image of the covered camera lens from each frame. 500 image pairs were taken of the normal shock region for each Reynolds number condition and processed as described below. This was repeated for the same region of flow with the model wedges removed to further characterize the freestream conditions. Additional image pairs were taken in regions of known temperature for calibration and image correction purposes during processing.

5.2.5 PLIF Thermometry: Image Processing

Thermometry images were processed using a custom application, written in Matlab. Free-stream images were initially processed following a conventional approach for linear LIF thermometry to establish baseline conditions. Details of this approach can be found in Appendix B. It was believed that the high temperature and density downstream of the shock, coupled with the necessary laser intensity to obtain signal in the freestream, led to a non-linear response in the Mach stem flow. A separate processing routine was written to examine Mach stem PLIF images, where

each region of the flow was individually analyzed for an assumed mean temperature based on the previously established conditions. Because the quantities of interest in this study were fluctuations, and the mean flow conditions are well known conventionally, it was determined that this 'in-situ' processing would be sufficient for the scope of this analysis.

The non-linear processing routine analyzed the upstream and downstream locations as separate images. Calibration images were not used in this routine. Instead, a mean temperature was assumed based on the previous freestream measurements and conventional shock-jump relations. The calibration constant was then specified to match this assumed temperature for the R_{12} values at each pixel. This temperature specification method essentially acts as a laser profile correction step, combined with a temperature calibration, as is typically seen in the conventional linear approach. The non-linear application is listed below, followed by a more detailed description of the procedure.

- Bin image if needed and select region of interest
- At each pixel for freestream and downstream respectively
  - Find range of R values, excluding outliers
  - Calculate temperature for a range of C12 and the given R values
  - Find C12 that returns a mean temperature closest to the user specified value
- Calculate temperature at all points
- Post process each pixel
  - Find range of temperature, excluding outliers
  - Calculate mean and fluctuating temperature

The first step of the non-linear routine allowed the user to select the regions of interest and specify the temperature for each region. The raw images were cropped to view only the normal shock region with fluorescence signal, and then a region in front of and behind the normal shock was selected for further processing. Next the images would be binned in two dimensions for both pre- and post-shock regions. The user could select a desired bin size of 1x1 (no binning) up to

12x12 pixels. The mean value of the pixels within each bin, excluding negative or "not a number" values, would be recorded and returned as the value for the entire bin.

Each pixel would then be analyzed individually. The R_{12} values from all image pairs at each pixel were first analyzed to remove outliers. A plot of R_{12} values for an example pixel coordinate (15,200) is shown in fig. 5.17. A $C_{12}{}'$ value was then selected such that the resulting mean temperature, calculated for the range of R values, would match the specified mean temperature of the region. This was done through manipulation of the standard PLIF thermometry equation to find "$\langle C_{12}{}' \rangle$" based on the given R_{12} range and specified mean temperature (5.3).

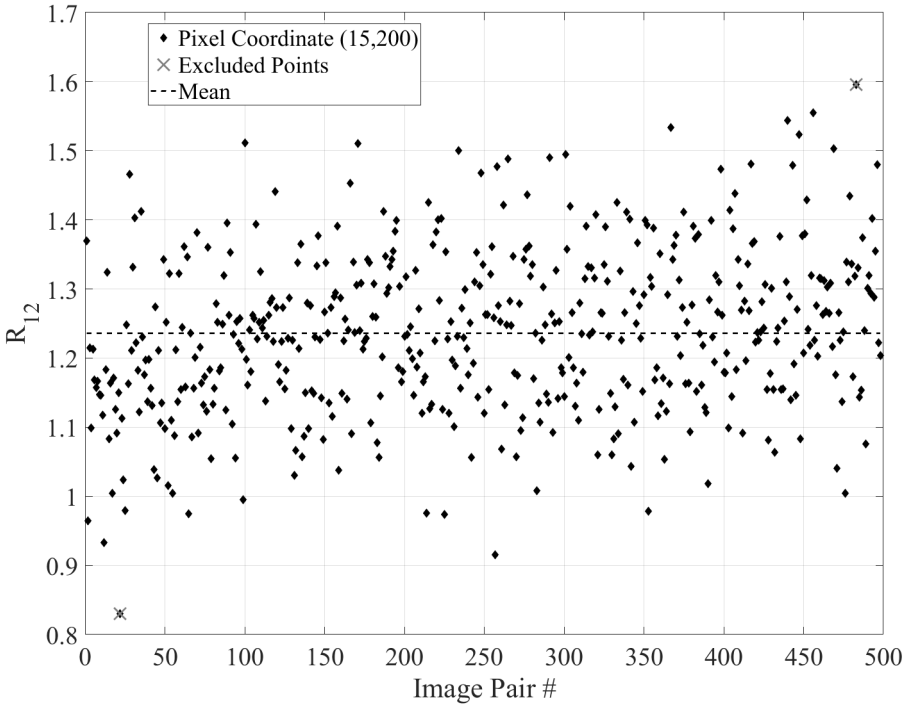

Figure 5.17: Plot of R_{12} values at pixel coordinate (15,200) in the region downstream of the normal shock wave. Excluded outlier values are shown as with an overlaid 'x'.

$$\langle C_{12}{}' \rangle = \left\langle e^{\left(ln(R_{12}) + \Delta E/k\overline{T}\right)} \right\rangle \tag{5.3}$$

Due to the inverse logarithmic response of temperature to (R/C), this method of $C_{12}{}'$ determi-

nation is necessary to avoid falsely skewing the mean temperature. Shown graphically in fig. 5.18, when a single C value is selected, a range of temperature values can be determined based on the range of R values. One cannot simply select a C value associated with the mean R value, else the temperature range will skew high compared to the specified mean temperature.

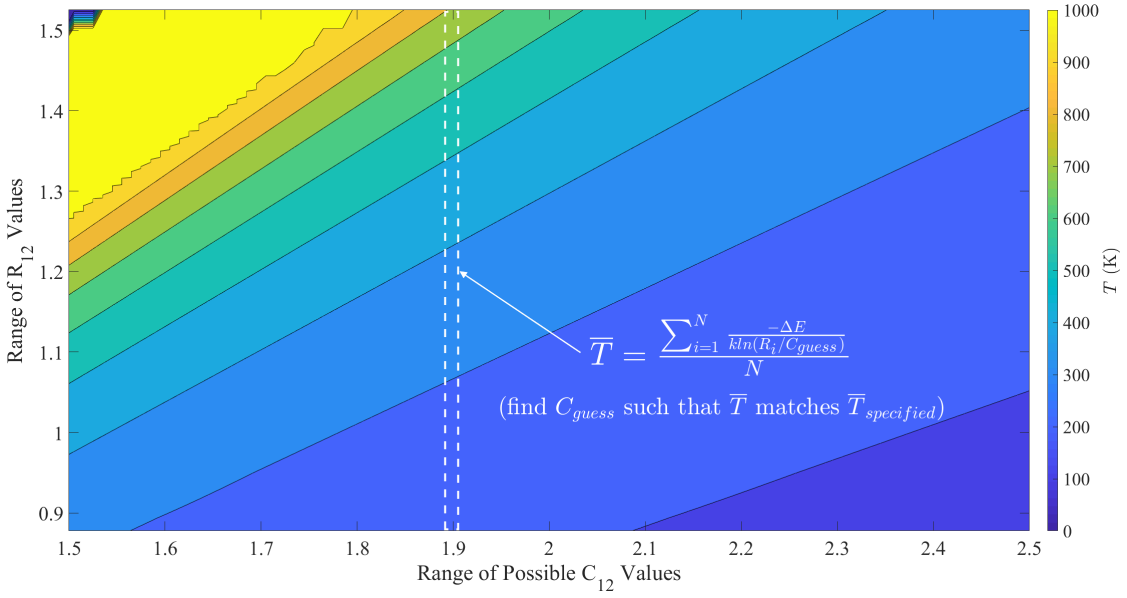

Figure 5.18: Contour plot of temperature over of the range of R_{12} and potential C_{12} values. A graphical description of the process for determining C_{12} is shown with an example of calculating a mean temperature from a guessed C value across the range of R values.

Once the appropriate $C_{12}{}'$ value was determined for a given pixel coordinate, temperature values for each image pair at that coordinate were calculated and recorded. This was repeated across both regions of interest, and the resulting temperature data was sent to post processing. Mean and fluctuating temperatures were analyzed for each region, the results of which are discussed in the next section.

5.3 Flow Visualization

Flow visualization was performed using both Schlieren and PLIF techniques. The schlieren system was setup in a z-type configuration, as shown in fig. 5.19, using a Unertl Optical Company

AMC149079 light source and a Cooke PCO 1600 camera with a horizontal knife edge. Images were taken at various time points in the flow to determine Mach stem formation, height, position, and growth. Optimal wedge spacing was determined by maximizing the Mach stem height while maintaining its position behind the wedge body for optical access. Additionally, the stability of the Mach stem was explored and target test times were indicated for the time of zero-growth. Finally, PLIF images were captured to further characterize the Mach stem flow at each Reynolds condition.

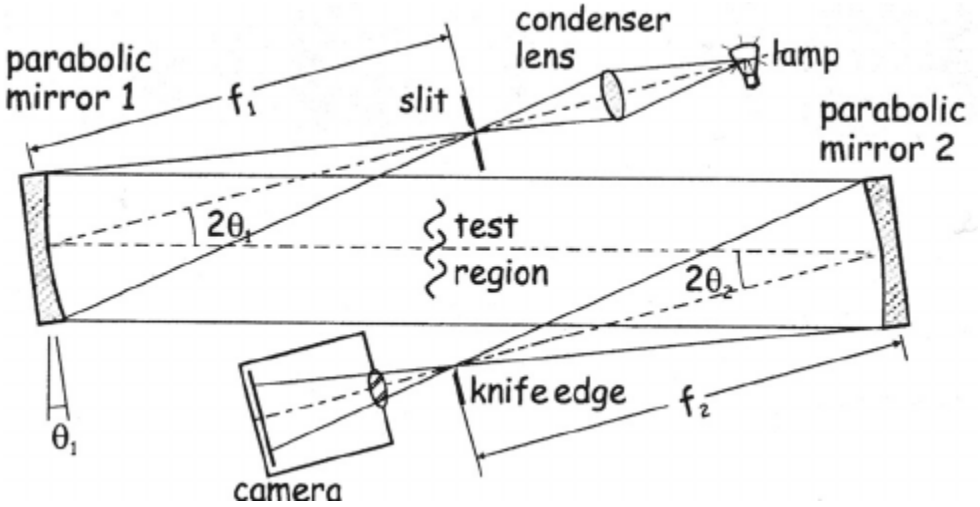

Figure 5.19: Z type configuration Schlieren setup (reprinted from Settles [72]).

6. DISCUSSION OF RESULTS

Table 6.1 shows a list of the experiments performed in this work. The results will be discussed in the following section.

Reynolds Number ($10^6/m$)	Settling Chamber Pressure (kPa)	Pitot Probe Pressure (kPa)	Shot-to-Shot Pressure RMS ($\%$)	Heater Exit Temperature (K)	Measurement
2.1	87.6 ± 1.0	8.2 ± 0.1	2.3	375	Freestream Velocimetry (1D)
3.5	145.1 ± 1.4	13.4 ± 0.2	1.4	374	
5.1	213.0 ± 1.8	20.1 ± 0.3	0.8	375	
2.1	86.0 ± 0.9	8.6 ± 0.1	not avail.	374	Mach Stem Velocimetry (1D)
3.5	145.3 ± 1.4	15.0 ± 0.2	0.6	374	
5.2	214.0 ± 1.7	22.1 ± 0.3	0.7	374	
2.1	87.0 ± 1.0	8.2 ± 0.1	0.8	374	Freestream Thermometry
3.5	145.1 ± 1.4	13.4 ± 0.2	1.4	374	
5.2	212.5 ± 1.8	20.5 ± 0.3	0.8	375	
2.1	86.8 ± 1.0	8.8 ± 0.2	0.7	$375*$	Mach Stem Thermometry
3.5	146.5 ± 1.1	15.1 ± 0.2	0.6	375	
5.2	212.5 ± 1.8	21.4 ± 0.3	1.0	$375*$	

Table 6.1: List of experiments and relevant tunnel conditions.(* Denotes a heater malfunction warning, the pebble bed heater PID loop was reset during tunnel operation and the supply temperature may have temporarily increased above the desired range.)

Total pressure data is explored first, with a discussion of freestream noise, turbulent scales, and expected conditions for the shock problem. A brief discussion of flow visualization follows, leading into results of the Mach stem MTV experiments. Mean and fluctuating velocities are analyzed across the shock, as well as amplification factors, for each Reynolds condition. PLIF results are then discussed, with an analysis of fluctuating temperature and amplification factors across the shock.

6.1 Total Pressure Characterization

Characterization of the freestream total pressure was performed in two parts, traversing a Pitot pressure probe across the center-line of the nozzle exit taking snapshots of data, and statically mounting the Pitot probe just offset from the center of the nozzle exit taking data over 500 tunnel runs. The total pressure was measured at nine location across the vertical and horizontal nozzle exit center-line. Following the procedure previously described, a section of data was analyzed for each location to determine the mean and fluctuating total pressure components across the nozzle exit plane. Plots of these are shown in fig. 6.1 and fig. 6.2 below. The uncertainty in the location of the probe at each point is of the order 0.2 cm. The model wedges, when installed, inhabit the area within $\pm$0.5 x/l and $\pm$0.5 y/h. Within this region, no significant anomalies in the mean or fluctuating total pressures are seen.

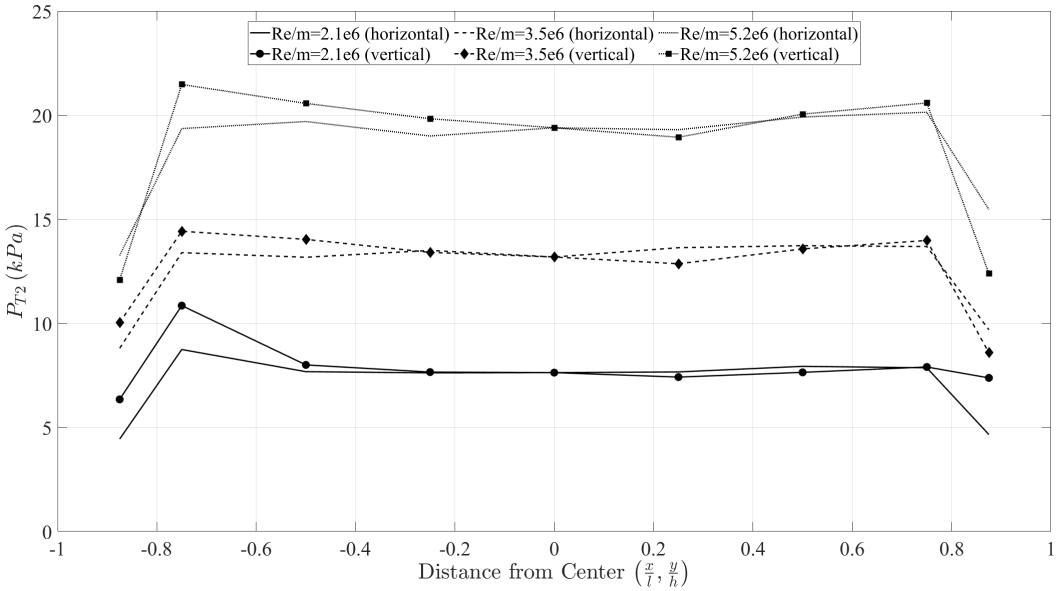

Figure 6.1: Total pressure traverse measurements for three Reynolds conditions in horizontal and vertical directions

Total pressure fluctuations are found to be 1.8-1.9 %, which is of the same order as seen in the ACE wind tunnel [67], as expected due to the similarity in design. One exception is the lowest

Reynolds condition, at Re/m=2.1e6. In ACE, this is reported to have reduced fluctuations. This trend is not found here, the total pressure fluctuations are consistent for all three cases, being marginally lower for the Re/m=2.1e6 case. This would imply that the nozzle experiences turbulent boundary layers at all conditions in this study.

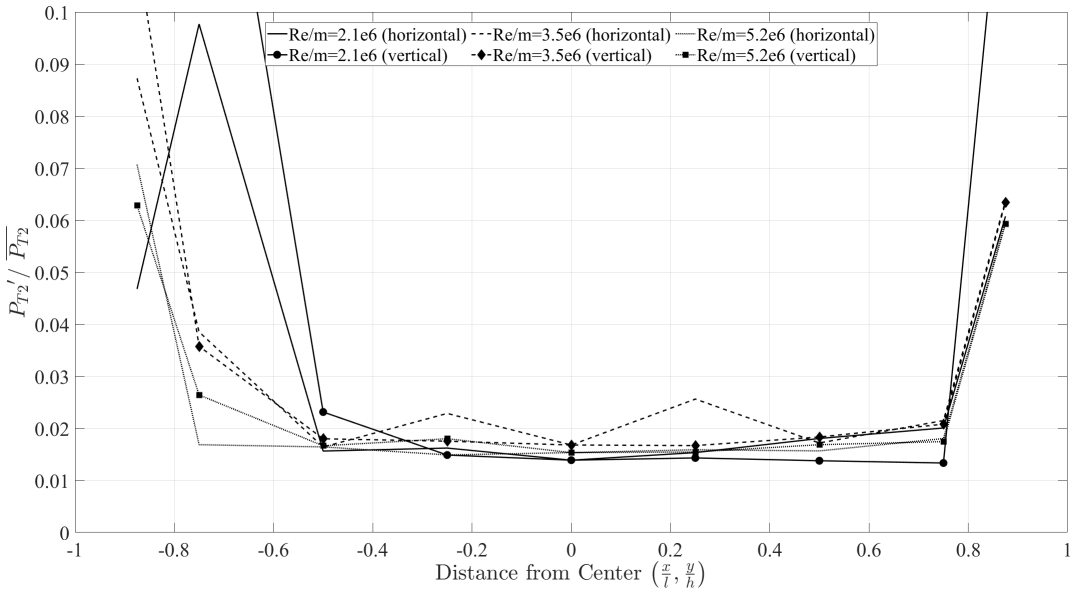

Figure 6.2: Total pressure traverse fluctuation measurements for three Reynolds conditions in horizontal and vertical directions

The pressure and temperature data taken during each tunnel run was used in conjunction with isentropic and shock-jump relations to determine the expected bulk conditions for velocity and temperature in the Mach stem flow. These values and their uncertainties are listed in table 6.2.

M_1	$T_1(K)$	$T_2(K)$	$U_1(m/s)$	$U_2(m/s)$
4.4 ± 0.1	77 ± 3	361 ± 13	773 ± 23	162 ± 5

Table 6.2: Expected Mach stem conditions.

Data from the statically mounted pitot probe runs were processed to determine the turbulent time and length scales for each Reynolds condition (table 6.3). The integral length scale is found to range 6.1-6.4 mm, decreasing with increasing Reynolds number, and the Taylor micro-length scale is found to range 3.4-4.8 mm, increasing with increasing Reynolds number. Due to the data collection methods, these length scales are only approximations. The sampling frequency was 300 kHz, low-pass filtered at 50 kHz, which gives a coarse auto-correlation function.

Reynolds number $(10^6/m)$	$T(\mu s)$	$\Lambda(mm)$	$t_\lambda(\mu s)$	$\lambda(mm)$
2.1	8.1	6.4	4.2	3.4
3.5	7.9	6.3	5.7	4.5
5.2	7.6	6.1	6.0	4.8

Table 6.3: Integral and Taylor time and length scales.

6.2 Flow Visualization

Schlieren flow visualization was used in this study to verify the optimal wedge spacing, as well as Mach stem formation, location, and stability in time. The final wedge design was found to have optimal spacing at 5.1 cm (2 in) separation, measured from the outside edge of the models. Several Schlieren studies were performed, and the Mach stem was found to consistently form at this wedge separation and remain in place for the duration of supersonic flow. The method for determining stability involved taking flow images over multiple tunnel runs, and it was determined that the movement of the shock location between images was within the shot-to-shot uncertainty of the tunnel conditions.

In addition to the Schlieren campaign, standard PLIF images were also taken of the Mach stem for each Reynolds condition. Example single shot images are shown in fig. 6.3. The slip lines between the subsonic region downstream of the normal shock and the supersonic region downstream of the reflected shock show signs of transition to turbulence. It appears that as the freestream Reynolds number is increased this transition is pushed farther upstream.

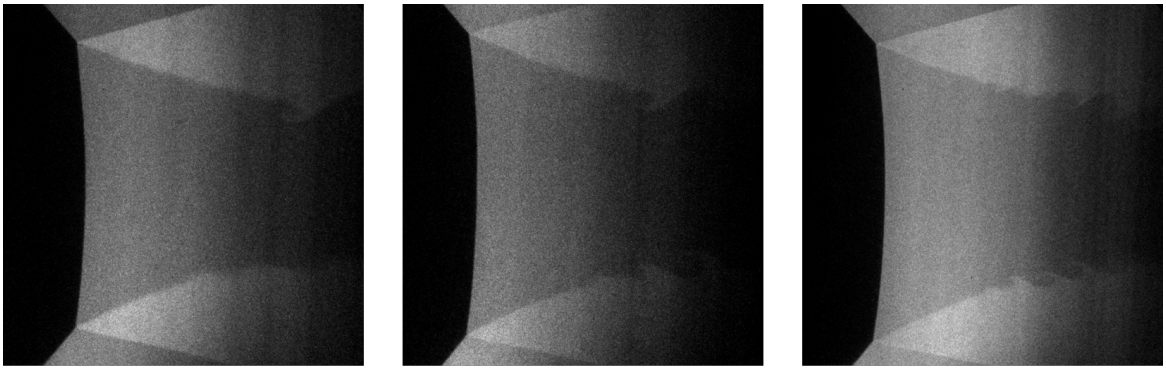

(a) Re/m=2.1e6 (b) Re/m=3.5e6 (c) Re/m=5.1e6

Figure 6.3: PLIF images of Mach stem flow for each Reynolds condition.

Additionally, the local pressure gradient downstream of the shock was estimated by measuring the average change in area of this region within the PLIF images. Because the flow is subsonic in this region, the area change can be related to the pressure gradient through the conservation of mass and momentum: $\frac{dA}{dx} = \frac{dP}{dx}\frac{A}{\rho U^2}(1 - M^2)$. The pressure gradients were determined to range -303 kPa/m to -366 kPa/m, increasing with increasing Reynolds number.

6.3 MTV Across Normal Shock

MTV experiments were performed on the Mach stem flow at four locations downstream of the normal shock wave for each Reynolds condition. The measurement locations were determined in post processing and were found to inhabit the region within 0.1 to 0.4 mm downstream of the normal shock wave. The freestream measurements were taken at a distance 1.6 to 2.0 mm upstream of the shock wave. Further, the center 300 pixels were extracted for analysis to avoid potential interactions with the shear layer. This final interrogation window is shown in fig. 6.4, overlaid on a PLIF image of the Mach stem at Re/m = 5.2e6 for visual reference.

The mean and fluctuating velocities within the measurement domain for Re/m=2.1e6 are shown in fig. 6.5 below. The mean velocity at this condition was found to be 775-780 m/s in the freestream and 155-165 m/s downstream of the normal shock. The velocity fluctuations range from 1-1.5 % in the freestream to 5-6 % downstream of the normal shock.

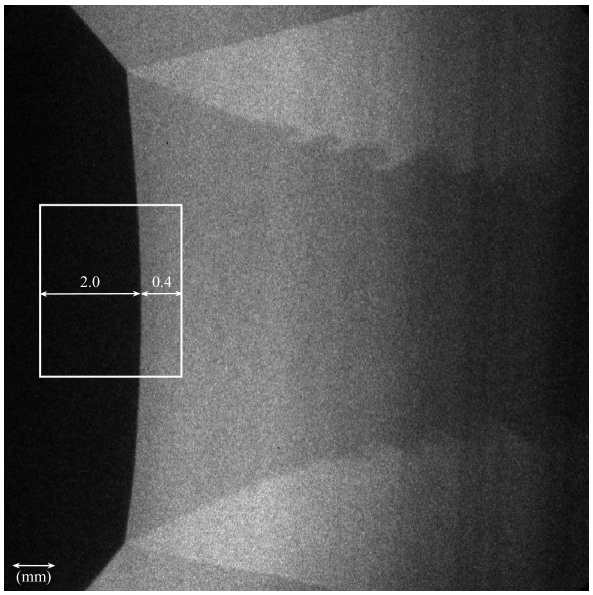

Figure 6.4: MTV measurement domain overlaid on PLIF image of Mach stem at Re/m = 5.2e6.

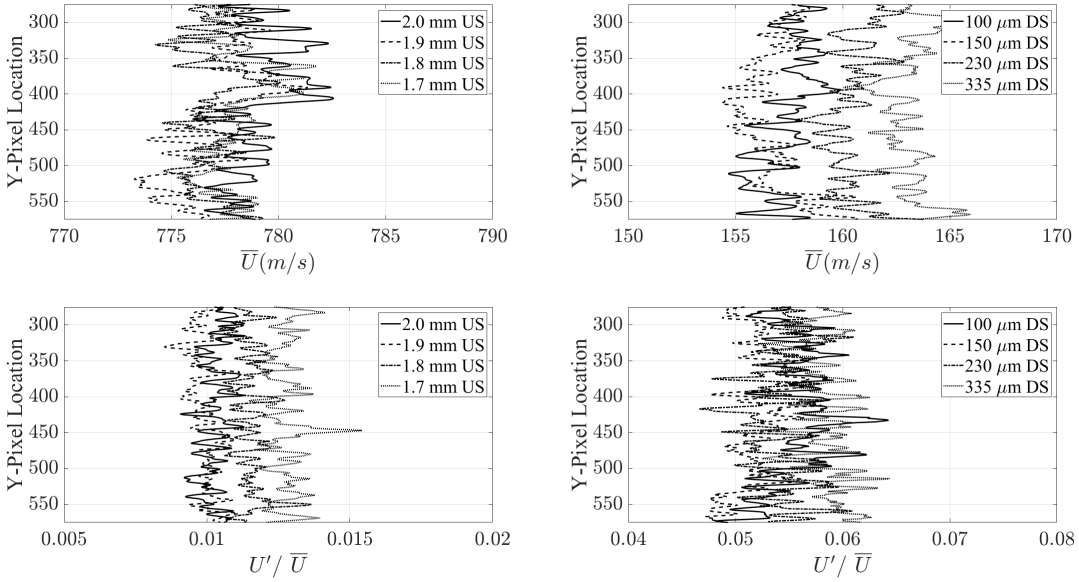

Figure 6.5: Mean and fluctuating velocities across shock for Re/m=2.1e6.

Figure 6.6 shows the number of data points (or image pairs) that were above the uncertainty cutoff of $r^2 = 0.95$ across the measurement domain for each measurement location of the Re/m =2.1e6 condition. In the freestream, 98-100 % of data points are retained using this cutoff. Down-

stream of the shock wave there is an increase in the number of data points that are cutoff. The closest and farthest locations from the shock wave in the downstream case show the highest loss of data, at 85-95 % retention; while the two intermediate locations retain at least 95 % of points. The discrepancy of the first location is possibly due to the proximity of the shock wave. In post processing, the shock wave was found to alter the line shape at this first location in some of the image pairs (due to shot-to-shot inconsistency in shock formation). These images were excluded from further processing, however it is possible that some inconsistency at this proximity was carried through in the remaining images as well. The low retention of the final location is presumably due to a discrepancy of laser intensity compared to the other cases.

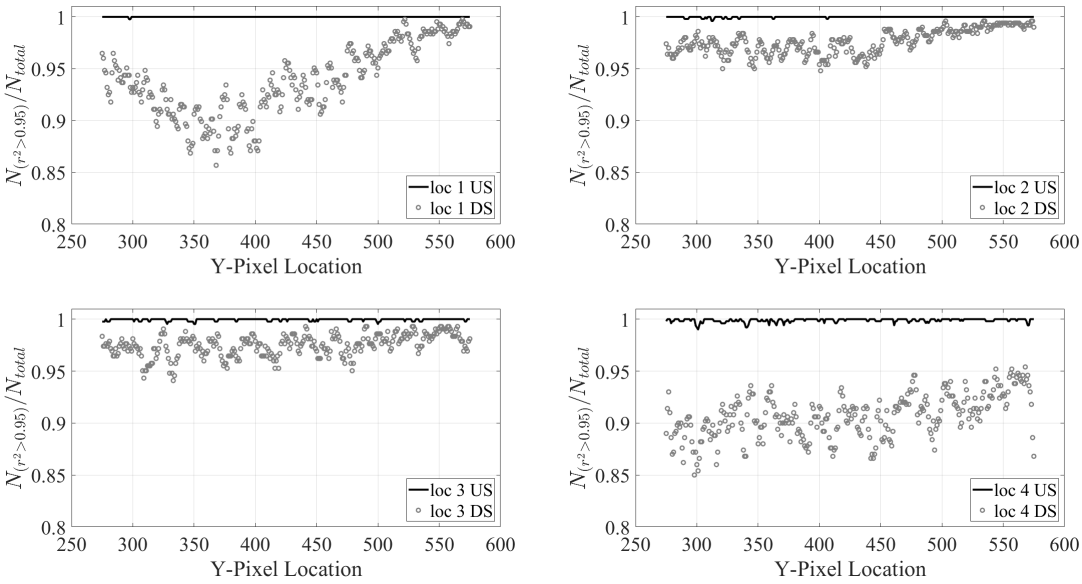

Figure 6.6: Number of points above uncertainty cutoff for Re/m=2.1e6. From top left to bottom right are the four measurement locations upstream and downstream of the shock, starting at the closest location downstream and increasing distance.

The velocity amplification factor is defined as the square of downstream fluctuations divided by upstream fluctuations, $G = (U_{DS}')^2 / (U_{FS}')^2$, in this work. Amplification factor is plotted against distance downstream of the shock at each point in fig. 6.7. All four measurement locations are included, and the mean value for each location is shown in black over the raw data. The larger

scatter observed closer to the shock is likely due again to the shock proximity and decrease in data retention. Moving farther downstream the amplfication factor is found to trend towards unity with a spread of ± 0.2.

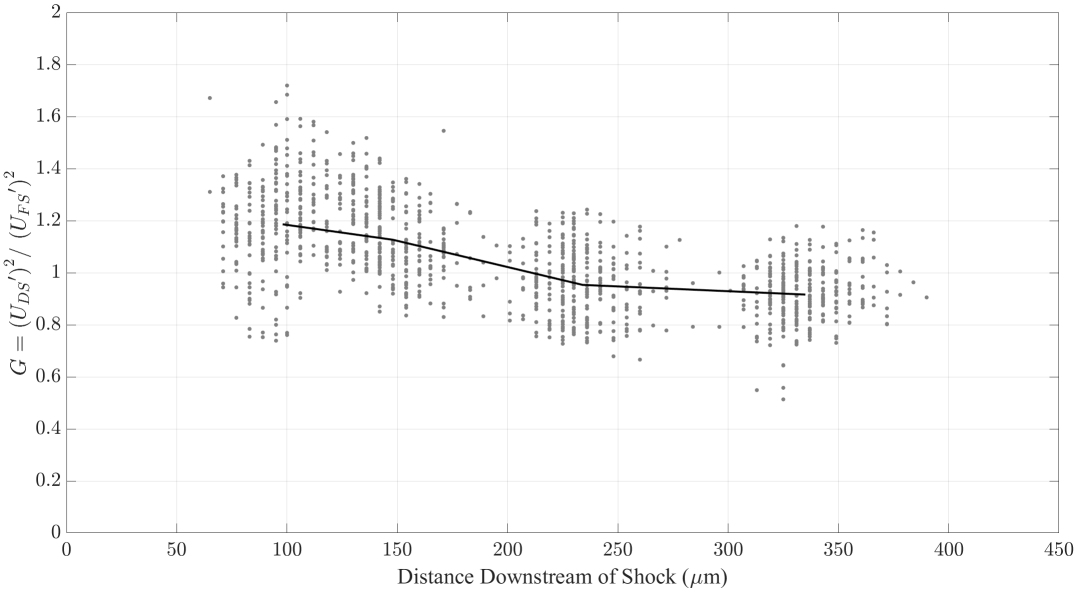

Figure 6.7: Velocity amplification factor as a function of distance downstream of shock for Re/m=2.1e6.

The mean and fluctuating velocities within the measurement domain for Re/m=3.5e6 are shown in fig. 6.8. The mean velocity at this condition was found to be 785-790 m/s in the freestream and 155-165 m/s downstream of the normal shock. The velocity fluctuations range from 0.7-0.8 % in the freestream to 3.5-4.5 % downstream of the normal shock.

Figure 6.9 shows the number of data points (or image pairs) that were above the uncertainty cutoff of $r^2 = 0.95$ across the measurement domain for each measurement location of the Re/m =3.5e6 condition. At this condition, there is virtually no data cutoff in any freestream or downstream locations.

Velocity amplification factor for Re/m=3.5e6 is shown in fig. 6.10. The amplificcation factor for this condition was found to be consistent across the measurement domain, with a mean value

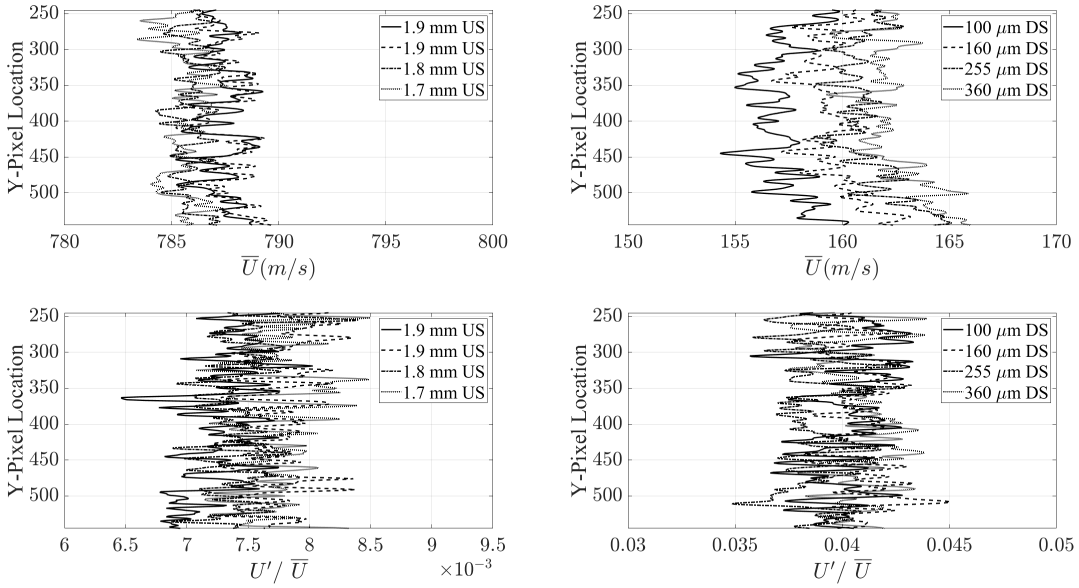

Figure 6.8: Mean and fluctuating velocities across shock for Re/m=3.5e6.

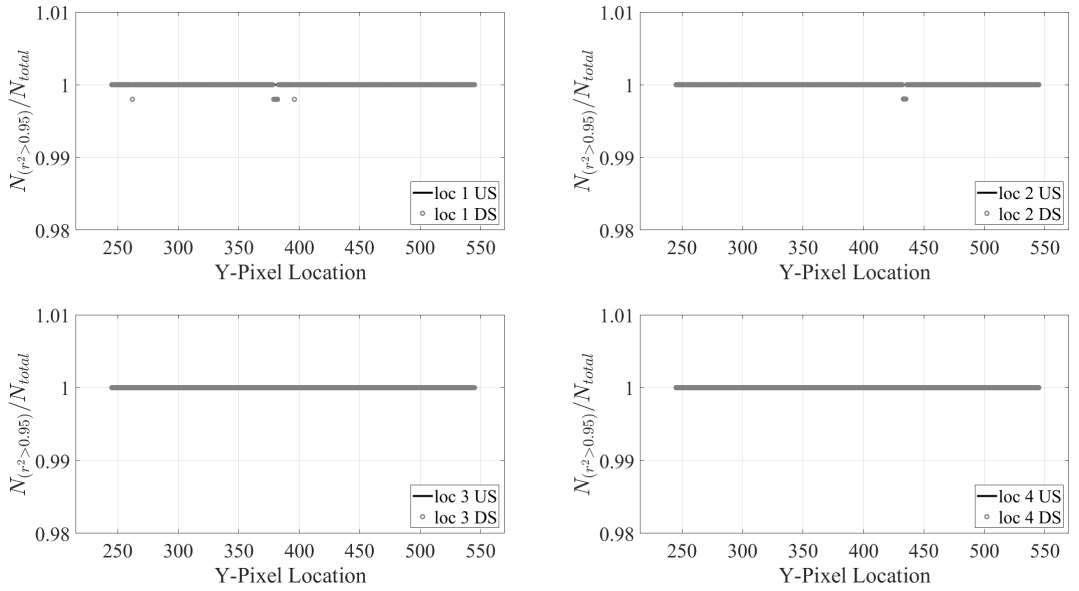

Figure 6.9: Number of points above uncertainty cutoff for Re/m=3.5e6. From top left to bottom right are the four measurement locations upstream and downstream of the shock, starting at the closest location downstream and increasing distance.

of 1.2 and a spread of ± 0.2.

The mean and fluctuating velocities within the measurement domain for Re/m=5.2e6 are shown

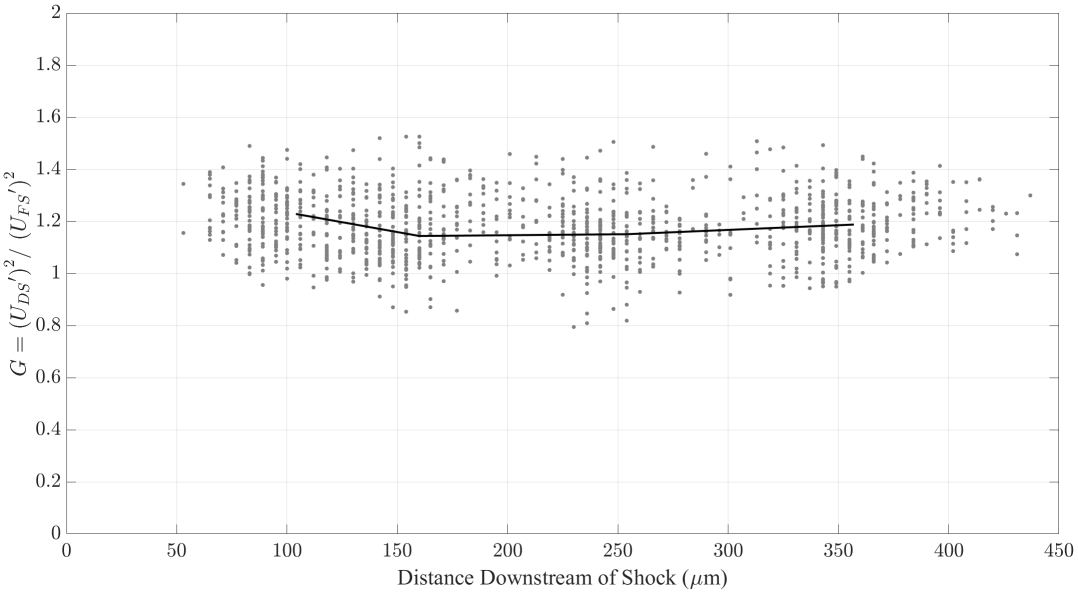

Figure 6.10: Velocity amplification factor as a function of distance downstream of shock for Re/m=3.5e6.

in fig. 6.11 below. The mean velocity at this condition was found to be 763-767 m/s in the freestream and 163-173 m/s downstream of the normal shock. The velocity fluctuations range from 0.65-0.8 % in the freestream to 3-4 % downstream of the normal shock.

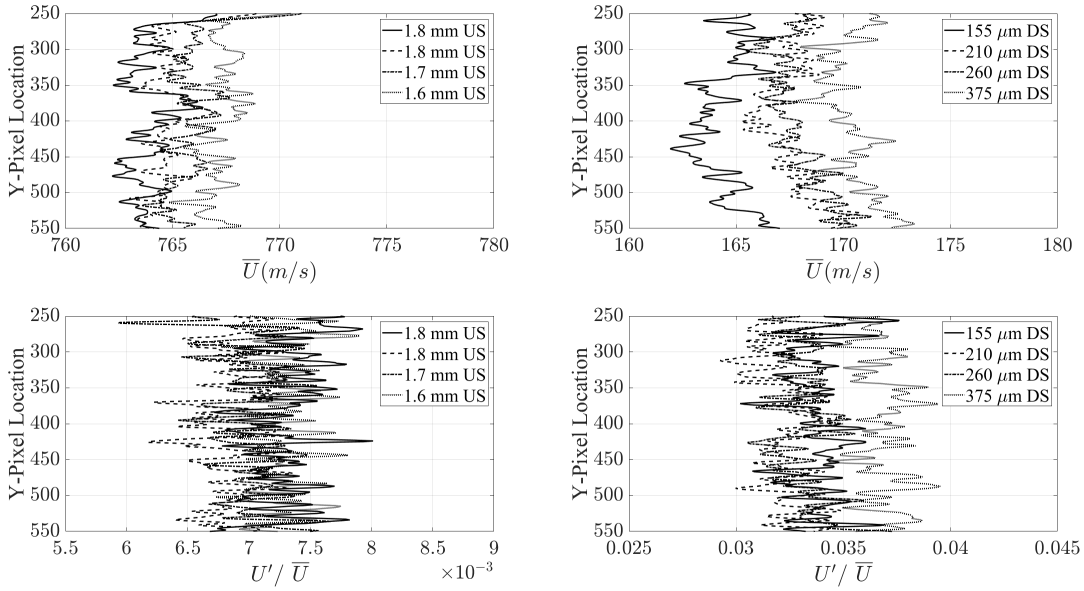

Figure 6.11: Mean and fluctuating velocities across shock for Re/m=5.2e6.

Figure 6.12 shows the number of data points (or image pairs) that were above the uncertainty cutoff of $r^2 = 0.95$ across the measurement domain for each measurement location of the Re/m =5.2e6 condition. The majority of data points are retained at this Reynolds condition, with at least 98 % retention across most of the measurement domain.

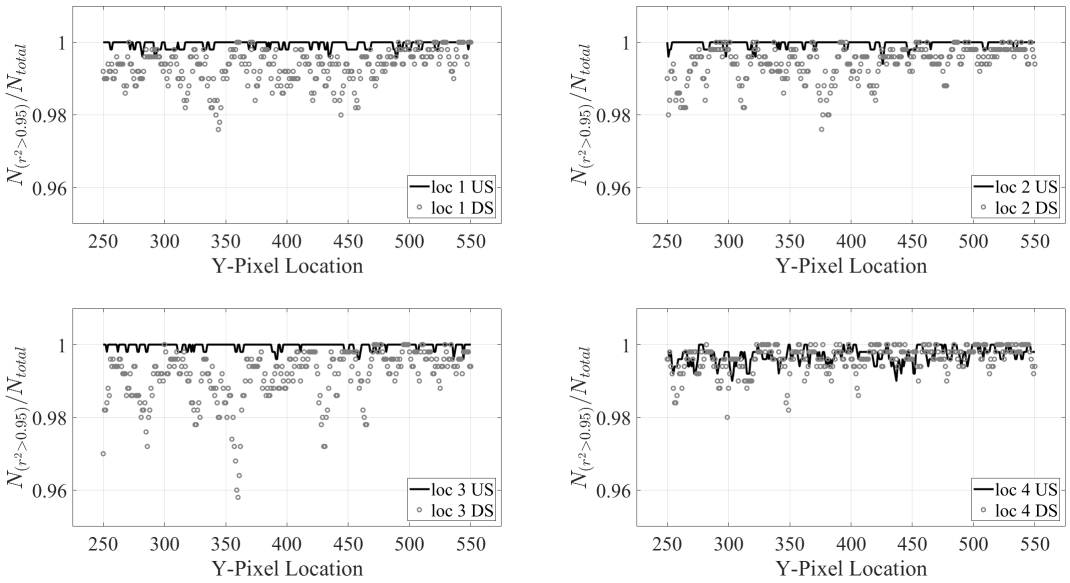

Figure 6.12: Number of points above uncertainty cutoff for Re/m=5.2e6. From top left to bottom right are the four measurement locations upstream and downstream of the shock, starting at the closest location downstream and increasing distance.

Figure 6.13 shows the velocity amplification factor for the Re/m = 5.2e6 condition. The mean amplification is found to be just above unity, with a spread of $\pm$ 0.2. A slight increase in amplification is noted moving farther downstream of the shock wave, though overall, no significant trend is observed.

The mean velocities discussed above for the three Reynolds conditions were time-averaged over 500 samples. Figure 6.14 shows 10 randomly selected velocity profiles in comparison with the mean velocity for a single line location in the middle Reynolds condition. This better shows the overall spread of the data, and the result of the 500 sample averaging.

In fig. 6.15 below, the mean velocities for each Reynolds condition are compiled. Each data

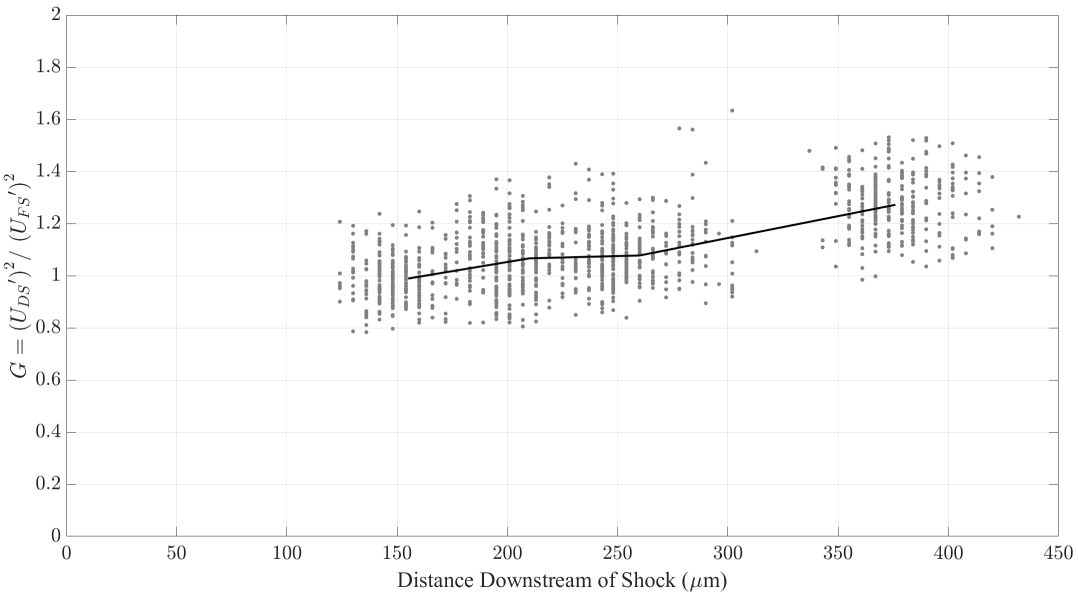

Figure 6.13: Velocity amplification factor as a function of distance downstream of shock for Re/m=5.2e6.

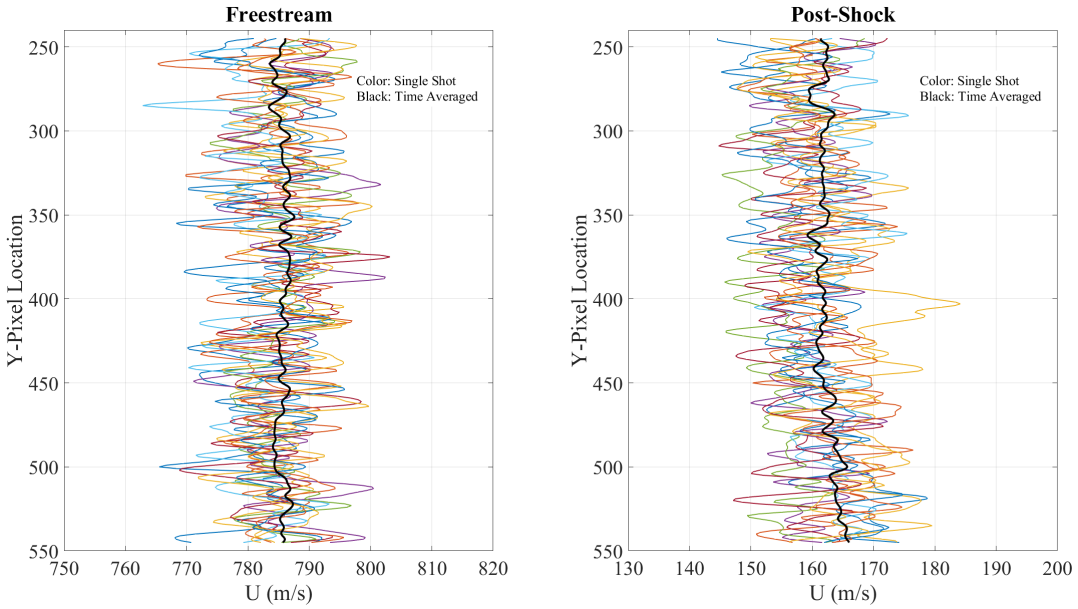

Figure 6.14: Several single-shot velocity profiles (color) in comparison to the time-averaged mean velocity (black).

point is an average along the vertical direction with error bars representing one standard deviation.

The mean velocities are found to be within the uncertainty of the expected conditions. The un-

certainty in cross-correlation peak estimation is believed to be on the order of 0.1 pixels following secondary fitting procedures, which does not account for the 3 % difference in mean velocities observed. It is believed the main source of variability in velocity determination arises from the uncertainty of actual tunnel conditions during typical operation.

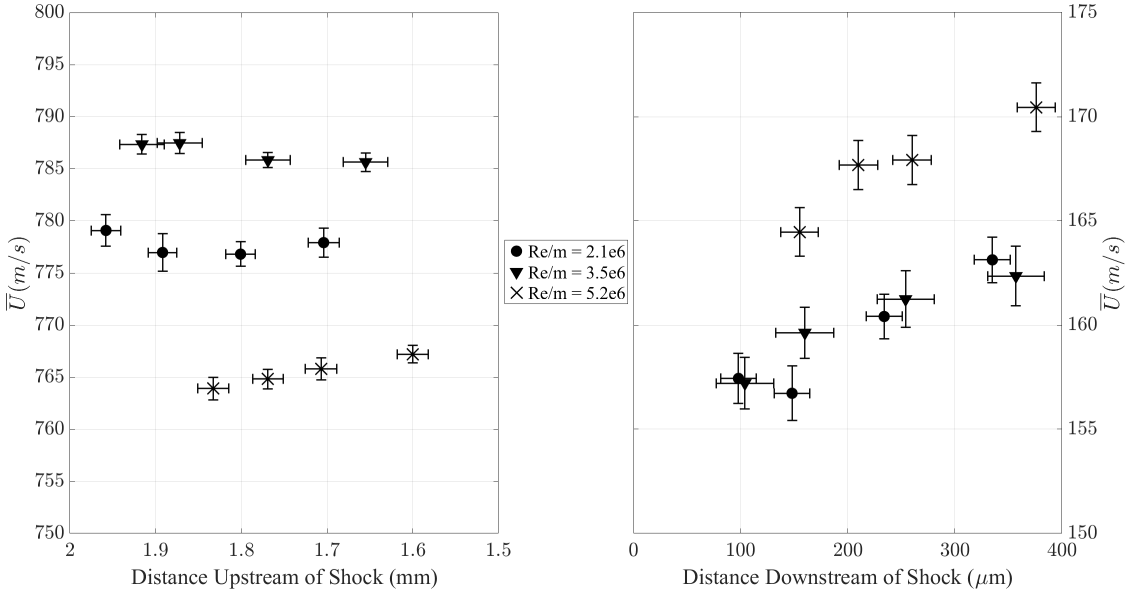

Figure 6.15: Mean velocity across shock for all Reynolds conditions.

The rms fluctuating velocities are compiled in fig. 6.16, where again, error bars represent one standard deviation. Higher freestream and post-shock fluctuations are noted in the lowest Reynolds condition, opposed to expectation. This trend is consistent with the freestream measurements performed without model wedges installed (see Appendix A), thus it is believed that the operation of the facility at such a low pressure leads to an increase in freestream disturbances, possibly due to mass flow inconsistencies through the control valves at this condition.

Average amplification factors of the three Reynolds conditions are plotted together in fig. 6.17. There does not appear to be a significant Reynolds number trend in velocity amplification for these conditions. The low Reynolds condition is perhaps an anomaly, due to discrepancies described previously. The final two conditions lie in close proximity to each other, with perhaps a slight

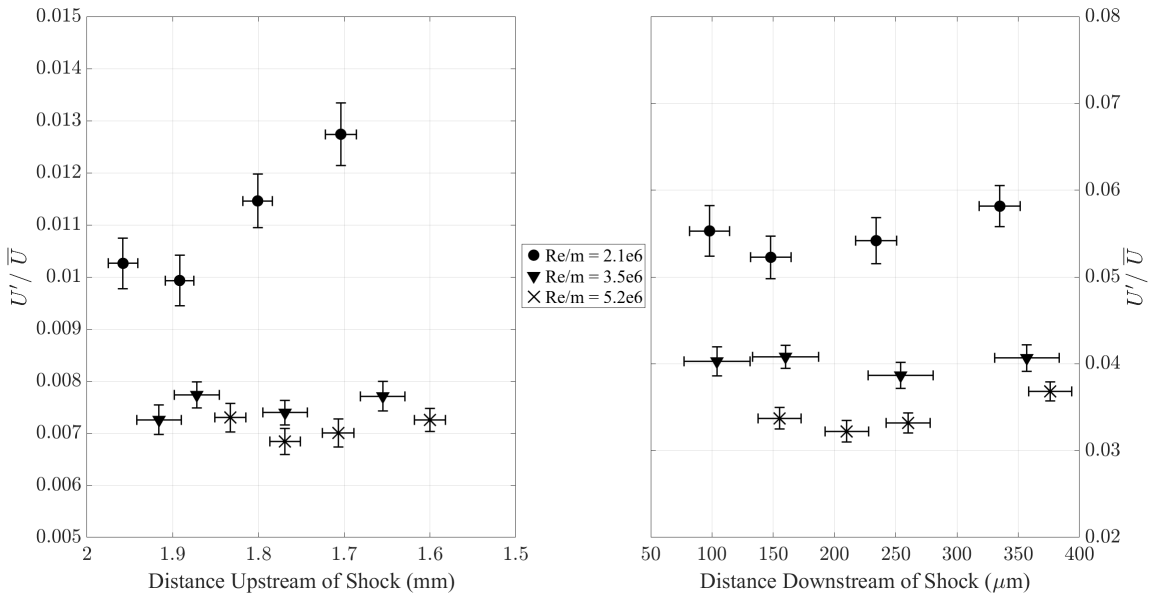

Figure 6.16: Velocity RMS across shock for all Reynolds conditions.

reduction in amplification with increasing Reynolds number.

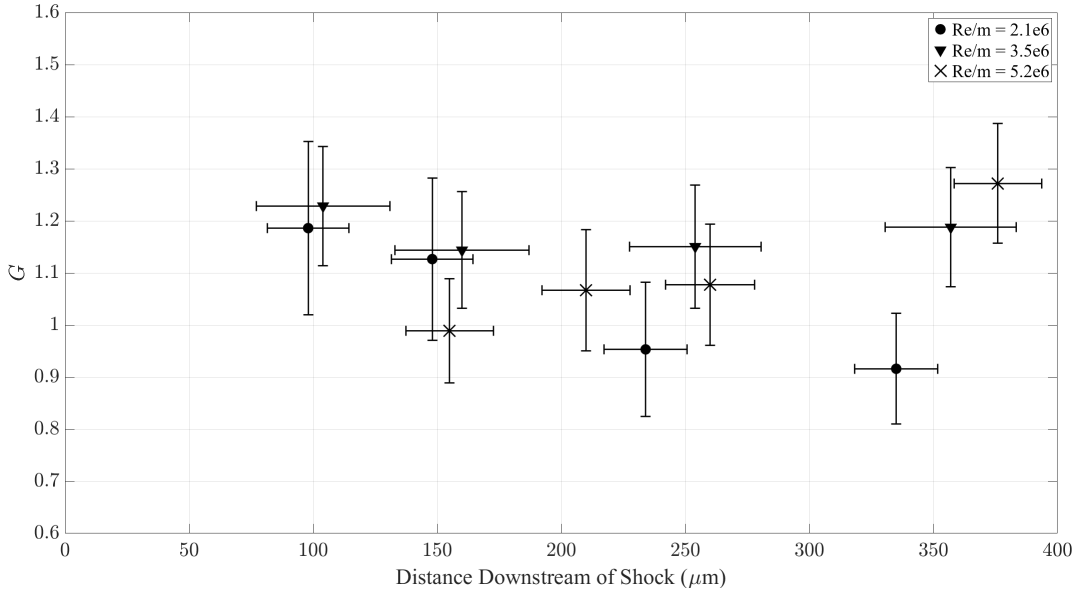

Figure 6.17: Velocity amplification factors across shock for all Reynolds conditions.

Finally, the velocity amplification factors from this work are shown in relation to the LIA plot

from [1] in fig. 6.18. The mean values fall just below the LIA curve, with no distinct Reynolds number trend. Error bars representing the spread of the data in this study are found to just reach the LIA prediction. In contrast, the other works included in Donzis' study around this Mach number all lie well above the LIA prediction line.

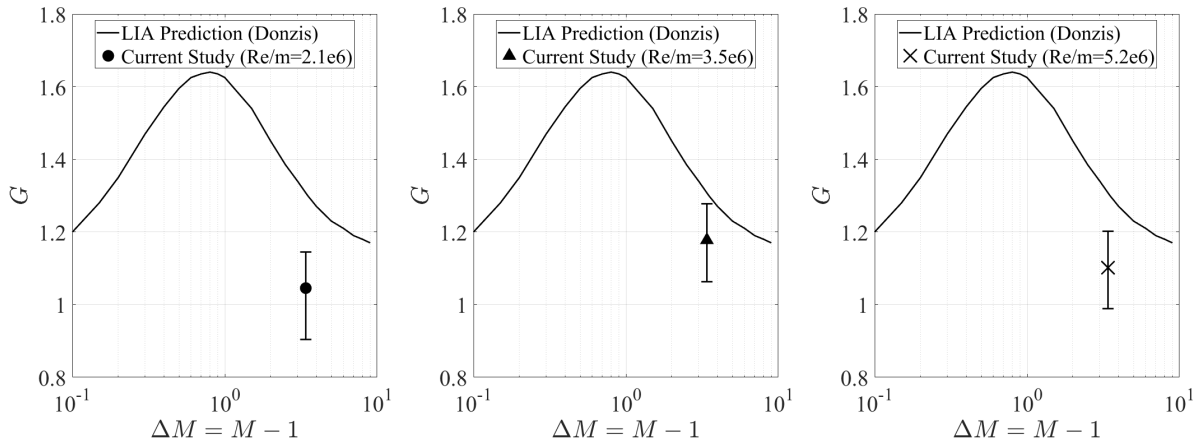

Figure 6.18: Velocity amplification factors in relation to LIA predictions (adapted from Donzis [1]).

6.4 Thermometry Across Normal Shock

As previously discussed, the PLIF thermometry experiments were found to be outside of the linear regime. The mean temperature was specified for two defined regions in front and behind the shock wave, based on the expected conditions determined previously. Each region was processed using averaged 4x4 pixel bins, and temperature outliers beyond three standard deviations from the mean were excluded. Using these techniques, there was at least 98 % retention of data points (image pairs) across the domain for all three Reynolds conditions. Contour plots of the fluctuating temperatures for each Reynolds condition are shown in fig. 6.19. The two analysis regions are overlaid on the average PLIF image for each case for visual representation.

In thermometry processing, laser intensity fluctuations play into the systematic error of the results. It could be suggested that the observed fluctuations are truly a result of laser intensity and

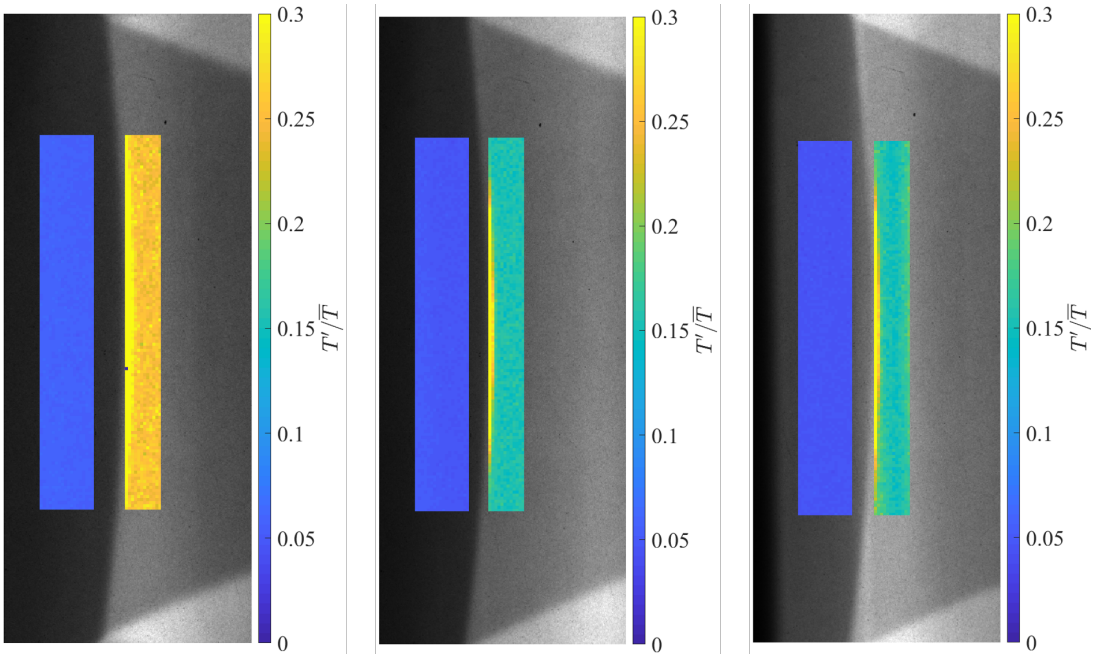

Figure 6.19: Temperature RMS fluctuations across shock for three Reynolds conditions. Left: Re/m =2.1e6, Center: Re/m = 3.5e6, Right: Re/m = 5.2e6.

not turbulent properties. Figure 6.20 below shows the evolution of temperature fluctuations at 10 randomly selected pixels in each of the pre- and post shock domains for the highest Reynolds condition. The scale is set to view only the first 200 image pairs to better visualize the correlation. It is expected that dominating laser intensity fluctuations would lead to correlated behavior between all of the pixels, where true temperature fluctuations would be represented by 10 randomly fluctuating lines. While there are some common peaks, it can be seen that the 10 pixels act independently, therefore, it is believed that the systematic error did not dominate these measurements.

Line plots representing the average temperature fluctuation across the vertical direction are shown in fig. 6.21. Again, similar to the velocity results, the lowest Reynolds condition is found to have increased fluctuations in both the freestream and post-shock regions, while the remaining Reynolds conditions lie in close proximity to each other. Freestream fluctuations range 4.5-6 %, increasing to 15-25 % in the region downstream of the shock wave.

Due to the significant temperature fluctuations observed downstream of the shock wave, the temperature amplification factor is defined in reference to the normalized fluctuations in this work.

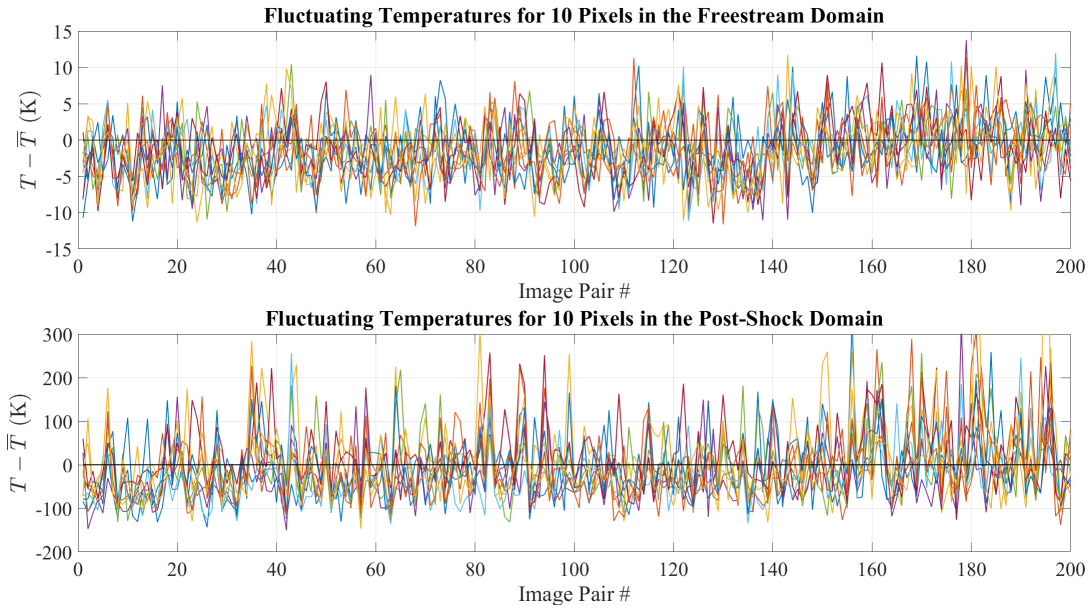

Figure 6.20: Temperature fluctuation evolution for the first 200 image pairs of 10 randomly selected pixels in the pre- and post-shock domains.

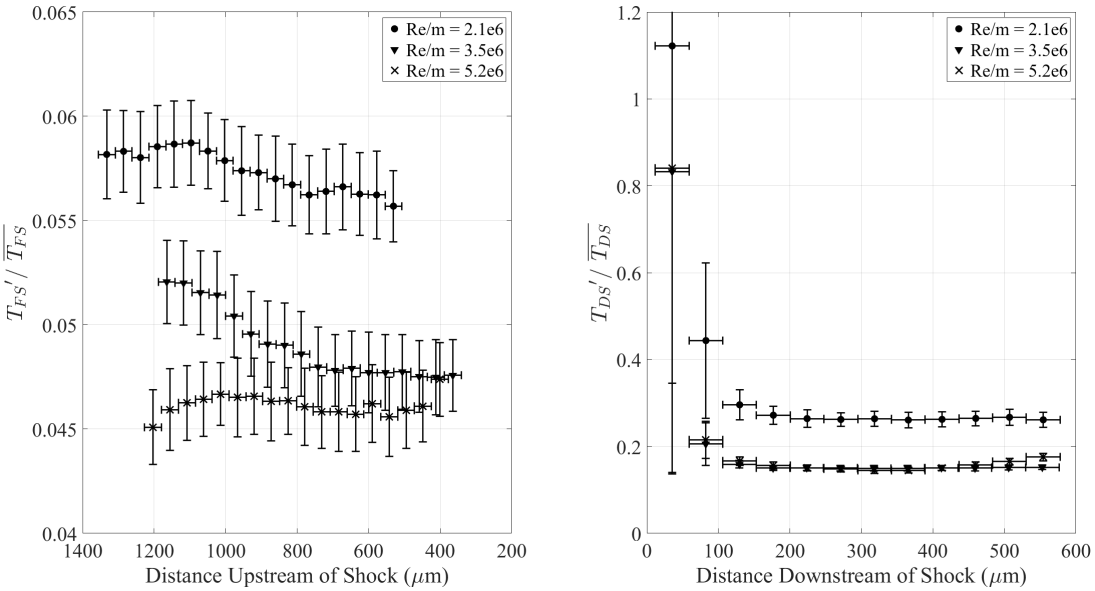

Figure 6.21: Average temperature RMS fluctuations as a function of distance downstream of shock for three Reynolds conditions.

Specifically, $G_T = \sqrt{\left(T_{DS}'/\overline{T_{DS}}\right)^2 / \left(T_{FS}'/\overline{T_{FS}}\right)^2}$, where the upstream and downstream fluctuations are normalized by their respective mean temperatures. Under this definition, the lowest

Reynolds condition settles to an amplification factor of 4.5, while the middle and high Reynolds conditions converge around 3. Moving towards the shock wave, the temperature amplification increases dramatically in all three cases. It is not truly possible to measure temperature fluctuations within the shock in this study, due to the time delay between images and uncertainty in specific shock location. Thus, the peak amplification is rather uncertain. In fact, due to pixel binning effects, only the region beyond 100 μm should be considered, and the region closer to the shock can only be a rough approximation.

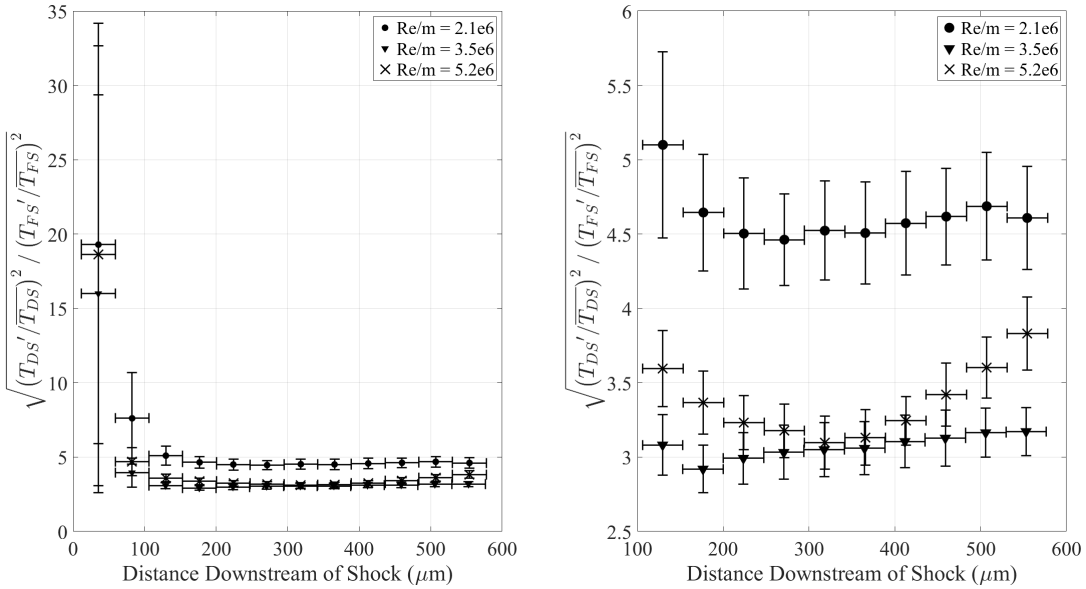

Figure 6.22: Average temperature amplification factor as a function of distance downstream of shock for three Reynolds conditions. To the left, the entire domain is included, to the right, only the region downstream of 100 μm is shown.

6.5 Uncertainty Analysis

As with any experiment, there are several expected sources of error in this work. A large concern was signal-to-noise (SNR) limitations, particularly in the low temperature and low density freestream. To mitigate this, the camera was liquid cooled to -35 C, which reduces the charge buildup on the sensor. Additionally, the dark-charge was subtracted within the camera software,

which brought the base noise level down to approximately 60 counts. The lowest signal applications in this study experienced approximately 600 counts, thus, the SNR was found to be 10 or higher. Another source of error in the MTV application arises from the timing jitter of the system (pulse/delay generator, camera, and lasers). The maximum reported timing jitter from each of these components arises from the YAG laser, at <0.5 ns, and the expected uncertainty from the system is <0.06 %. The uncertainty of the MTV data processing algorithm was 0.1 pixels (as discussed in section 5.2.3), which in the low velocity region downstream of the shock results in an uncertainty of 0.4 %. The random error was reduced by taking large sample data sets. The total number of data points was of the order 600 thousand samples, and the expected error is <0.2 %. Thus, the total error in the MTV application is expected to be of the order 0.5 %.

The thermometry application experienced similar sources of error, including SNR, data processing, and laser intensity fluctuations. Due to the pixel binning routine, the random error for thermometry is expected to increase to 0.25 %. There was a reported 4 % uncertainty in the mean temperature estimate, however, once established it is believed that this does not translate directly to the uncertainty in determination of the fluctuating temperatures. Overall, the total uncertainty from systematic and random sources is expected to be less than 0.5 %.

The time delay between images was set to be 1.7 μs in these experiments. This was selected to reduce the uncertainty in velocity determination by increasing the movement of the lines between images. From the freestream velocity measurements, the molecules are known to travel less than 1.5 mm. The Taylor microscale was estimated to be 3-4 mm, thus it is believed that there was no significant loss of turbulence information due to the extended time delay.

7. CONCLUSIONS AND RECOMMENDATIONS

The goal of this study was to observe velocity and temperature fluctuation behavior through a stationary normal shock wave at Mach 4.4. This Mach number was selected for observation due to the high discrepancy between current theoretical and computational works, as well as the lack of experimental data in this regime. Three conditions were studied, listed in table 7.1. Experiments were performed in a small scale pulsed operation wind tunnel facility with Mach stem generator models installed to produce a normal shock wave in the freestream. No turbulence generating apparatus was used, rather the freestream fluctuations were a product of typical tunnel operation. This would include the incident noise due to flow through the tunnel supply lines and through the inlet valve orifices, as well as acoustic waves originating from the nozzle wall boundary layers. The major findings of this work are discussed below, followed with recommendations for future works.

Reynolds number $(10^6/m)$	M	M_t	Re_λ	G	$G_T{}^\dagger$	$K^\ddagger$ (10^{-3})
2.1	4.41	0.083	79	1.05	4.5	2.8
3.5	4.42	0.057	124	1.18	3.05	1.5
5.2	4.41	0.052	174	1.10	3.1	1.2

Table 7.1: List of cases observed in this work in terms of turbulent Mach and Reynolds conditions and the observed amplification factors. $^\dagger G_T$ is defined in section 6.4 as the square root of the ratio of normalized fluctuations.$^\ddagger K$ is the similarity parameter defined and adapted from [1].

7.1 Concluding Remarks

Several optical techniques were employed in this work to observe amplification of vortical and entropic turbulence modes. Single component velocity measurements were taken at four locations downstream of the Mach stem for each Reynolds condition. This was followed by a PLIF thermometry investigation across the same region of interest for each case. Of the three conditions

studied, the lowest Reynolds case seems to be an anomaly, having increased levels of freestream disturbances in both velocity and temperature. This is thought to be due to tunnel operation at low pressure. The behavior is observed during all experiments, with and without model wedges installed, so it is unlikely to be an experimental error.

Freestream velocity fluctuations for the axial mode were measured to be 0.7-1.2 %, normalized by the mean velocity. In the post shock region, the RMS fluctuations were found to increase to 3-6 %, normalized by the respective post-shock mean velocity. Transverse velocity fluctuations were not obtained in this study, therefore the role of the transverse modes in this STI investigation are not indicated. Amplification of the axial mode was found to be 1.1-1.2, with no strong Reynolds number effect. The freestream velocity fluctuations are relatively weak compared to the other modes in this study (1.8-1.9 % total pressure fluctuations and 4.5-6 % temperature fluctuations), therefore it is difficult to separate its role in the observed amplification.

The measured velocity amplification factor is in near agreement with LIA prediction, though significantly lower than the computational studies in a similar Mach and K regime (see [53]). The absence of transverse velocity components may play a role in this discrepancy, though it should be noted that this is not truly a direct comparison. Many theoretical and computational studies report amplification factor as the ratio of fluctuating velocities that are computed at the shock boundary (or often some defined peak location), where these measurements were made approximately 200 μm downstream of the shock wave. It is believed another source of discrepancy may arise from the presence of temperature fluctuations. It has been shown that the presence of entropy fluctuations is influential to the correlation of U' and T' for strong shocks and high Mach numbers [73]. Additionally, the behavior of this correlation may have a suppressing affect on amplification of thermodynamic properties in STI [47]. It is indicated in this work that the presence of strong entropy fluctuations may be providing a suppression affect toward the amplification of axial velocity fluctuations. In fact, with increased freestream disturbances in the lowest Reynolds number case, the amplification factor of velocity is found to decrease.

Temperature fluctuations were measured to be 4.5-6 % in the freestream and 15-25 % in the

post-shock region. The Re/m = 2.1e6 condition had significantly higher fluctuations than the Re/m = 3.5e6 and 5.2e6 cases. The region downstream of the shock was defined starting at the shock boundary, and was binned in 4x4 pixel intervals. The time delay between image pairs was 1.7 μs, to remain consistent with previous MTV measurements. These factors led to significant uncertainty in temperature fluctuation measurements near the shock boundary. Amplification factors were reported to be 3-4.5 for the region beyond 100 μm downstream of the shock, where the amplification factor in this case is defined for the normalized fluctuating temperatures. It is noted that the case with significantly increased turbulent Mach number reports the highest temperature fluctuation amplification. The other two cases show similarity in both turbulent Mach number and amplification factor. This would indicate that increased turbulent Mach number may lead to increased temperature fluctuation amplification. In fact, a power law fit to this data shows a trend of $M_t^{1.5}$, however the small sample of only three data points makes this relationship rather uncertain.

7.2 Recommendations

The work presented provides a preliminary database of vortical and entropic fluctuation amplification in high Mach number shock-turbulence interactions. The selected high Mach number and non-intrusive measurement techniques allowed for novel measurements that provide new insight where classical and contemporary theories do not yet agree, however, these observations do not fully close the knowledge gap in this regime of STI. Some opportunities for further investigation are listed:

- High-fidelity investigation of the acoustic mode in addition to the velocity/entropy mode would lead to a deeper understanding of the potential pressure coupling and its overall role in STI. Further, investigation of pressure fluctuations using a non-intrusive method would be ideal, as the advantages of optical techniques for STI have been shown in this work.
- Investigation of the velocity-temperature correlation in STI is severely limited. The dominating entropy mode in this work indicated the importance of this correlation, as some previous works have suggested ([73] & [47]), however a full investigation was not possible. It is known that typical wind tunnel environments will experience freestream disturbances

of all three Kovazsnay modes, and it is expected that atmospheric conditions will be similar due to the presence of thermal gradients and gravitational/Coriolis effects, thus it is imperative to continue the exploration of this behavior. Simultaneous optical approaches exist for measuring temperature and velocity in turbulent fields, and experiments of this nature would broaden STI knowledge.

REFERENCES

[1] D. A. Donzis, "Amplification factors in shock-turbulence interactions: Effect of shock thickness," *Physics of Fluids*, vol. 24, no. 1, p. 011705, 2012.

[2] J. Larsson, I. Bermejo-Moreno, and S. K. Lele, "Reynolds-and Mach-number effects in canonical shock–turbulence interaction," *Journal of Fluid Mechanics*, vol. 717, pp. 293–321, 2013.

[3] H. S. Ribner, "Convection of a pattern of vorticity through a shock wave," tech. rep., NACA NACA, 1954.

[4] H. S. Ribner, "Shock-turbulence interaction and the generation of noise," tech. rep., National Aeronautics and Space Administration, Cleveland Oh Lewis Research Center, 1955.

[5] D. A. Donzis and S. Jagannathan, "On the relation between small-scale intermittency and shocks in turbulent flows," *Procedia IUTAM*, vol. 9, pp. 3–15, 2013.

[6] L. S. G. Kovasznay, "Turbulence in supersonic flow," *Journal of the Aeronautical Sciences*, vol. 20, no. 10, pp. 657–674, 1953.

[7] R. Quadros, K. Sinha, and J. Larsson, "Turbulent energy flux generated by shock/homogeneous-turbulence interaction," *Journal of Fluid Mechanics*, vol. 796, pp. 113–157, 2016.

[8] J. D. Anderson, *Modern compressible flow, with historical perspective*, ch. 3,4. McGraw-Hill, second edition ed., 1990.

[9] J. D. Anderson, *Introduction to Flight*, pp. 183–185. McGraw-Hill, sixth edition ed., 2008.

[10] D. A. Donzis, "Shock structure in shock-turbulence interactions," *Physics of Fluids*, vol. 24, no. 12, p. 126101, 2012.

[11] A. R. Staff, "Equations, tables, and charts for compressible flow," *NACA Report*, vol. 1135, 1953.

[12] S. B. Pope, *Turbulent flows*, ch. 1, 4, 6. Cambridge University Press, 2000.

[13] O. Reynolds, "IV. On the dynamical theory of incompressible viscous fluids and the determination of the criterion," *Philosophical Transactions of the Royal Society of London.(a.)*, no. 186, pp. 123–164, 1895.

[14] A. J. Favre, "The equations of compressible turbulent gases," tech. rep., Aix-marseille Univ (france) Inst De Mecanique Statistique De La Turbulence, 1965.

[15] L. F. Richardson, *Weather prediction by numerical process*. Cambridge University Press, 2007.

[16] L. S. G. Kovasznay, "The hot-wire anemometer in supersonic flow," *Journal of the Aeronautical Sciences*, vol. 17, no. 9, pp. 565–572, 1950.

[17] A. C. Eckbreth, *Laser diagnostics for combustion temperature and species*, vol. 3. CRC Press, 1996.

[18] A. Melling, "Tracer particles and seeding for particle image velocimetry," *Measurement Science and Technology*, vol. 8, no. 12, p. 1406, 1997.

[19] L. Jacquin, E. Blin, and P. Geffroy, "An experiment on free turbulence/shock wave interaction," in *Turbulent Shear Flows 8*, pp. 229–248, Springer, 1993.

[20] R. Sanchez-Gonzalez, *Advanced laser diagnostics development for the characterization of gaseous high speed flows*. Ph.D. Dissertation, Texas A&M University, College Station, 2012.

[21] G. Herzberg, *Molecular spectra and molecular structure*, vol. 1. Read Books Ltd, 2013.

[22] Y. Andreopoulos, J. H. Agui, and G. Briassulis, "Shock wave-turbulence interactions," *Annual Review of Fluid Mechanics*, vol. 32, no. 1, pp. 309–345, 2000.

[23] J. H. Agui, G. Briassulis, and Y. Andreopoulos, "Studies of interactions of a propagating shock wave with decaying grid turbulence: velocity and vorticity fields," *Journal of Fluid Mechanics*, vol. 524, pp. 143–195, 2005.

[24] H. S. Ribner, "Spectra of noise and amplified turbulence emanating from shock-turbulence interaction," *AIAA Journal*, vol. 25, no. 3, pp. 436–442, 1987.

[25] F. K. Moore, "Unsteady oblique interaction of a shock wave with a plane disturbance," tech. rep., NACA, 1953.

[26] B.-T. Chu and L. S. Kovásznay, "Non-linear interactions in a viscous heat-conducting compressible gas," *Journal of Fluid Mechanics*, vol. 3, no. 5, pp. 494–514, 1958.

[27] A. N. Sekundov, "Turbulence in a supersonic flow and its interaction with a shock wave," *Fluid Dynamics*, vol. 9, no. 2, pp. 166–172, 1974.

[28] D. Dosanjh and T. Weeks, "Interaction of starting vortex as well as karman vortex street with traveling shock wave," in *AIAA 1st Annual Meeting*, p. 425, 1964.

[29] J. C. Anyiwo and D. M. Bushnell, "Turbulence amplification in shock-wave boundary-layer interaction," *AIAA Journal*, vol. 20, no. 7, pp. 893–899, 1982.

[30] D. Rotman, "Shock wave effects on a turbulent flow," *Physics of Fluids A: Fluid Dynamics*, vol. 3, no. 7, pp. 1792–1806, 1991.

[31] S. Lee, S. K. Lele, and P. Moin, "Direct numerical simulation of isotropic turbulence interacting with a weak shock wave," *Journal of Fluid Mechanics*, vol. 251, pp. 533–562, 1993.

[32] R. Hannappel, T. Hauser, and R. Friedrich, "A comparison of ENO and TVD schemes for the computation of shock-turbulence interaction," *Journal of Computational Physics*, vol. 121, no. 1, pp. 176–184, 1995.

[33] T. A. Zang, M. Y. Hussainit, and D. M. Bushnellt, "Numerical computations of turbulence amplification in shock-wave interactions," *AIAA Journal*, vol. 22, no. 1, pp. 13–21, 1984.

[34] K. Mahesh, S. Lee, S. K. Lele, and P. Moin, "The interaction of an isotropic field of acoustic waves with a shock wave," *Journal of Fluid Mechanics*, vol. 300, pp. 383–407, 1995.

[35] S. K. Lele, "Shock-jump relations in a turbulent flow," *Physics of Fluids A: Fluid Dynamics*, vol. 4, no. 12, pp. 2900–2905, 1992.

[36] L. Jacquin, C. Cambon, and E. Blin, "Turbulence amplification by a shock wave and rapid distortion theory," *Physics of Fluids A: Fluid Dynamics*, vol. 5, no. 10, pp. 2539–2550, 1993.

[37] G. P. Zank, Y. Zhou, W. H. Matthaeus, and W. K. M. Rice, "The interaction of turbulence with shock waves: A basic model," *Physics of Fluids*, vol. 14, no. 11, pp. 3766–3774, 2002.

[38] J. G. Wouchuk, C. H. R. de Lira, and A. L. Velikovich, "Analytical linear theory for the interaction of a planar shock wave with an isotropic turbulent vorticity field," *Physical Review E*, vol. 79, no. 6, p. 066315, 2009.

[39] H. S. Ribner, "Acoustic energy flux from shock-turbulence interaction," *Journal of Fluid Mechanics*, vol. 35, no. 2, pp. 299–310, 1969.

[40] J. Ollerhead, "Some shadowgraph experiments with a cold, supersonic jet," *Wyle Laboratories, Huntsville, Ala., Res. Staff Rep. WR 66Ű44.*, 1966.

[41] S. Lee, S. K. Lele, and P. Moin, "Interaction of isotropic turbulence with shock waves: effect of shock strength," *Journal of Fluid Mechanics*, vol. 340, pp. 225–247, 1997.

[42] S. Lee, "Large eddy simulation of shock turbulence interaction," in *Annual Research Briefs, 1992*, 1993.

[43] F. Ducros, V. Ferrand, F. Nicoud, C. Weber, D. Darracq, C. Gacherieu, and T. Poinsot, "Large-eddy simulation of the shock/turbulence interaction," *Journal of Computational Physics*, vol. 152, no. 2, pp. 517–549, 1999.

[44] T. Dubois, J. A. Domaradzki, and A. Honein, "The subgrid-scale estimation model applied to large eddy simulations of compressible turbulence," *Physics of Fluids*, vol. 14, no. 5, pp. 1781–1801, 2002.

[45] E. Garnier, P. Sagaut, and M. Deville, "Large eddy simulation of shock/homogeneous turbulence interaction," *Computers & Fluids*, vol. 31, no. 2, pp. 245–268, 2002.

[46] N. Grube, E. Taylor, and P. Martin, "Numerical investigation of shock-wave/isotropic turbulence interaction," in *49th AIAA Aerospace Sciences Meeting including the New Horizons Forum and Aerospace Exposition*, p. 480, 2011.

[47] K. Mahesh, S. K. Lele, and P. Moin, "The influence of entropy fluctuations on the interaction of turbulence with a shock wave," *Journal of Fluid Mechanics*, vol. 334, pp. 353–379, 1997.

[48] S. Jamme, J.-B. Cazalbou, F. Torres, and P. Chassaing, "Direct numerical simulation of the interaction between a shock wave and various types of isotropic turbulence," *Flow, Turbulence and Combustion*, vol. 68, no. 3, pp. 227–268, 2002.

[49] J. Larsson and S. K. Lele, "Direct numerical simulation of canonical shock/turbulence interaction," *Physics of Fluids*, vol. 21, no. 12, p. 126101, 2009.

[50] I. Bermejo-Moreno, J. Larsson, and S. K. Lele, "LES of canonical shock-turbulence interaction," *Annual Research Briefs*, pp. 209–222, 2010.

[51] J. Larsson, "Effect of shock-capturing errors on turbulence statistics," *AIAA Journal*, vol. 48, no. 7, pp. 1554–1557, 2010.

[52] X. Wang and X. Zhong, "DNS of strong shock and turbulence interactions with thermochemical non-equilibrium effects," in *42nd AIAA Fluid Dynamics Conference and Exhibit*, p. 3162, 2012.

[53] C. H. Chen and D. A. Donzis, "Shock–turbulence interactions at high turbulence intensities," *Journal of Fluid Mechanics*, vol. 870, pp. 813–847, 2019.

[54] J. Ryu and D. Livescu, "Turbulence structure behind the shock in canonical shock–vortical turbulence interaction," *Journal of Fluid Mechanics*, vol. 756, 2014.

[55] N. O. Braun, D. I. Pullin, and D. I. Meiron, "Large eddy simulation investigation of the canonical shock–turbulence interaction," *Journal of Fluid Mechanics*, vol. 858, pp. 500–535, 2019.

[56] J. W. Trolier and R. E. Duffy, "Turbulence measurements in shock-induced flows," *AIAA Journal*, vol. 23, no. 8, pp. 1172–1178, 1985.

[57] J.-F. Haas and B. Sturtevant, "Interaction of weak shock waves with cylindrical and spherical gas inhomogeneities," *Journal of Fluid Mechanics*, vol. 181, pp. 41–76, 1987.

[58] L. Hesselink and B. Sturtevant, "Propagation of weak shocks through a random medium," *Journal of Fluid Mechanics*, vol. 196, pp. 513–553, 1988.

[59] A. Honkan and J. Andreopoulos, "Experiments in a shock wave/homogeneous turbulence interaction," in *21st Fluid Dynamics, Plasma Dynamics and Lasers Conference*, p. 1647, 1990.

[60] A. Honkan and J. Andreopoulos, "Rapid compression of grid-generated turbulence by a moving shock wave," *Physics of Fluids A: Fluid Dynamics*, vol. 4, no. 11, pp. 2562–2572, 1992.

[61] A. Honkan, C. B. Watkins, and J. Andreopoulos, "Experimental study of interactions of shock wave with free-stream turbulence," *Journal of Fluids Engineering*, vol. 116, no. 4, pp. 763–769, 1994.

[62] G. Briassulis and J. Andreopoulos, "High resolution measurements of isotropic turbulence interacting with shock waves," in *34th Aerospace Sciences Meeting and Exhibit*, p. 42, 1996.

[63] S. Xanthos, G. Briassulis, and Y. Andreopoulos, "Interaction of decaying freestream turbulence with a moving shock wave: pressure field," *Journal of Propulsion and Power*, vol. 18, no. 6, pp. 1289–1297, 2002.

[64] J. Keller and W. Merzkirch, "Interaction of a normal shock wave with a compressible turbulent flow," *Mineralium Deposita*, vol. 29, no. 1, pp. 241–248, 1994.

[65] L. Jacquin and P. Geffroy, "Amplification and reduction of turbulence in a heated jet/shock interaction," in *Symposium on Turbulent Shear Flows, 11 th, Grenoble, France*, 1997.

[66] S. Barre, D. Alem, and J. P. Bonnet, "Experimental study of a normal shock/homogeneous turbulence interaction," *AIAA Journal*, vol. 34, no. 5, pp. 968–974, 1996.

[67] C. L. N. Mai, *Near-Region Modification of Total Pressure Fluctuations by a Normal Shock Wave in a Low-Density Hypersonic Wind Tunnel*. Ph.D. Dissertation, Texas A&M University, College Station, 2014.

[68] M. Semper, B. Pruski, and R. Bowersox, "Freestream turbulence measurements in a continuously variable hypersonic wind tunnel," in *50th AIAA Aerospace Sciences Meeting including the New Horizons Forum and Aerospace Exposition*, p. 732, 2012.

[69] H. G. Hornung and M. L. Robinson, "Transition from regular to mach reflection of shock waves part 2. the steady-flow criterion," *Journal of Fluid Mechanics*, vol. 123, pp. 155–164, 1982.

[70] C. A. Mouton and H. G. Hornung, "Mach stem height and growth rate predictions," *AIAA Journal*, vol. 45, no. 8, pp. 1977–1987, 2007.

[71] A. Chpoun and E. Leclerc, "Experimental investigation of the influence of downstream flow conditions on Mach stem height," *Shock Waves*, vol. 9, no. 4, pp. 269–271, 1999.

[72] G. S. Settles, "Schlieren and shadowgraph techniques- visualizing phenomena in transparent media(book)," *Berlin, Germany: Springer-Verlag GmbH, 2001.*, 2001.

[73] R. Quadros, K. Sinha, and J. Larsson, "Kovasznay mode decomposition of velocity-temperature correlation in canonical shock-turbulence interaction," *Flow, Turbulence and Combustion*, vol. 97, no. 3, pp. 787–810, 2016.

APPENDIX A

FREESTREAM CHARACTERIZATION

A.1 Velocity Characterization

The baseline freestream velocity condition was determined by performing single component MTV at the nozzle exit without the wedge models installed. For each Reynolds condition, four lines were written vertically in the flow and the initial and time delayed images were processed as described in the previous section. Raw images of the averaged time-zero images for each Reynolds condition are shown in fig. A.1. From these images, it can be seen that the laser intensity had significant variation across the image plane. The center two lines in each case are of significantly higher quality than the outer lines, and the last line is by far the weakest. The following discussion will show results for all four lines in each case, though greater focus is placed on the results of the first three lines for this reason.

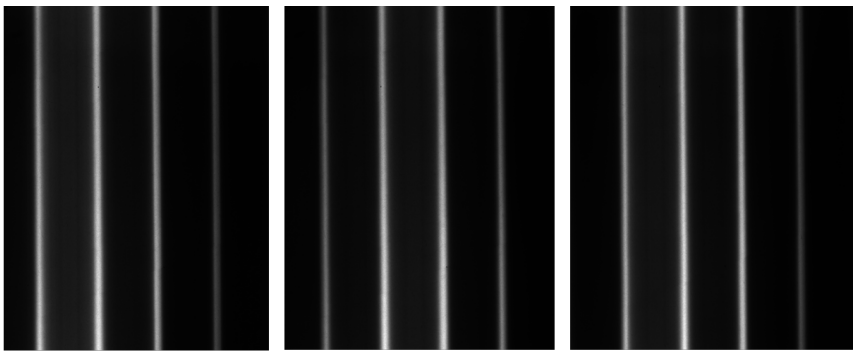

(a) Re/m=2.1e6 (b) Re/m=3.5e6 (c) Re/m=5.1e6

Figure A.1: Raw images of freestream MTV, zero time delay, for each Reynolds condition. Imperfect laser intensity profiles cause the outer lines to be of significantly lower quality than the two center lines in each case.

Results of freestream MTV for the first Reynolds condition of Re/m=2.1e6 are shown in

fig. A.2 and fig. A.3 below. The mean velocity is 807 m/s and the turbulent intensity $(U'/\overline{U})$, is approximately 1 %.

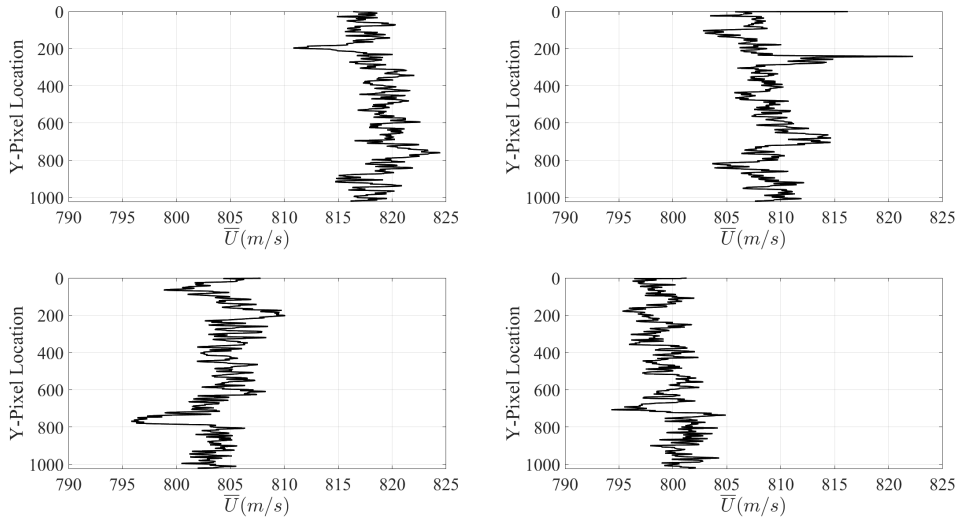

Figure A.2: Freestream mean velocity for Re/m=2.1e6 condition. Top left to bottom right are lines moving from left to right in raw image.

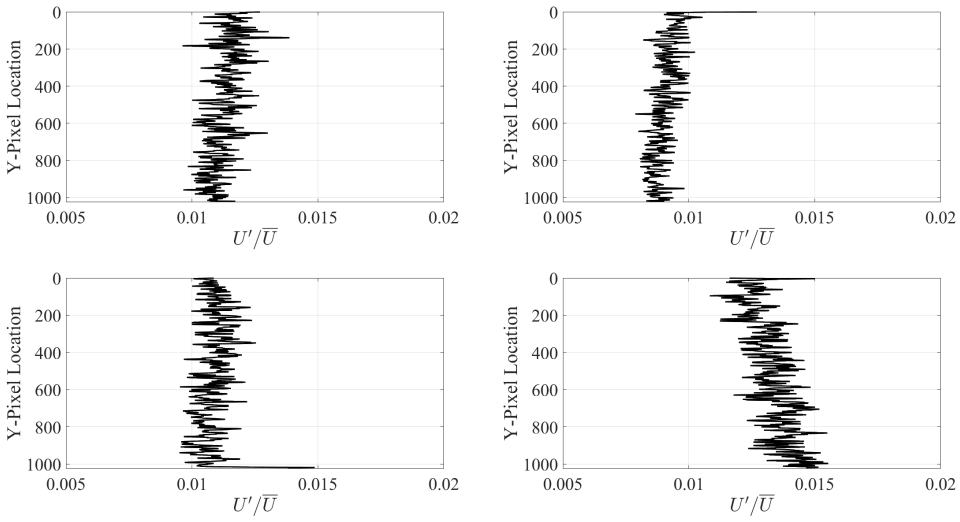

Figure A.3: Freestream velocity RMS for Re/m=2.1e6 condition. Top left to bottom right are lines moving from left to right in raw image.

Results of freestream MTV for the first Reynolds condition of Re/m=3.6e6 are shown in fig. A.4 and fig. A.5 below. The mean velocity is 785 m/s and the turbulent intensity $(U'/\overline{U})$, is approximately 1.3 %.

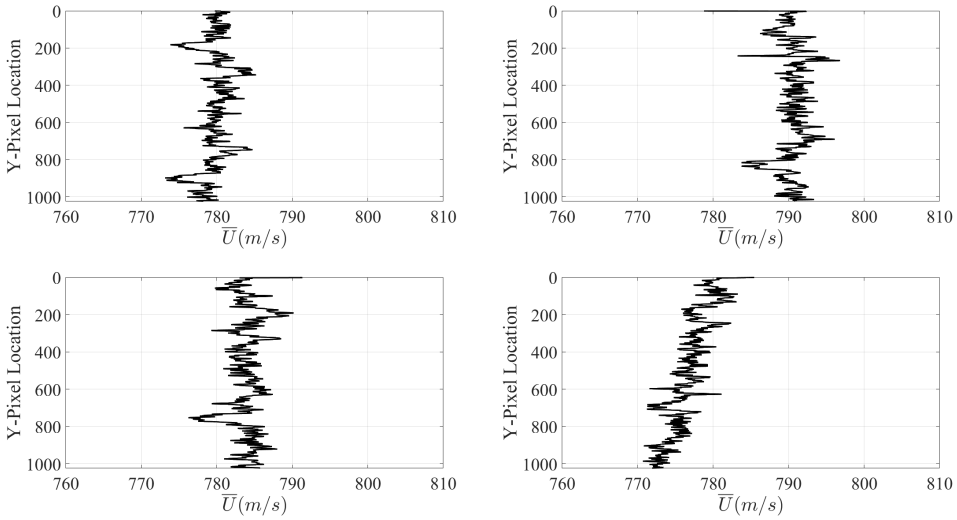

Figure A.4: Freestream mean velocity for Re/m=3.6e6 condition. Top left to bottom right are lines moving from left to right in raw image.

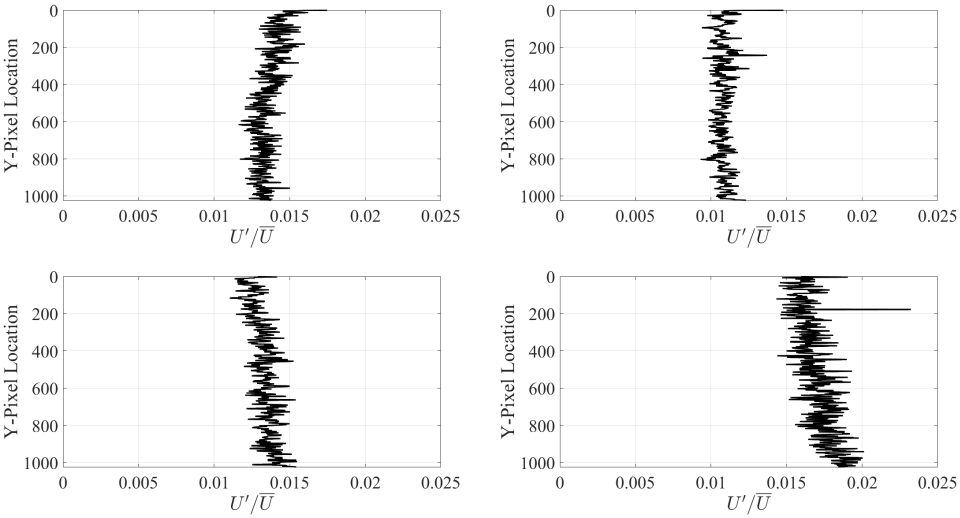

Figure A.5: Freestream velocity RMS for Re/m=3.6e6 condition. Top left to bottom right are lines moving from left to right in raw image.

Results of freestream MTV for the first Reynolds condition of Re/m=5.1e6 are shown in fig. A.6 and fig. A.7 below. The mean velocity is 793 m/s and the turbulent intensity $(U'/\overline{U})$, is approximately 0.7 %.

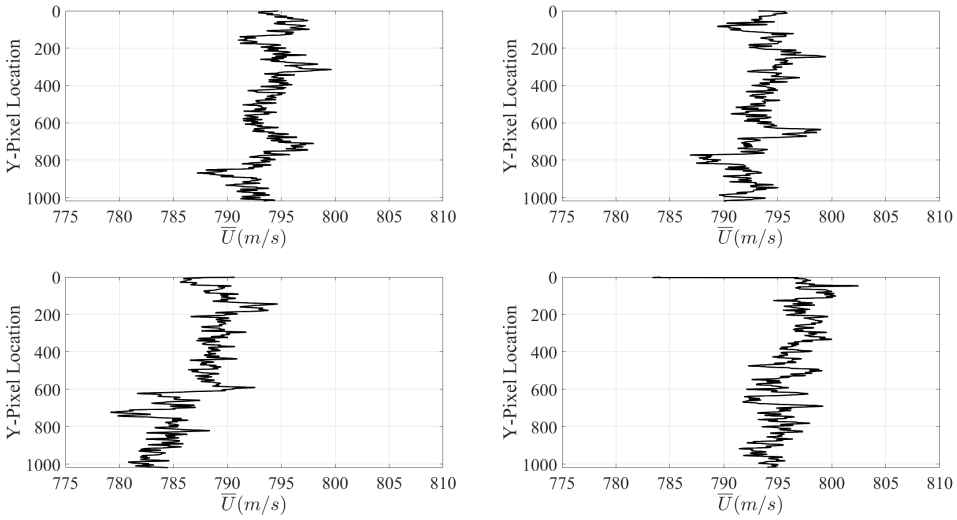

Figure A.6: Freestream mean velocity for Re/m=5.2e6 condition. Top left to bottom right are lines moving from left to right in raw image.

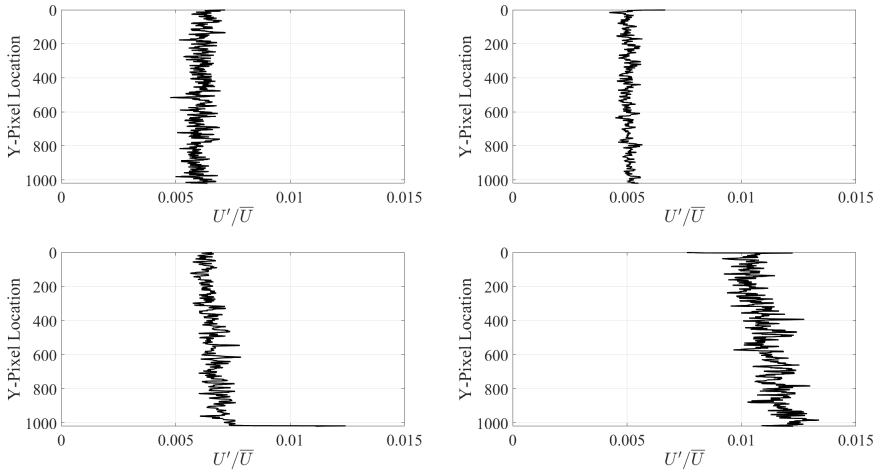

Figure A.7: Freestream velocity RMS for Re/m=5.2e6 condition. Top left to bottom right are lines moving from left to right in raw image.

A.2 Temperature Characterization

Independent freestream thermometry was also performed on the nozzle exit without the wedge models installed. The in-situ processing technique was applied, and the mean temperature was prescribed as 78K. Fluctuating temperatures were found to range 4-10 %, fig. A.8, consistent with those determined in Mach stem flow images.

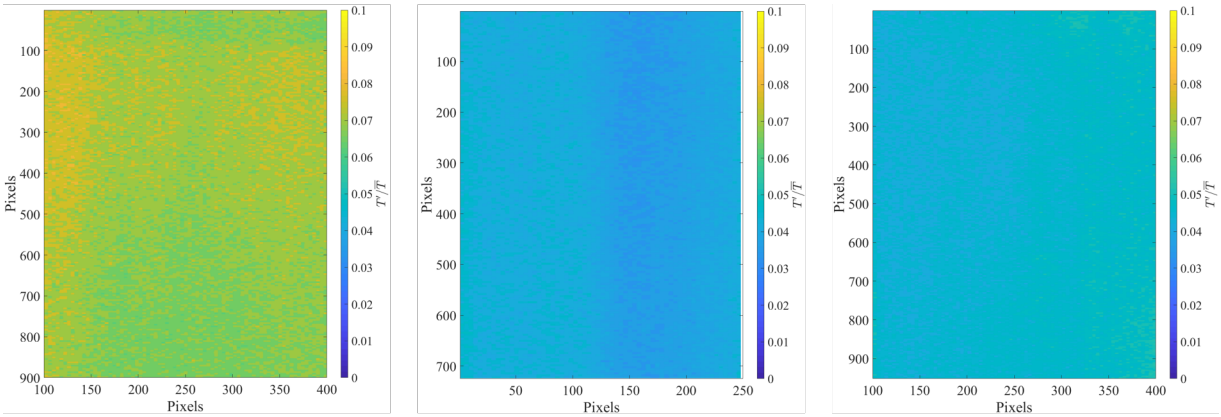

(a) Re/m=2.1e6 (b) Re/m=3.5e6 (c) Re/m=5.1e6

Figure A.8: Freestream temperature RMS for three Reynolds conditions.

APPENDIX B

LINEAR PLIF THERMOMETRY

Thermometry images were processed using custom applications written in Matlab. Freestream images were processed following a conventional approach for linear LIF thermometry. It was believed that the high temperature and density downstream of the shock, coupled with the necessary laser intensity to obtain signal in the freestream led to a non-linear response in the Mach stem flow. A separate processing routine was written to examine Mach stem PLIF images, where each region of the flow was individually calibrated and analyzed for an assumed mean temperature.

In the conventional application, inputs allowed the user to select the overall interrogation region, and specify parameters such as tunnel conditions and desired bin size. The image pairs were binned in two dimensions using the specified bin size by averaging the non-negative, real values across the bin. This was done to images of the laser profile in a constant temperature region as well. The laser profile images were then normalized by peak intensity value, and the calibration and flow images were divided by the normalized profile to correct for laser intensity variations.

Next the calibration images of known temperature were analyzed by the application to determine the "C_{12}" value. The profile-corrected calibration images were divided to determine R_{12} at each point. The user could then select a small region within the calibration image and the specified temperature value was then used to calculate C_{12} within this region. The calculated C_{12} value was then used to calculate temperature across the entire calibration image for verification that the calibration was good. The user could make adjustments and repeat the calibration as needed. Once the calibration was accepted, the flow images would be processed.

The laser profile correction was applied to each image pair, and the ratio of the images was calculated for each point. Temperature was then calculated based on the previously determined calibration constant and stored in a matrix. Once all image pairs had been processed, the mean and fluctuating temperature values for the entire image could be determined in post-processing.

Examples of mean and RMS fluctuating temperatures are shown in fig. B.1 and fig. B.2 below.

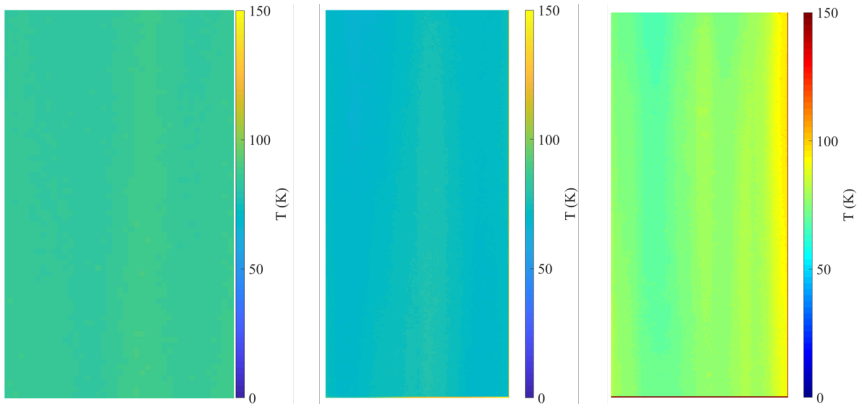

Figure B.1: Mean temperature contours of freestream flow, lowest to highest Reynolds conditions shown from left to right.

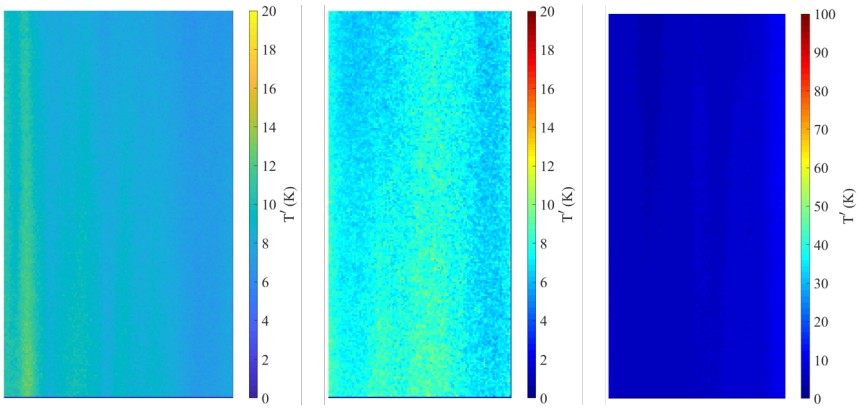

Figure B.2: Temperature RMS fluctuation contours of freestream flow, lowest to highest Reynolds conditions shown from left to right.

The images were processed with 4x4 pixel bins. Some affects from laser intensity can still be seen in some of these images, indicating the correction process may not have been sufficient. Fluctuating values are found to be consistent with those determined using the in-situ processing technique.